UNIVERSITY OF CALIFORNIA
RIVERSIDE

A Broad Spectrum of Fault Behaviors in Fast and Slow Earthquakes

A Dissertation submitted in partial satisfaction
of the requirements for the degree of

Doctor of Philosophy

in

Geological Sciences

by

Bo Li

March 2019

Dissertation Committee:

Dr. Abhijit Ghosh, Chairperson
Dr. David D. Oglesby
Dr. Gareth Funning

The Dissertation of Bo Li is approved:

Committee Chairperson

University of California, Riverside

Acknowledgments

I am grateful to my committee members for their thoughtful comments that led to great improvement of my dissertation. Thanks so much my advisor-Abhijit Ghosh. I do appreciate all your advice on my research work in our weekly group meeting. Also many thanks to David D. Oglesby, our department chair. Without your supporting letter for applying the visa, I may not be able to come to the U.S.A and do my Ph.D. research. I am also grateful for Gareth Funning. Thank you for your class in teaching us how to do programming and make fancy figures in GMT. I am also indebted to my friends in the Earth Sciences Department at the University of California, Riverside, for your help and care over years in my life and research. Part of Chapter 2 has been published in Pure Applied Geophysics (Li and Ghosh, 2016), and part of work in Chapter 3 has been published in Geophysical Research Letters (Li and Ghosh, 2017).

ABSTRACT OF THE DISSERTATION

A Broad Spectrum of Fault Behaviors in Fast and Slow Earthquakes

by

Bo Li

Doctor of Philosophy, Graduate Program in Geological Sciences
University of California, Riverside, March 2019
Dr. Abhijit Ghosh, Chairperson

Faults show complex slip behaviors at different sections depending mainly on their stress and friction distributions. In the seismogenic zone, a fast earthquake happens when the frictional resistance to fault movement reduces faster than the decrease in elastic stress due to fault slip, and it releases seismic energy that causes ground shaking. Increases in depth, temperature and pressure change the frictional properties from velocity weakening to strengthening. This deeper section is referred to as the creeping zone and shows stable sliding without any stress drop. In between, there is a transition zone where slow slip can occur on asperities embedded in the creeping region (*Bartlow et al.*, 2011; *Ghosh et al.*, 2012; *Obara et al.*, 2011). The slip cannot reach high enough velocities to produce regular earthquakes, but sometimes it is still able to radiate low amplitude and low frequency seismic waves (*Peng and Gomberg*, 2010). Seismicity in the seismogenic zone can trigger slow slip in the transition zone. It can also change the stress and accelerate or decelerate the seismicity on adjacent faults or even on faults hundreds to thousands kilometers away when the earthquake is large enough. Conversely, slow slip in the transition zone can also

change the surrounding stress field and increase the stress in the up-dip seismogenic zone, potentially advancing the timing of earthquake failure.

In this dissertation, I study the broad spectrum of fault behaviors and explore the potential relationships between them. In *Chapter 1*, we give an introduction to fast and slow earthquakes and briefly introduce the main methods used to study them. In *Chapter 2*, I apply the back-projection method to two case studies: the 2015 M_w 8.3 Illapel earthquake, using one array with both low- and high-frequency bands imaging multiple rupture patches, and the 2015 M_w 7.8 Gorkha earthquake using multiple global arrays to image the rupture process and detect aftershocks. The back-projection results of the Gorkha earthquake imaged by different global arrays show similar rupture processes but vary in detail. One array shows continuous eastward rupture for $\sim$ 60 s while other arrays show a branching rupture to the northeast at $\sim$ 45 s. In addition, we combine multiple global arrays to improve the resolution of the back-projection method. The higher resolution also allows us to detect 2.6 times the number of aftershocks than that recorded in the global catalog.

In *Chapter 3*, we apply the multi beam back-projection method (MBBP) to study the slow earthquakes of the Unalaska-Akutan region in the Alaska-Aleutian subduction zone. We detect near-continuous tremor and low frequency earthquakes for nearly two years. The slow earthquakes are distributed heterogeneously in three clusters and are located deeper than those in other subduction zones. The tremors show both short and long-term migrations along strike and dip directions with a wide range of velocities. In addition, tremors and LFEs show strong spatio-temporal correlations. They are located in the same

patches, and when there are LFEs bursts during tremor signals. We also observe some cases where local or regional earthquakes can terminate or amplify slow earthquake activity.

In *Chapter 4*, we use the move-max matched filter method to detect small local earthquakes along the San Jacinto fault (SJF) zone that are triggered by the 2014 M_w 7.2 Papanoa earthquake. Using the catalog events as templates, the move-max matched filter method detects 5.4 times the number of earthquakes recorded in the ANSS and SCSN catalog, while the matched-filter method only distinguishes 3.2 times the number of catalog events using the same detection threshold. After relocation using hypoDD, we find a new normal fault with strike almost perpendicular to the SJF. More than one mechanism may be responsible for triggering earthquakes. The transient dynamic stresses may have triggered slow slip or fault creep, and lead to the increased and protracted seismicity along the San Jacinto Fault (SJF). In addition, the time-dependent acceleration to failure process initiated by the dynamic stress change can result in the enhanced seismicity on the new fault.

Contents

List of Figures

List of Tables

Chapter 1

Introduction

1.1 Fast Earthquakes

Faults show complex slip behaviors in different locations, with these behaviors depending mainly on the faults stress and frictional property distributions. This is particularly clear on subduction faults (Figure 1.1). In the seismogenic zone, sudden slip with associated stress drop (earthquakes) can occur when the frictional resistance to fault movement reduces faster than the elastic stress decrease due to fault slip, followed by periods of no motion as stress recharges (*Schwartz and Rokosky*, 2007). This is referred to as stick-slip motion, and the frictional behavior is referred to as slip weakening. When the fault slips quickly enough and has a large enough stress drop, dynamic forces become significant and radiate a fairly large amount of seismic energy (*Peng and Gomberg*, 2010), which in turn is strong enough at the crack tip to overcome more frictional forces on locked sections of the fault, produce a large earthquake, and potentially cause significant societal impact.

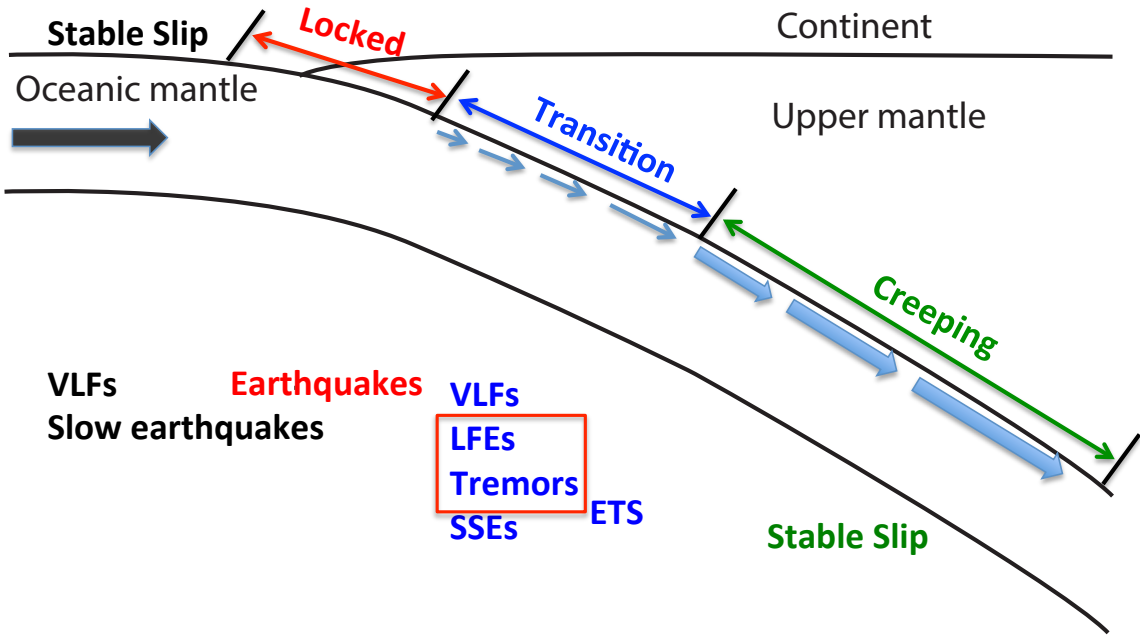

Figure 1.1: A schematic diagram of a subduction megathrust fault. In this dissertation, we are focusing on the regular earthquakes in the locked zone, the LFEs and tremors in the transition zone.

1.1.1 The rupture process of large earthquakes

When a large earthquake happens, the entire fault does not rupture simultaneously. In any given period within the duration of an entire event, only a small patch of fault slips while other parts are not slipping (*Heaton*, 1990). The rupture occurs as an expanding slip front with surrounding fault areas remaining locked. Understanding the earthquake rupture process is fundamental for our ability to discern the nature of fault systems and earthquake hazards (*Olson and Apsel*, 1982). The spatio-temporal evolution of the rupture process its initiation, propagation and termination helps us study the rupture velocity and provides an opportunity to address some fundamental questions about the earthquake source properties, rupture directivity, subsurface structures, aftershocks and disaster prediction and relief. It

also improves our understanding of the relationship between earthquake complexity and the heterogeneous and multi-scale structure of active fault zones (*Meng et al.*, 2011).

Because of its great significance, there are increasing requirements for very detailed information about the rupture processes of earthquakes, especially large events. Since the advent of seismometers, people began to use strong motion seismograms to analyze the rupture processes. *Trifunac* (1974) developed an approximate three-dimensional dislocation model for the San Fernando earthquake by using the data from five strong-motion accelerograph stations centered above and surrounding the fault. *Heaton and Helmberger* (1979) constructed a three-dimensional dislocation model of a finite fault by summing point dislocations distributed over the fault plane. *Miyatake* (1992) reconstructed the dynamic rupture process of the 1979 Imperial Valley earthquake using the kinematic parameters previously obtained through waveform inversion techniques. *Takeo* (1987) developed a new inversion method to investigate the dislocation distribution and the character of rupture propagation using strong motion records. The application of these methods can provide the detailed spatial distribution of slip amplitude, the rupture speed, and the source-time function, and show that the slip on a fault can be highly variable. Such inverse methods have enhanced our understanding of earthquake rupture processes. However, these methods require a lot of assumptions, the calculation of Green's functions to compute synthetic seismograms to compare with ground-motion data, and to compute surface displacements to compare with geodetic information (e.g. *Hartzell and Heaton*, 1983; *Wald et al.*, 1991; *Yoshida et al.*, 1996). Thus, it is time-intensive to derive the parameters that are necessary

to construct the fault dislocation model. This limitation prevents such methods from acting as efficient disaster relief and aftershock forecasting tools.

1.1.2 The back-projection method

One of the most important tasks after a large earthquake is to determine a finite source rupture model as quickly as possible so that a map of regions with the strongest shaking can be provided to guide emergency response and rescue (*Xu et al.*, 2009). In order to achieve this as soon as possible, methods utilizing the time-reversal property of the wave equation to identify various sources of seismic energy have been employed over the last 29 years (e.g. *Kao and Shan*, 2004, 2007; *Baker et al.*, 2005; *Krüger and Ohrnberger*, 2005; *MacAyeal et al.*, 2006). The back-projection technique is one of the most popular methods. It uses the curvature of wave fronts recorded at large aperture, dense seismic arrays and the time-reversal property of these waves to determine the timing and location of the energy source that generates the seismic waves (Figure 1.2) (*Ishii et al.*, 2005). This process can be expressed mathematically as:

$$s_i(t) = \sum_{k=1}^{n} \alpha_i \mu_k (t + t_{ik} + \Delta t_k) \tag{1.1}$$

Where s_i is the stack (summed up) seismograms at the ith source potential point, α_k is the normalization factor at station k, u_k is the seismogram at station k, t_{ik} is the theoretical travel time between the ith grid point and kth station, t_k is the empirical travel time correction made at each station, t is time with respect to a reference event, and n is the number of stations.

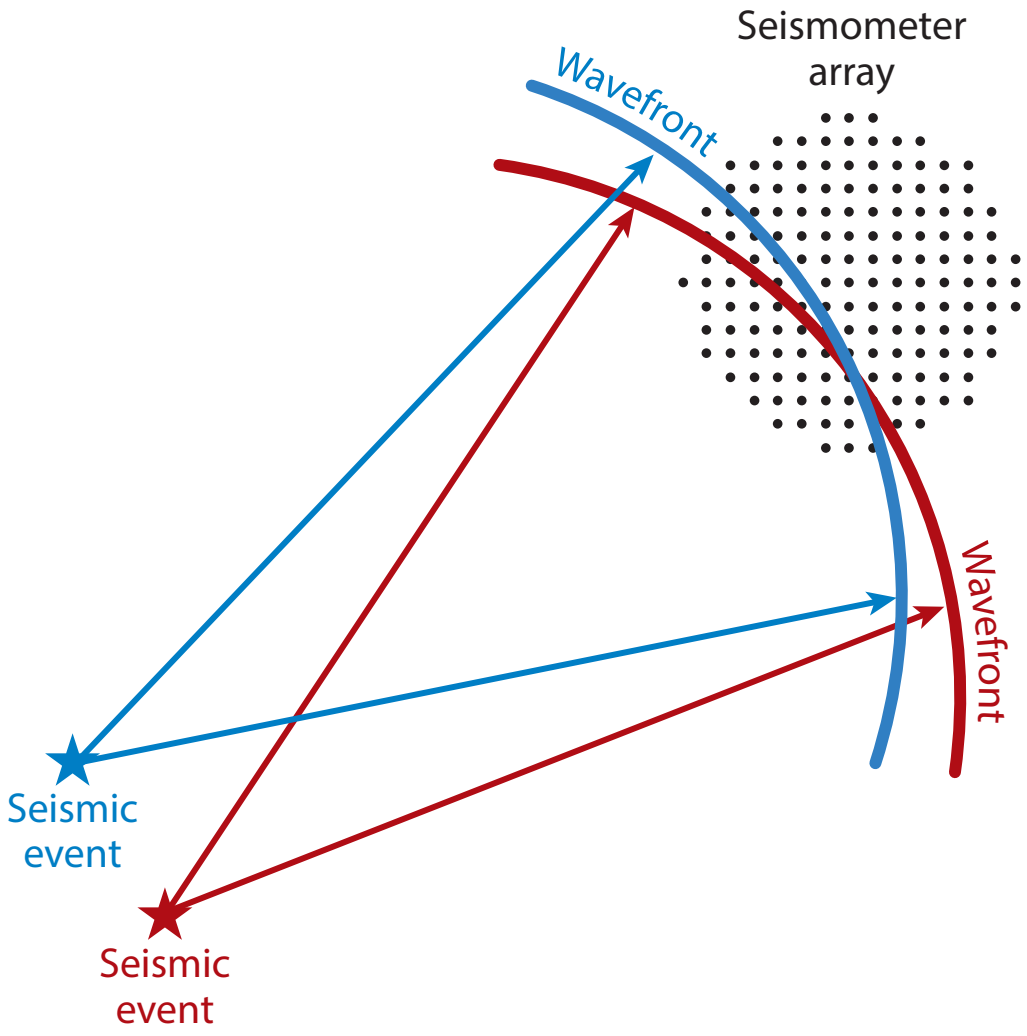

Figure 1.2: The schematic diagram showing the back-projection method (*Kiser and Ishii*, 2017). Each black dot represents one seismic station that recorded the earthquake signal. The differently colored curves show the rupture front at different times, with the colored star indicating the energy source at the corresponding time.

Compared to other methods that study earthquake rupture, the back-projection technique has two advantages. First, it does not require extensive computation of the wave field and any prior knowledge of the duration of the event and geometry of the fault. The only prior information required is a radial velocity model and an estimated hypocenter. Thus, it does not require a great deal of time to estimate the fault parameters. It is only

necessary to obtain the seismic data and select high signal-to-noise stations before applying the analysis. Additionally, it can be applied to data at higher frequencies, i.e. up to 1-2 Hz (*Ishii et al.*, 2005), which has important implications for structural engineering studies, and is sensitive to dynamics of earthquakes, such as acceleration of rupture and rapid changes in slip amplitude (e.g. *Das and Aki*, 1977; *Madariaga*, 1977). The back-projection method was first successfully applied by *Ishii et al.* (2005) to study earthquake rupture and propagation for the 2004 Sumatra-Andaman earthquake. The rupture of this giant event, as imaged using back projection, had a length of nearly 1300 km and lasted almost 600 s. This study showed the capability of the back projection method to spatially show rupture propagation and energy radiation as a function of time (*Kiser and Ishii*, 2012). Thus far, it has been successfully applied to study the rupture process of many large earthquakes earthquakes (e.g. *Kiser and Ishii*, 2012; *Ishii et al.*, 2005; *Xu et al.*, 2009; *Koper et al.*, 2011; *Meng et al.*, 2012). The direct P-wave is the preferred phase to use in the back-projection method since it has the highest propagation velocity, and hence is the first phase to reach seismic stations. Thus it is able to show the spatio-temporal patterns of the rupture process without much interference from other phases of body and surface waves that follow.

1.1.3 Aftershocks detection after large earthquakes

The spatio-temporal evolution of aftershock sequences has been used by several studies to constrain fundamental aspects of stress transfer (e.g. *King et al.*, 1994), post seismic deformation (e.g. *Hsu et al.*, 2006; *Sladen et al.*, 2010), rupture extent (e.g. *McCann et al.*, 1979), the constitutive relationships that govern slip (e.g. *Dieterich*, 1994), and forecasting of future seismicity (e.g. *Cocco et al.*, 2010). Aftershock detection have

been limited by a lack of local instrumentation, which necessitates the use of teleseismic data. Even though global arrays are deployed worldwide, this limitation still exits in some regions where seismic arrays are hard to install and maintain. In addition, the detection and characterization of early aftershocks are usually hampered by the arrival of various seismic phases immediately following giant earthquakes (e.g. *Kagan*, 2004; *Kagan and Houston*, 2005; *Lolli and Gasperini*, 2006; *Lengliné et al.*, 2012). This lack of cataloged early aftershock activity is generally considered to be a detection problem, but also has important consequences for determing the seismic hazards and constitutive relationships acting after the large slip associated with a large earthquake (e.g. *Dieterich*, 1994).

In addition to imaging the rupture process of large earthquakes, the back-projection method can also be applied to detecting aftershocks above a certain magnitude, which depends on the distance between the source region and the array, the focal mechanisms of earthquakes, the azimuth of the array to the source, the velocity structure, and the resolution of the array. By combining multiple arrays, we can greatly improve the azimuthal coverage and signal-to-noise ratio, which results in much higher resolution in the back-projection method. Multi-array methods can allow for better tracking of the rupture process, and enhance the detection capability to identify more earthquakes that are not recorded by current global catalog. Thus, this method enables us to build a more complete earthquake catalog and better understand the stress state of the fault.

1.2 Slow earthquakes

Both the large earthquakes and their aftershock sequence are the result of fast fault slips in the seismogenic zone. However, the seismic moment at most plate boundary faults only accounts for a fraction of plate tectonic motions (*Frank*, 2016). The slip in the downdip transition zone cannot reach these fast velocities to produce regular earthquakes, resulting in the aseismic and episodic slow slip events (Figure 1.1). However, some slow slip are still able to radiate low amplitude and low frequency seismic waves (*Peng and Gomberg*, 2010). Those events are termed as slow earthquakes, including tremors, low frequency earthquakes (LFEs) and very low frequency earthquakes (VLFEs). In our study, we focus on the tectonic tremor (TT) and LFEs in the Alaska-Aleutian subduction zone.

1.2.1 Tectonic tremor

Tectonic tremors (TTs), also known as non-volcanic tremors (NVTs), are characterized by non-harmonic emergent signals of sustained amplitude lasting from minutes to days, and sometimes for months or longer. They were first observed by *Obara* (2002) from a non-volcanic area in the Nankai trough subduction zone in southwest Japan. The predominant frequency of TT ranges from 1 to 10 Hz, and the high-frequency energy of tremor is more depleted than that of an ordinary earthquake. Following the identification of TT, studies have revealed TT activity in other subduction zones including Cascadia (*Rogers and Dragert*, 2003), Mexico (*Payero et al.*, 2008), Costa Rica (*Thorwart et al.*, 2007), and Alaska (*Peterson et al.*, 2011). Recent studies also show that TTs are not limited to subduction environments. They are also observed along the San Andreas Fault (SAF), a continental

transform plate boundary fault (*Ellsworth et al.*, 2005; *Nadeau and Dolenc*, 2005), and beneath the central Range in Taiwan, an arc-continental type collision environment (*Peng and Chao*, 2008). TT tends to migrate along the subduction zone near the seismic-aseismic transition zone on the plate interface. Observations of tremor in Japan strongly suggest that where tremor occurs, it outlines the depth extent of slip in large megathrust earthquakes (*Ide et al.*, 2007a). Thus study of tremors provides a window into the deep roots of subduction zones, a poorly understood region that is largely devoid of seismicity (*Rubinstein et al.*, 2009).

Tremors accompanying slow slip events were first observed in Cascadia and southwest Japan (*Rogers and Dragert*, 2003; *Hirose et al.*, 1999). SSEs release accumulated plate boundary strain with durations on the order of days to years without radiating seismic energy that can be detected. SSEs therefore cannot be detected by regular seismic arrays designed for earthquake monitoring. SSEs have been detected in multiple subduction zones by continuous Global Positioning System (GPS) networks and their durations vary from days to years (e.g. *Schwartz and Rokosky*, 2007; *Dragert et al.*, 2001; *Ozawa et al.*, 2001; *Kostoglodov et al.*, 2010; *Yamamoto et al.*, 2005). Such observations have greatly improved our understanding of strain accumulation and release at plate boundaries and provide a supplement for the moment release budget because seismic moment from regular earthquakes at most plate boundaries accounts for only a fraction of plate tectonic motions (e.g. *Frank*, 2016). SSEs can perturb the surrounding stress field and may increase stress on the surrounding regions of a fault, bringing it closer to earthquake failure (*Kato et al.*, 2012). The coupled phenomenon between tremors and SSEs provides us a new way to study slow slip

events wherever GPS data are limited and help to better assess seismic hazard (*Schwartz and Rokosky*, 2007).

Recent studies of the Mexican subduction zone have observed changes in seismic velocity near the subduction interface during periods of intense TT activity during SSEs, suggesting that TT activity can be used to track transient strain at depth (e.g. *Rivet et al.*, 2011). Tremor migration is an important feature that provides clues about the dynamics of the slow earthquakes (*Ghosh et al.*, 2010a,b). Tremor and slow slip can be used to learn about the conditions in the deep root zone of some major faults and suggests the possibility of greater predictability of large earthquakes. These observations highlight the need to better understand TTs and their effect on the subduction cycle.

1.2.2 Multi beam back-projection method (MBBP)

Tremors typically emerge slowly from the background noise and lack any regular structure, with peaks in amplitude occurring at random during the episode, without any easily identifiable seismic body wave arrivals. The lack of easily identifiable features makes it difficult to distinguish TT from cultural or environmental noise (*Rubin*, 2011). The absence of easily identified body wave arrivals also contributes to the difficulty in locating TT. Methods used to locate earthquakes largely depend on the impulsive nature of their body wave phases, rendering them rather ineffective for locating tremor.

In this dissertation, we apply the multi beam back-projection method (*Ghosh et al.*, 2009, 2012) to detect and locate tremors by automatically scanning the mini array data. This method divides continuous data into numerous time windows and runs beamforming for each time window to get the slowness and azimuth information of the signals. The

beamforming method is similar to the back-projection method, but instead of calculating travel time in geographic domain, it obtains the travel time in slowness domain. With a local velocity model, we divide the study region into 3-D grids and calculate the slowness and azimuth values for each grid relative to the center of each mini array. Then we do ray tracing of the beamforming results to the study region. Ideally the traces by multiple arrays will intersect at the source location (Figure 1.3).

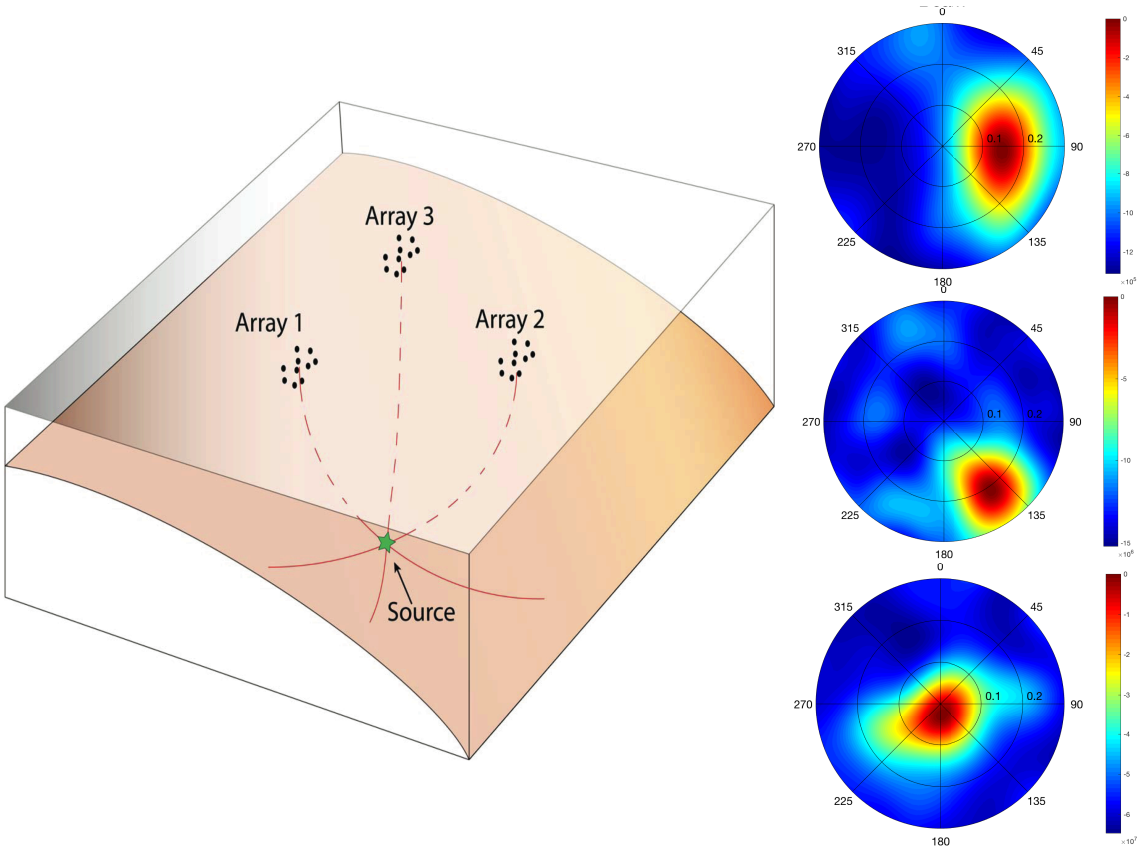

Figure 1.3: Schematic diagram showing basic idea behind the multi beam back-projection (MBBP) algorithm (modified from Ghosh et al., 2012). Each beam focus shows the slowness and azimuth of the signal of the current time window. The intersection point of multiple traces is the location of the signal source.

1.2.3 LFEs

Since 1999, the Japan Meteorological Agency (JMA) has differentiated a class of events that are different from earthquakes, denoted as low-frequency earthquakes (LFEs), in their seismicity catalogue. LFEs are small earthquakes (less than magnitude 2) with amplitudes that decay much faster at higher frequencies, particularly above 10 Hz, which occur during episodes of deep tremor in southwest Japan (*Katsumata and Kamaya*, 2003; *Shelly et al.*, 2006) and belong to a newly discovered class of slow earthquakes (*Ide et al.*, 2007a). The existing literature shows LFEs comprise at least a portion of tremor (e.g. *Shelly et al.*, 2007a,b), and the spectral characteristics of tremor and LFEs are essentially identical. LFEs and TT occur in approximately the same region in map view and exhibit similar migration behavior along strike. *Brown et al.* (2009) also demonstrated that LFEs comprise tremor on the plate interface down-dip of the locked portion of three subduction zones. The close association implies their mechanisms are probably intertwined. Thus locations of LFEs can help constrain the location of tremor, and understanding their mechanism is critical for understanding tremor as a whole. *Shelly et al.* (2006) shows strong evidence that the LFEs occur on the plate interface, coincident with the inferred zone of slow slip. Thus LFEs could also provide another way to monitor slow slip at depth, potentially contributing to seismic hazard forecasting. The coupled phenomena of tremor, LFEs and episodic slow slip events represent a mode of failure for a transition zone between a locked and continuously creeping fault. In a subduction zone, this usually corresponds to the transition between the locked megathrust source region up-dip and the continuously slipping region down-dip (*Shelly et al.*, 2006), with few cases observed above the seismogenic zone.

LFEs are difficult to detect due to their inherently low signal-to-noise ratios (e.g. *Shelly et al.*, 2006). Swarms of LFEs have been observed within TT, with several sources producing many LFEs over time that are called multiplets (*Shelly et al.*, 2007b). This template-matching method (Figure 1.4) can be used to search for repeating LFEs once LFE templates are identified. Here we use both visual inspection and the modified automatic network-beamforming response method to find LFE templates (*Frank and Shapiro*, 2014). The visual inspection is an inefficient method in terms of time, and it also restricts the detection of LFE templates to the loudest events that are only visible above the tremor signal. The automatic beamforming method relies on the response of the entire seismic network to a theoretical source. It is based on two simple hypotheses: (1) if the hypocenter of a given LFE lies close to one of the theoretical sources on our 3-D grid, S0, it should be observed on the seismic network with a moveout very close to the one associated with S0; (2) if the average interstation distance is relatively small compared to the distance travelled by an arriving wave from S0, the travel paths of the arriving waves should not differ greatly, ensuring that each of the stations on the network record similar energy envelopes. In our case, mini arrays are used, thus we do not need to calculate the moveout between the source location and each array station, before performing a time shift and stack the squared velocity seismograms. Here we perform a sliding time window search. In each time window, we cross correlate between all the station pairs in the mini array and find the station with highest average cross correlation coefficient. Then we perform a time shift for all other stations based on the time to reach the peak cross correlation coefficient, and obtain the stacked beam power and summed cross coefficient. Then we set a threshold based

on the summed coefficient to remove incoherent noise, since both earthquakes and LFEs will produce higher summed coefficients. In addition, we also use the stacked beam power to remove earthquakes. Earthquakes generally produce higher energy than LFEs since they are shallower. In addition, we also visually check the seismograms and the spectra (Figure 1.5) to adjust our thresholds.

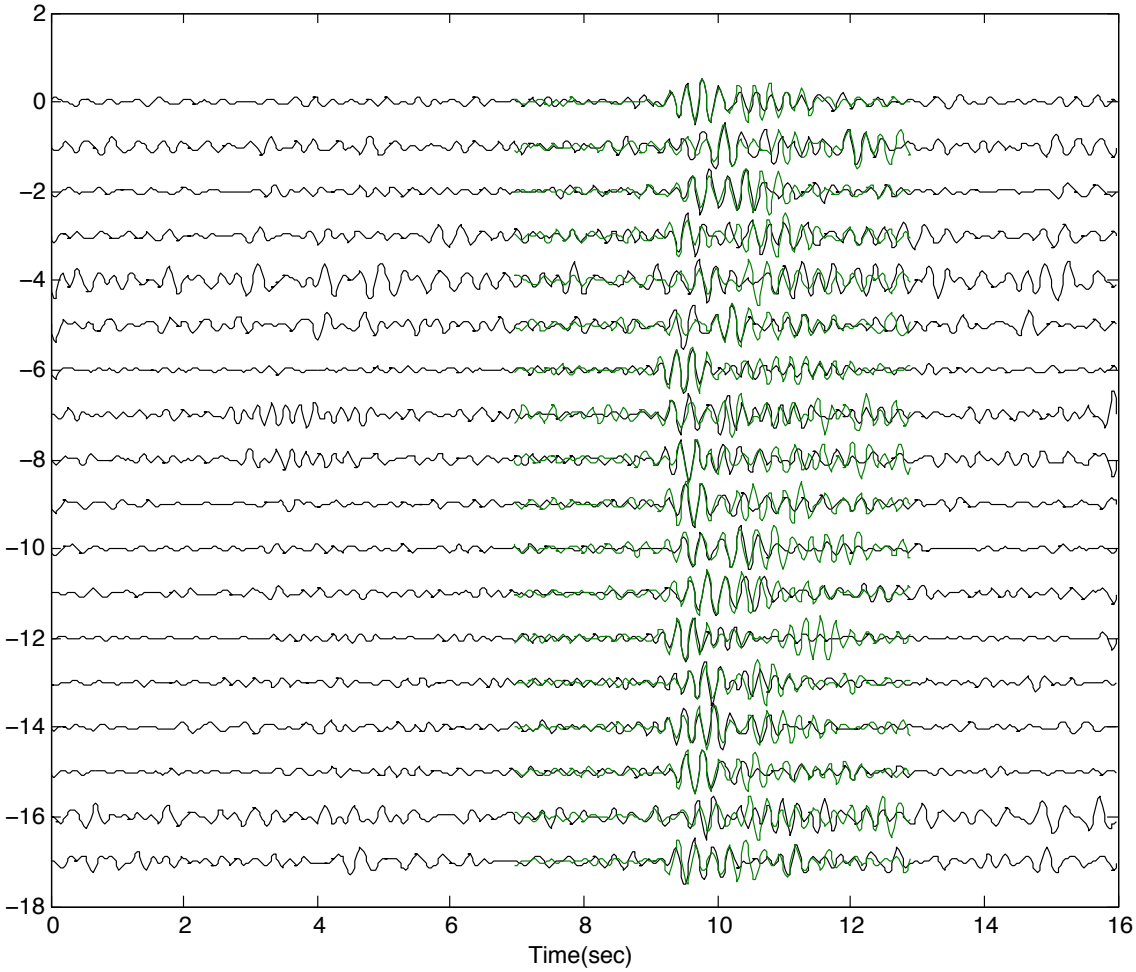

Figure 1.4: Example of template matching method. The green seismograms are the 6s template (18 components of 6 stations) and the black seismograms are continuous seismograms of the same stations at different times.

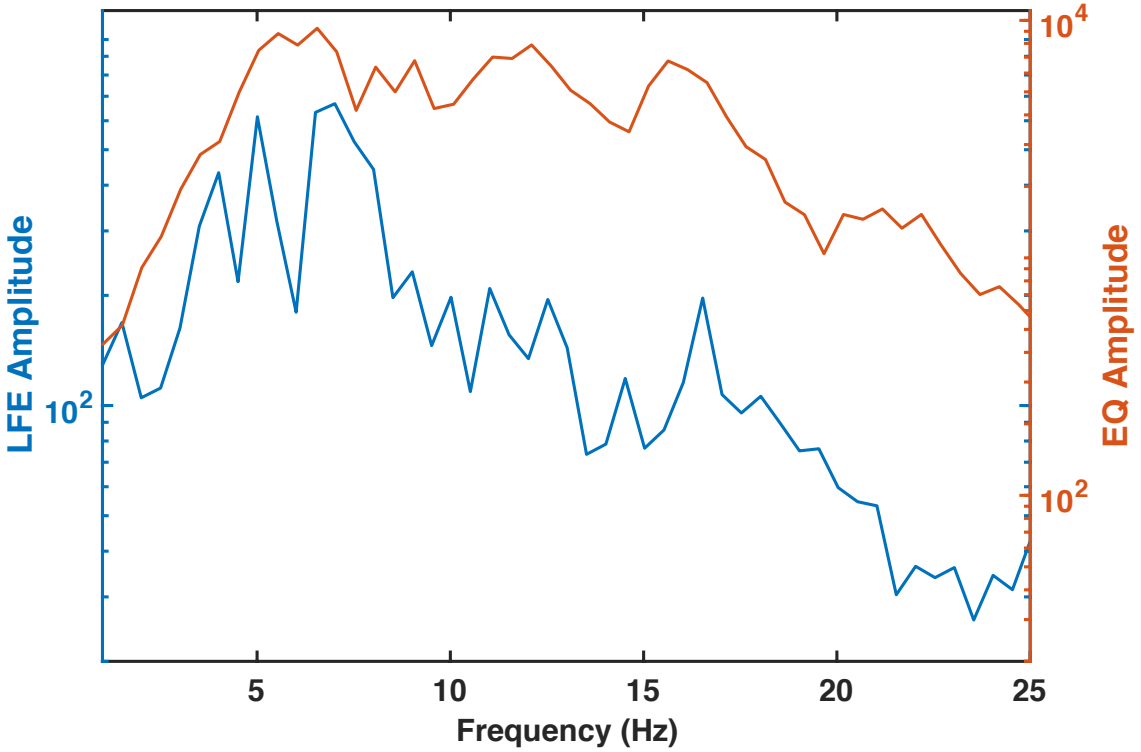

Figure 1.5: Spectra comparison between a regular earthquake and an LFE in the study region. The spectra are calculated for S-wave arrivals for a 3-s window, for 0.5 s before and 2.5 s after the phase arrival. The amplitudes of the LFE frequency spectrum decays more rapidly than that of the regular earthquake for frequencies above ~ 8 Hz.

Compared to the slow earthquakes in other subduction zones, study in the Alaska-Aleutian subduction zone is particularly challenging, and less progress has been made for three reasons. 1) Harsh weather conditions in this sparsely populated part of the world generate strong seismic noise. 2) The recording geometry in the Alaska-Aleutian margin is limited by geography. Seismic and geodetic studies are restricted to land-based linear instrument deployments due to the expense and logistics of amphibious geophysical studies. The limitation of seismic station coverage prevents the successful application of approaches similar to those used to observe tremor in other subduction settings. (3) The Alaska-Aleutian Arc seismic records include frequent signals from volcanoes, earthquakes, and possibly hy-

drothermal activity related to magmatic activity. The Alaska-Aleutian subduction zone, with the recurrence of large earthquakes, plays an important role in the worldwide subduction system. Thus, the study of slow earthquakes in this location helps us to better recognize the physical properties of the transition zone, provides new insights into the slow earthquake activities in this area, and studying the newly coupled phenomena (LFEs, TTs and SSEs) in this area would help researchers understand their relationship as a whole for other subduction zones. In addition, the frequently seismic activity also provides us a good opportunity to explore the potential relationship between slow and fast earthquakes.

1.3 Dynamic triggering of earthquakes

In addition to the interaction between fault slip in the seismogenic (fast earthquakes) and transition (slow earthquakes) zones on the same fault, and the quick triggering of aftershocks on regional fault networks, there are also observations showing that seismic activity can be affected by large earthquakes at much larger distances - hundreds to thousands of kilometers away. For example, the 2002 M_w 7.9 Denali Alaska earthquake triggered earthquakes in the Coso geothermal field in southeastern California, over 3600 km away (*Prejean and Hill*, 2009). The occurrence of triggering is the result of the dynamic stress redistribution induced by the passage of seismic waves of another earthquake. The stress changes due to a large earthquake located remotely is typically between ~ 0.1 and ≤ 1 MPa (*Prejean and Hill*, 2009). Thus, triggered earthquakes indicate the region is sensitive to small stress perturbations. Studies of triggered earthquakes provide clues to understand the stress state on a fault prior to failure and rupture initiation (*Johnson et al.*, 2015).

1.4 Summary of Projects

In this dissertation, I study the complex spectrum of fault behaviors and the potential interactions between them. First, we apply the back-projection method to image the rupture process of the 2015 M_w 8.3 Illapel earthquake using one array with low- and high-frequency bands to reveal multiple rupture patches. Then we combine multiple arrays to improve the resolution of the back-projection method to image the rupture process of the 2015 M_w 7.8 Gorkha earthquake, and detect the aftershocks following the mainshock. Secondly, we apply the multi beam back-projection method to study slow earthquakes (TTs and LFEs) in the Unalaska-Akutan region of the Alaska-Aleutian subduction zone using mini array data. We detect and locate abundant slow earthquakes, which are clustered in three patches to the south of Unalaska-Akutan Island. We analyze the spatio-temporal distributions of both tremors and LFEs in this subduction zone. They are located deeper compared to other subduction zones, and show strong sptatio-temporal correlations between tremors and LFEs. The results also show some correlations between slow and fast earthquakes. Finally, we use the move-max match filter (MMMF) method to study the local seismicity along the San Jacinto Fault zone that is triggered by a large earthquake hundreds of kilometers away. The result shows a significant increase in earthquakes detection by the MMMF method compared to the traditional template matching method, and shows delayed triggering a few hours after the teleseismic event. Then we discuss the possible mechanisms for the delayed triggering, such as the dynamic stress due to the passage of teleseismic waves trigger a local creep or small SSE, or initiate a time-dependent acceleration. These studies in the dissertation help provide a more comprehensive understanding of the slip behaviors,

physical properties, stress states and stress transfer of faults, and could lead to a better assessment of seismic hazards.

Chapter 2

Using Back-Projection to Image the Rupture Process and Detect Aftershocks of Large Earthquakes with Global Arrays

2.1 Imaging the Rupture Process of the 2015 M_w 8.3 Illapel Earthquake Using the US Seismic Array

2.1.1 Abstract

We study the rupture process of the M_w 8.3 Illapel, Chile earthquake that occurred on 16 September 2015 using the US seismic network as a large aperture array. We apply

the back- projection technique using two frequency bands, 0.1-0.5 and 0.25-1 Hz. Both frequency bands reveal that this event is characterized by the rupture of three patches. The higher frequency band shows an earlier burst of seismic radiation and illuminates a relatively down-dip patch of energy radiation. On the other hand, the lower frequency band shows a more up-dip rupture and matches well with slip inversion results in other studies. The Illapel earthquake ruptures about 100-km along-strike, and shows 40-km up-dip and 40-km down-dip movement away from the hypocenter, along the subduction megathrust fault. The earthquake first ruptures around the epicenter with a relatively low level of seismic radiation. Then, it propagates northeast along the Juan Femandez Ridge (JFR) to rupture a patch down-dip accompanied by strong higher frequency seismic radiation. Finally, it ruptures to the northwest of the epicenter and terminates south of the Challenger fracture zone (CFZ), releasing a burst of strong lower frequency seismic radiation. Most of the aftershocks are either within or at the edge of the rupture patch, a region characterized by high coupling in central Chile. The rupture is bounded along strike by two fracture zones to the north and south. The JFR to the south of the rupture zone may have acted as a barrier along-strike, leaving the area south of the mainshock vulnerable for a large damaging earthquake in the near future.

2.1.2 Introduction

A moment magnitude (M_w) 8.3 thrust earthquake occurred on September 16th 2015, at 22:54:32 (UTC), on the subducting interface between the Nazca and South American plates in central Chile. Even though the majority of the slip was concentrated offshore (e.g. *Heidarzadeh et al.*, 2016; *Ye et al.*, 2017; *Yin et al.*, 2016; *Melgar et al.*, 2016), the

Illapel earthquake still resulted in at least 15 deaths, destroyed or damaged thousands of houses, and left more than 16,000 people homeless (http://earthquake.usgs.gov). The occurrence of four large aftershocks within 30 min of the mainshock, each with moment magnitude greater than 6, intensified the damage in this area. The fault slip model resolved from the kinematic inversion of tide gauges, strong motion sensors, high-rate GPS stations, and sentinel-1A InSAR data shows a maximum slip of over 10-m northwest and up-dip of the epicenter (*Melgar et al.*, 2016). In central Chile, the downgoing Nazca plate subducts below the South American plate at a shallow angle with a convergence rate of 72 mm/year (*Barazangi and Isacks*, 1976; *DeMets et al.*, 1994). This region has produced a number of large megathrust earthquakes in recorded history. Since 1900, central Chile has experienced several earthquakes of magnitude 7.5 or larger, including the 1906 M_w 8.4 Valparaiso earthquake, the 1943 M_w 7.9 Illapel-Salamanca earthquake, the 1985 Ms 7.8 offshore Valparaiso earthquake (*Beck et al.*, 1998; *Tebbens et al.*, 1997; *Barrientos*, 1995) (Figure 2.1), and the more recent M_w 8.8 2010 Maule event (e.g. *Delouis et al.*, 2010; *Lay et al.*, 2010). The 2015 M_w 8.3 Illapel earthquake is located at the southern edge of the 1943 M_w 7.9 Illapel-Salamanca earthquake and to the north of the 1985 Ms 7.8 offshore Valparaiso earthquake rupture zone. This region is known as the Metropolitan segment in central Chile, characterized by high coupling between the overriding and downgoing plates (*Métois et al.*, 2012).

One of the most critical and time-sensitive tasks after a large earthquake is to rapidly determine the rupture extent and regions with the strongest shaking that could provide a guide for a quick emergency response and rescue operations (*Xu et al.*, 2009).

Here, we apply the back-projection technique (*Ishii et al.*, 2005) to study the rupture process of the Illapel, Chile earthquake. We use different frequency bands to compare the frequency-dependent rupture and energy radiation patterns.

2.1.3 Data and Method

The back-projection method assumes that the P-waves are radiated as the rupture propagates during a large earthquake. It utilizes the time-reversal property of the wave equation and curvature of wave fronts recorded by a large aperture, dense seismic array, to determine the time and location of the energy source (*Ishii et al.*, 2005). With no prior knowledge of the event duration and fault geometry needed, the back-projection technique has the capability of quickly mapping out rupture propagation and sources of higher frequency seismic energy radiation as a function of space and time (*Kiser and Ishii*, 2011). Since its introduction and successful application to image the rupture propagation of the M_w 9.2 2004 Sumatra earthquake by *Ishii et al.* (2005), the back-projection method has widely been used to study and quickly obtain rupture patterns for large and moderate size earthquakes, such as the 28 March 2005 Sumatra M_w 8.6 earthquake, the 12 May 2008 M_w 7.9 Wenchuan earthquake, the 12 January 2010 Haiti M_w 7.0 earthquake, etc. (e.g. *Walker et al.*, 2005; *Xu et al.*, 2009; *Meng et al.*, 2012; *Kiser and Ishii*, 2013). The direct P-wave is the preferred phase to use in the back-projection method, since it has the highest propagation velocity and, therefore, it is the first phase to reach seismic stations. Thus, it is able to show the spatiotemporal patterns of the rupture process without much interference from other phases of body and surface waves that follow.

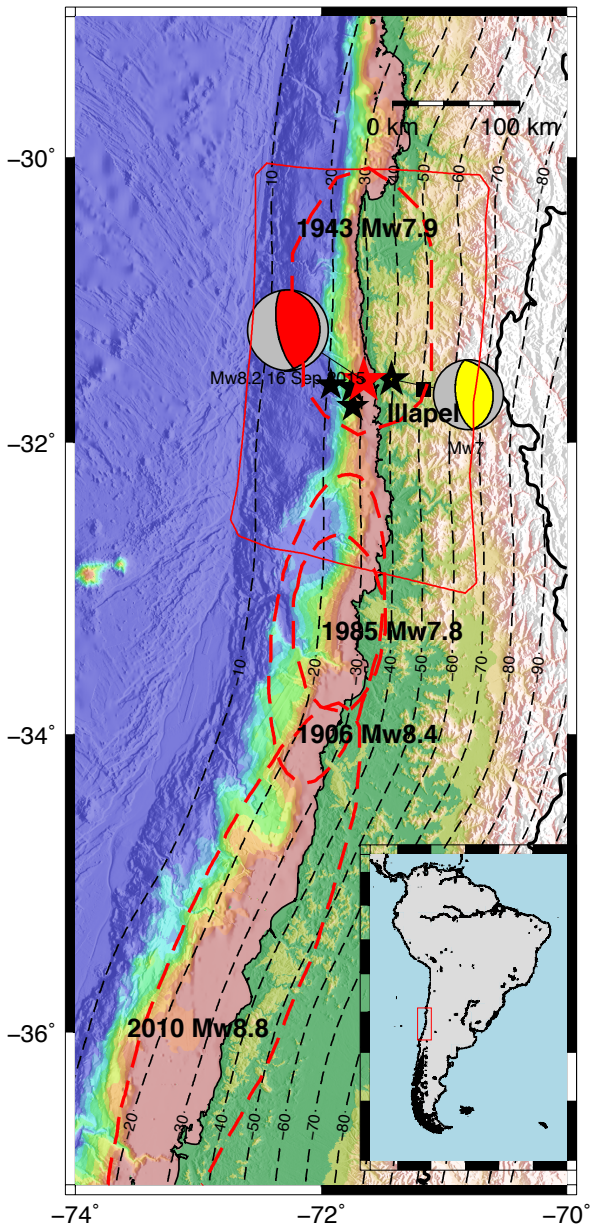

Figure 2.1: Location map of earthquakes in Central Chile. Red star shows the epicenter of the 2015 M_w 8.3 Illapel earthquake. The gray-red and gray-yellow beach balls represent centroid moment tensors for the mainshock and the M_w 7.0 aftershocks, obtained by the Global Centroid Moment Tensor (GCMT) project. Black stars show the epicenters of four large aftershocks ($M_w \geq 6$) that occurred within half an hour of the mainshock. The red dashed lines define the rupture zone of the 1906, 1943, 1985, and 2010 large earthquakes in Central Chile (*Contreras-Reyes and Carrizo*, 2011). The red box represents the slip inversion model region (*Melgar et al.*, 2016). The contour lines represent the depth of the plate interface in this subduction zone from the USGS slab model (http://earthquake.usgs.gov/data/slab/).

The study region for the Illapel earthquake is defined by the latitude range $33°S - 29°S$ and the longitude range $74°W - 70°W$. It is divided into grids with $0.1°$ spacing in both latitude and longitude. The Taup software developed by the University of Southern California, and a 1-D laterally homogeneous global velocity model (iasp91) (*Kennett and Engdahl*, 1991), are used to calculate the theoretical travel time from the source grid to each seismic station, with a constant source depth of 25 km. To avoid the waveform complexities from the upper mantle discontinuities and the core-mantle boundary effect (*Fan and Shearer*, 2015), the stations at a distance range between $30°$ and $90°$ are used. Most of the US seismic network stations occupy the right distance range with a reasonably wide azimuthal range, between $-40°$ and $5°$ measured clockwise from north. Only stations with higher signal to noise ratios (SNR) and high coherence are selected to minimize the interference from noisy signals. We apply a cross-correlation method on the first 20 s of the P waves to determine waveform coherency. We select 187 stations with average correlation coefficients above 0.5 distributed over the entire US (Figure 2.2) to perform the back-projection. We use a sliding time window approach, with 8-s long time windows and 3-s time steps, to image the rupture process of the mainshock using the back-projection technique. In addition, we use the calibration method developed by *Ghosh et al.* (2012) to reduce the location uncertainty caused mainly by varying source depths, 3-D velocity structures, and anisotropy along the travel path from the source to each station.

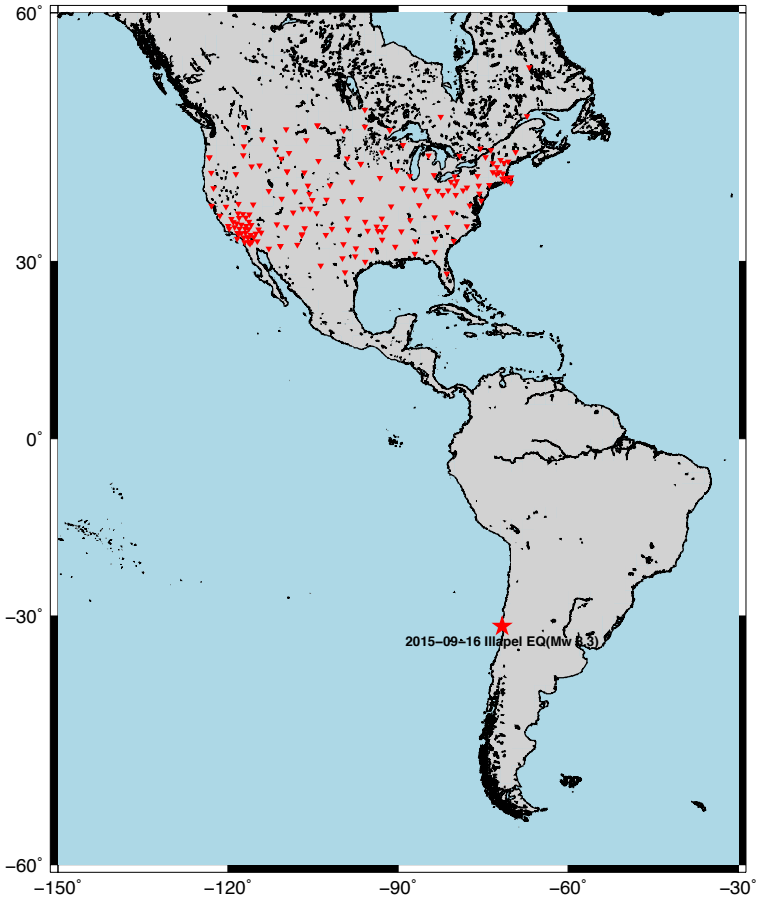

Figure 2.2: Distribution of the US seismic stations used in this study. Each red triangle represents a seismic station and the red star shows the epicenter of the 2015 M_w 8.3 Illapel earthquake.

2.1.4 Back-projection results

The rupture imaging of the M_w 8.3 Illapel earthquake, with both relatively high- (0.25-1 Hz) and low-frequency (0.1-0.5 Hz) energy using the US seismic array shows that the mainshock lasts for about 80 s and is characterized by three rupture patches defined by the locations and amplitudes of the high-frequency sources (Figure 2.3) determined by the back-projection method. There is general agreement between the overall features of rupture propagation as imaged using two frequencies; they vary, however, in details. There

are two strong bursts of seismic radiation during this earthquake (Figure 2.4). Energy peaks associated with the higher frequency band show up earlier than the corresponding lower frequency ones. The first energy peaks in higher and lower frequency bands are around 27 and 42 s, respectively, and the second energy peaks appear at 51 and 60 s. Similar observation for the 2010 M_w 8.8 Maule earthquake is interpreted as high-frequency energy release due to the breaking of the fault at the rupture tip, followed by slower slip behind the rupture front due to reduced friction (*Kiser and Ishii*, 2011). The stacked normalized amplitude shows the first energy burst dominates the energy radiation for the higher frequency band; while for the lower frequency band, the second energy burst is stronger.

To determine whether the lag of the low frequency energy radiation reported in the manuscript is an artifact of depth phases or 3-D structure, we compare the energy radiation pattern for multiple aftershocks using the back-projection method. The selected aftershocks have similar thrust mechanisms and are close to the mainshock. The result for the M_w 7.0 aftershock (latitude -31.2622; longitude -71.4262; depth 28.41km from USGS) is shown in figure 2.5. The figure shows both frequency bands have the same pace of energy radiation, even though the low frequency results show relatively higher energy radiation during 18-27 s. It is in contrast to the results of the mainshock, in which the higher frequency energy radiation precedes the lower frequency results by 9-15 s. Thus, it seems that it is the different source mechanism that causes the high frequency precedence, and the artifacts of depth phases or 3-D structure have little effect on the back-projection results.

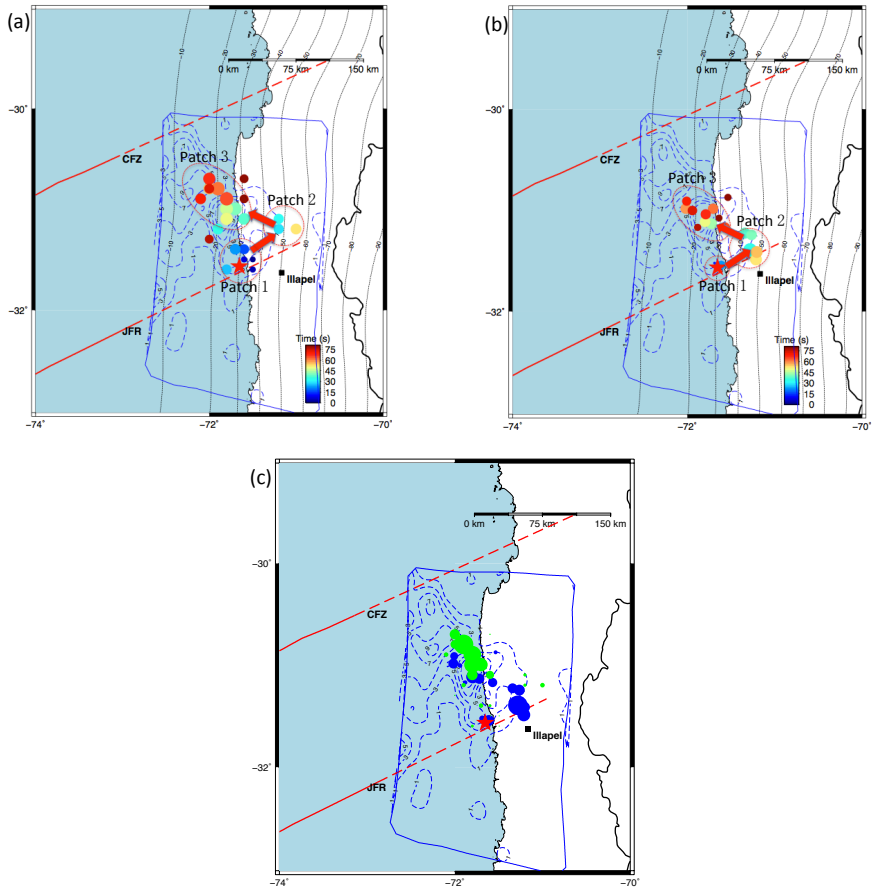

Figure 2.3: (a) Rupture process of the 2015 M_w 8.3 Illapel earthquake. Colored circles represent the locations of the peak energy during the mainshock using the back-projection method (lower-frequency band, 0.1-0.5 Hz), color-coded in time. Circle size is scaled to the normalized energy. The blue box represents the slip inversion model region (*Melgar et al.*, 2016). The blue dashed lines show the slip contours starting at 1 m with 2-m intervals. The red solid lines show the Challenger fracture zone (CFZ) and the Juan Fernandez Ridge (JFR) with the dashed line marking the extension of the ridge (*Métois et al.*, 2012). The red dashed circles show three rupture patches with arrows showing the propagation direction determined by our back-projection results. (b) Rupture process of the 2015 M_w 8.3 Illapel earthquake with higher-frequency band (0.25-1 Hz). Symbols are the same as in (a). (c) Comparison of rupture propagation of the 2015 M_w 8.3 Illapel earthquake between higher- (0.25-1 Hz) and lower-frequency bands (0.1-0.5 Hz) as imaged by the back-projection method. Blue circles represent higher frequency and green circles show the result of lower-frequency ruptures. The size of the circle is normalized according to the peak energy radiation for the entire event. Other symbols are the same as (a).

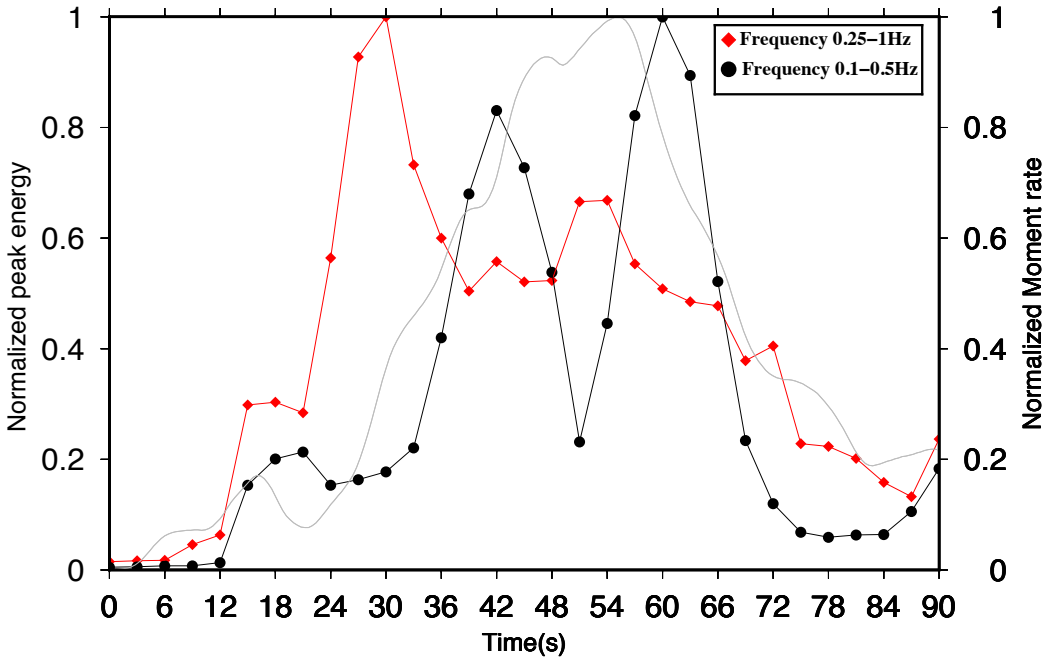

Figure 2.4: Normalized stacked energy as a function of time for the 2015 M_w 8.3 Illapel earthquake using the US stations. Each red diamond and black circle represent the peak stacked energy in the 8-s sliding time windows, with 3 s time steps for the frequency bands of 0.25-1 and 0.1-0.5 Hz, respectively. Red and black lines show the evolution of seismic radiation over the duration of this earthquake, as imaged in this study. The gray line represents the moment rate taken from the United States Geological Survey (USGS) slip model (http://earthquake.usgs.gov/earthquakes).

Both frequency bands resolve three rupture patches in space. The patches appear to be similar to the asperities, and they are referred to as patch 1, 2, and 3 in this article. The rupture propagates about 100 km along strike, with 40-km up-dip and 40-km down-dip movement along the subduction megathrust fault during this earthquake (Figure 2.6). The lower frequency back-projection results show that the rupture breaks patch 1 for about 24 s when near the epicenter, with small up- and down-dip movement (Figure 2.3a, Figure 2.6). This initial phase is characterized by a relatively low level of radiated seismic energy (Figure 2.4). Then, rupture propagates northeast to patch 2, about 67km northeast of from the

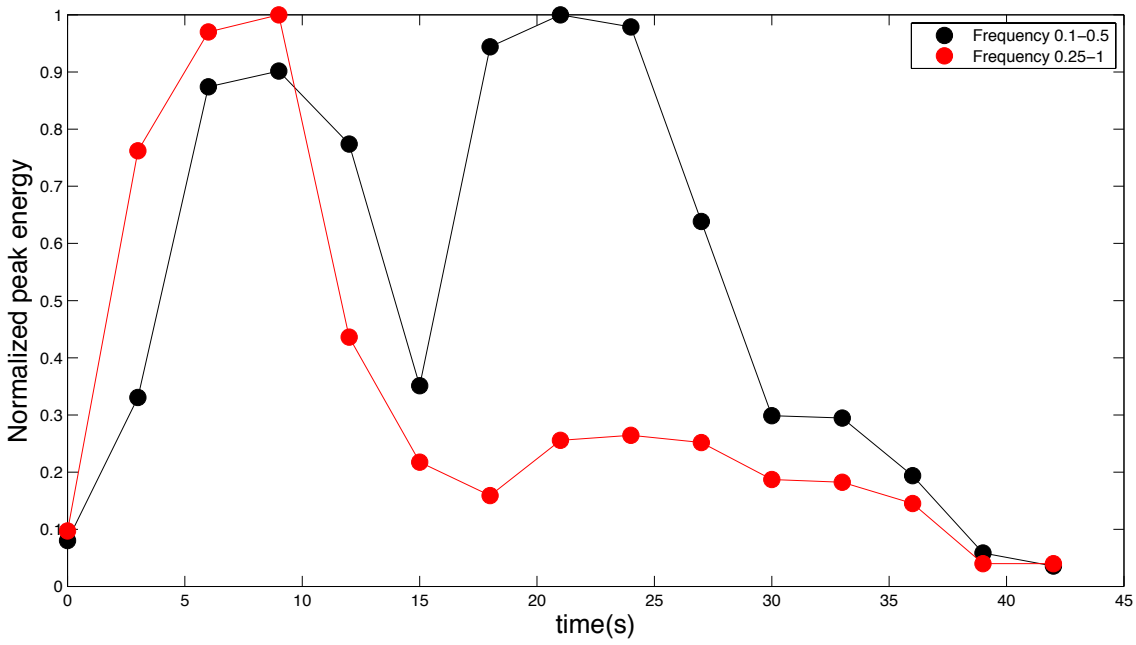

Figure 2.5: Normalized stacked energy as a function the time for the M_w 7.0 aftershock using US stations. Each red circle and black circle represent the peak stacked energy in the 8 s sliding time windows, with 3 s time steps (same as that for the mainshock) for the frequency bands of 0.25-1 Hz and 0.1-0.5 Hz, respectively.

epicenter. This phase is characterized by relatively higher amplitude seismic radiation. The rupture stays in patch 2 for about 27 s, but it is not clearly visible for its entire duration (Figure 2.3a) due to simultaneous strong seismic radiation from patch 3. Patch 3 is located northwest and up-dip of patch 2. Patch 3 starts to rupture 6 s after patch 2 becomes active and continues rupturing to the end of the mainshock. Patch 3 appears to be the strongest patch broken during this earthquake; it produces the highest amplitude and two strong bursts of seismic radiation. The first burst occurs between 33 and 51 s. The energy of radiation increases rapidly and reaches a peak at 42 s, then quickly drops to a lower level. During this period, patch 3 ruptures to the northwest for about 60 km. Another strong energy burst occurs between 51 and 69 s, with radiated energy rising rapidly to reach its

maximum at 60 s. During this time, rupture continuously propagates to the northwest and up-dip. Then, the radiated energy starts to diminish, accompanied by a reversal in rupture direction toward the southeast (Figure 2.3a) in the last 20 s of the rupture. Patches 1 and 3 coincide with areas of intermediate-to-high coseismic slip, as estimated by the fault slip inversion (*Melgar et al.*, 2016) (Figure 2.3a). Patch 2, however, is located down-dip of any significant coseismic slip. The overall pattern of the evolution of seismic radiation over time (the stacked amplitude) during this event generally agrees with the moment rate obtained from the United States Geological Survey (USGS) slip model (Figure 2.4) (http://earthquake.usgs.gov/earthquakes).

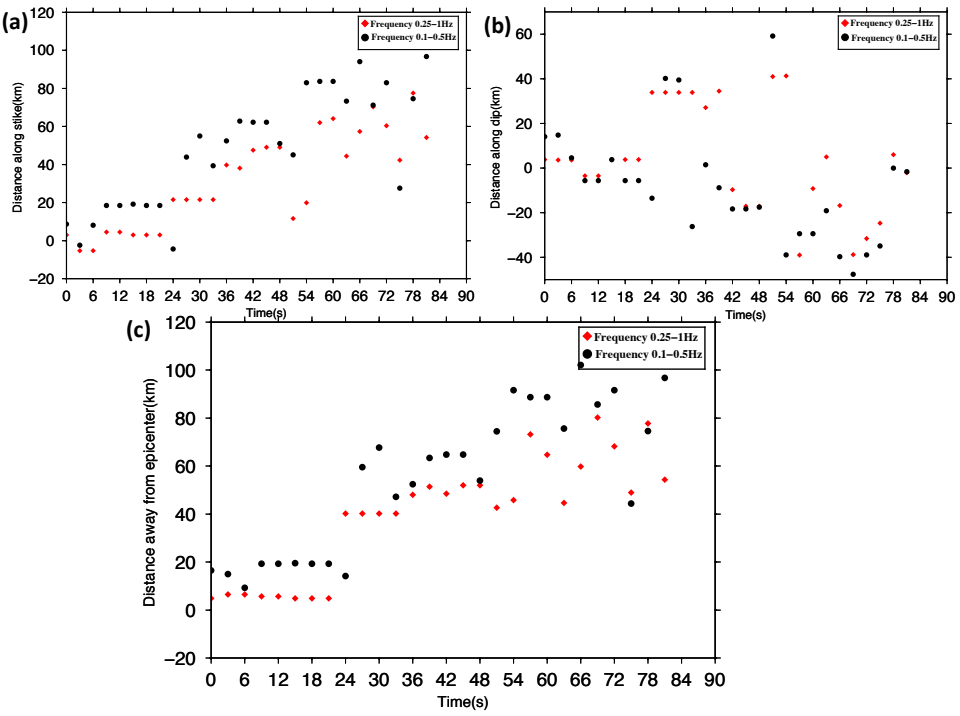

Figure 2.6: Rupture distance along strike, dip and away from the epicenter. (a) Rupture distance along the strike of the subduction zone (strike of 004° from USGS) over time. The red diamonds represent high frequency and black circles represent low frequency results of the back-projection method. (b) Rupture distance along the dip direction of the fault. (c) Rupture distance away from the epicenter of the mainshock.

The higher frequency back-projection results show a similar rupture and energy radiation pattern. There appears to be three rupture patches, in locations similar to those determined from lower frequency radiation (Figure 2.3b). The higher frequency sources are, however, generally located down-dip of the lower frequency sources (Figure 2.6) and do not propagate into the near-trench large slip patch. The first and dominant high-frequency energy burst is located northeast of the epicenter, just down-dip of the 1-m slip contour. Higher frequency sources in the patch 3, located northwest of the epicenter, are also further down-dip compared to the lower frequency sources (Figure 2.3a, b) determined in this study. Thus, the time-integrated spatial distribution of seismic radiation shows a patch of lower frequency radiation located northwest of the epicenter, while most of the higher frequency energy is released northeast of the epicenter (Figure 2.3c, 2.6). Even after considering the effect of the array response functions (ARF), which is elongated in the NWSE direction (Figure 2.7) and has higher resolution in high frequencies, the centroid of integrated higher frequency radiation is clearly down-dip of the lower frequency centroid.

Interestingly, there are two bathymetric features that are subducting near the rupture areathe Juan Femandez Ridge (JFR) to the south and the Challenger fracture zone (CFZ) to the north of the rupture zone. The rupture and aftershocks appear to be bounded by these two strong surface features. In fact, the rupture seems to propagate from patch 1 to patch 2 along the JFR. The rupture breaks patch 1, bounded by JFR to the south, for about 24 s, which is a significant proportion of the total duration. However, it never manages to propagate to the south across the JFR, even though the megathrust fault south of the JFR is highly coupled (*Métois et al.*, 2012).

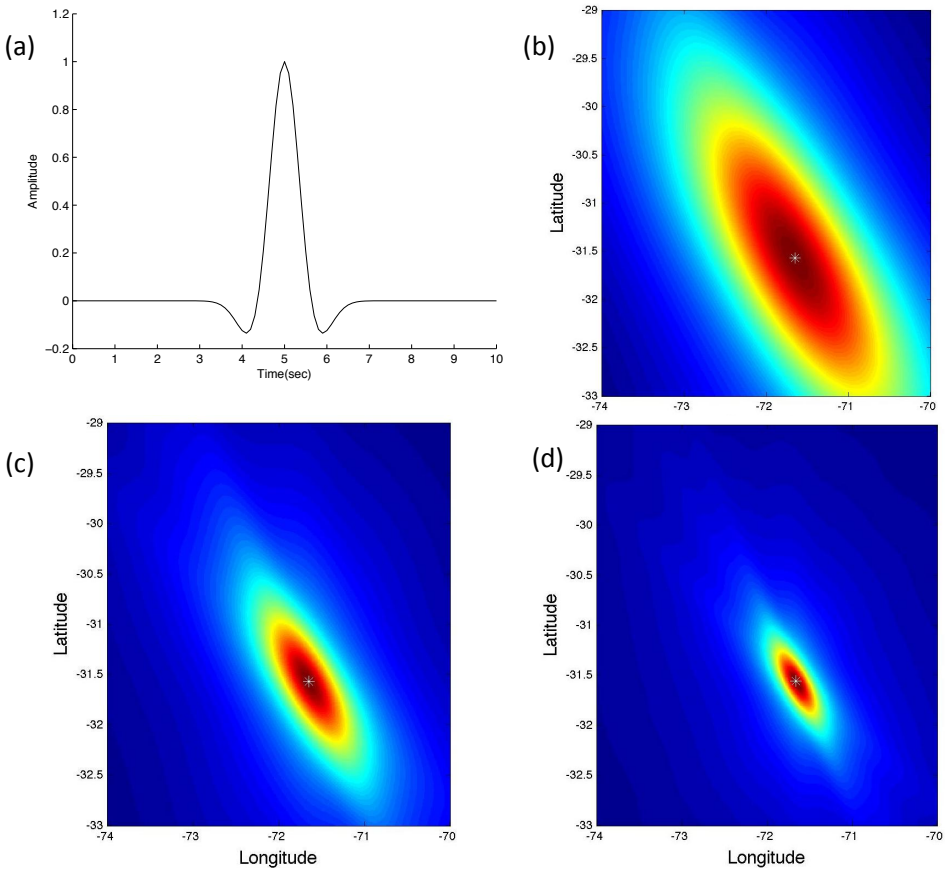

Figure 2.7: Point source energy kernels. (a) The Ricker wavelet example with peak frequency at 0.5 Hz. (b) Back-projection result for a point source (white star) using US seismic arrays synthetic seismograms with a central frequency of 0.2 Hz. (c) The same as (b), except using a central frequency of 0.5 Hz. (d) The same as (a), except using a central frequency of 1.0 Hz.

2.1.5 Discussion

The ChilePeru subduction zone is one of the most active convergent plate boundaries and has produced multiple large earthquakes in the recent past. Ruptures of historical large earthquakes in central Chile generally occur within the highly coupled region, and stop at areas with low-to-average coupling (*Métois et al.*, 2012). The 2010 M_w 8.8 Maule earthquake occurred in the middle of the Maule coupling segment and ruptured the whole

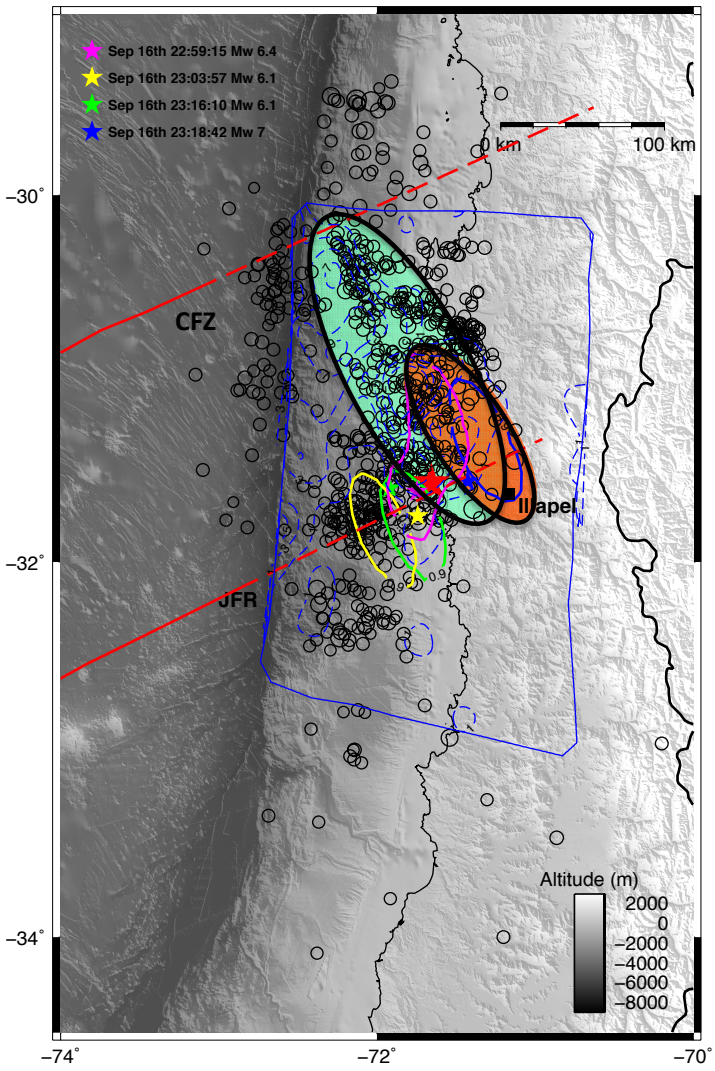

Figure 2.8: Time-integrated images of the seismic radiation using the US seismic stations. Red star indicates the epicenter of the M_w 8.3 Illapel earthquake, and other four colored stars show the epicenters of four early large aftershocks (M $\geq$ 6). The filled green area shows the region with greater than 70% normalized stacked energy from lower frequency seismic radiation. The filled orange region represents the region with greater than 70% normalized stacked energy from higher frequency seismic radiation. Both patches include the effect of array response function. Open circles show aftershock locations from the ANSS catalog between 16 September and 24 November 2015. Solid colored lines show the normalized time-integrated energy from high-/low-frequency seismic radiation during the four early large aftershocks at 90% stacked amplitude, with colors corresponding to the stars for each large aftershock. Other symbols are the same as Figure 2.3a.

area showing above average coupling (75%) to the north and south of the epicenter. The southern rupture extent of the Maule event may be controlled by a visible surface features, i.e., the Mocha Fracture Zone (*Contreras-Reyes et al.*, 2008; *Kiser and Ishii*, 2011). Defined by the amplitude and rupture velocity, the Maule earthquake is divided in three segments (*Kiser and Ishii*, 2011) and shows frequency-dependent ruptures, with higher frequency radiation located downdip and preceding lower frequency radiation. Interestingly, the 2015 M_w 8.3 Illapel earthquake also occurs within a highly coupled zone of the subduction fault, known as the Metropolitan highly coupled segment (*Métois et al.*, 2012). Three rupture patches characterize the Illapel earthquake as imaged by the back-projection method. The patches behave like asperities that rupture during this event. Thus, this event is characterized by breaking of multiple asperities along the subduction thrust. Rupture of patch 1, located near the epicenter, does not propagate to the south, even though it is highly coupled. This may be due to the presence of the Juan Femandez Ridge (JFR), defined by a chain of volcanic domes generated by the magmatic activity related to hot-spot activity (*Huene et al.*, 1997). The thermal anomaly results in a decrease in density of the lithosphere beneath the JFR (*PILGER JR*, 1981), and the interaction of this feature with the overriding plate results in continental crustal uplift and thickening (*Fromm et al.*, 2004). It is also related to the formation of a sediment barrier at 32.5S, which shows a sediment-poor and sediment-rich trench to the north and south, respectively (*Lowrie*, 1981). Thus, the JFR appears to be an important feature (*Marot et al.*, 2013), separating the central Metropolitan segment into two segments, and acts as a barrier for the rupture to propagate to the south and break the southern, highly coupled patch. From patch 1, the rupture propagates

northeast to patch 2, a direction parallel to the northeast trending JFR, before it is stalled at a locale with relatively low coupling. Patch 3 ruptures to the northwest, and is an area characterized by high coupling (*Métois et al.*, 2012). The rupture ceases when it comes to a low coupled region, just southward of the Challenger fracture zone (CFZ) (*Huene et al.*, 1997). This indicates the rupture of large earthquakes in this subduction zones is not only controlled by the seismic coupling, but also strongly affected by the pre-existing bathymetric features. These observations are consistent with the characteristics of the megathrust rupture shown during the Maule earthquake.

The spatial and temporal distribution of aftershocks provides critical information on the fault dynamics and the evolution of the state of stress in the rupture area. According to the Advanced National Seismic System (ANSS) catalog, there were 749 aftershocks greater than magnitude 3.6 within 2 months (Sept 16thNov 24th) following the mainshock. These aftershocks are mainly distributed northwest and southwest of the mainshock. In Central Chile, the rupture zones of large earthquakes appear to occur in a generally along-strike direction (*Kelleher*, 1972) and within the highly coupled region. Most of the aftershocks to the northwest of the mainshock epicenter are within the patch that releases strong low-frequency (0.1-0.5 Hz) seismic radiation (Figure 2.8). The southwest aftershocks cluster in a region, where some early (within 30 min following the mainshock) large ($M_w \geq 6$) aftershocks occur (Figure 2.8). Most of the aftershocks are bounded by the CFZ to the north and the JFR to the south, either within or at the edge of the patch that releases lower frequency energy. These two aftershock areas are also characterized by high coupling in central Chile (*Métois et al.*, 2012). Ridge subduction can significantly affect the stress

field (*Tapponnier and Molnar*, 1976), and may result in a possible increase of post-seismic stress in this region due to the mainshock and early large aftershocks. The rupture and aftershocks of the Illapel earthquake do not break the highly coupled segment located south of the JFR in central Chile (*Métois et al.*, 2012), leaving it vulnerable for another large earthquake in near future.

2.1.6 Conclusions

Central Chile produces frequent large earthquakes partly due to the high convergence rate and strong plate coupling between the Nazca and the South American Plates. We apply the back-projection method using the US seismic array to study the rupture of the 2015 M_w 8.3 Illapel, Chile earthquake that occurred at the southern edge of the 1943 M_w 7.9 Illapel-Salamanca earthquake and the northern edge of the 1985 Ms magnitude 7.8 offshore Valparaiso earthquake. Both lower- (0.1-0.5 Hz) and higher- frequency bands (0.25-1 Hz) of energy show three rupture patches and, generally, similar evolution of seismic radiation. The rupture propagates about 100-km along-strike, 40-km up-dip, and 40-km down-dip away from the hypocenter on the subduction megathrust fault. The rupture patches and rupture propagation appear to be controlled by the highly coupled Metropolitan segment and bathymetric features of the JFR and the CFZ. The higher frequency radiation show an earlier burst (915 s) of seismic radiation than the lower frequency waves, as well as a relatively down-dip location of sources radiating seismic energy. The results of the back-projected aftershocks, with similar thrust mechanisms as the mainshock, show the lag of the low-frequency energy radiation is not caused by depth phases or 3-D structure (Figure 2.5). The major slip patch from the slip inversion model (*Melgar et al.*, 2016) is located

northwest of the mainshock epicenter, and adjacent to the patch producing strong seismic radiation for a significant proportion of the rupture duration as imaged by this study. The aftershocks are distributed northwest and southwest of the epicenter, either within or at the edge of the lower-frequency energy release center. The rupture zone and majority of the aftershocks seem to be bounded by the CFZ to the north and the JFR to the south. The JFR may have acted as a barrier to prevent rupture from propagating to the south, leaving this region under the risk of another large earthquake in the near future.

2.2 Rupture Process Image and Enhanced Aftershock Detection of the 2015 M_w 7.8 Gorkha Earthquake Using Multiple Global Seismic Arrays

2.2.1 Abstract

We use four global arrays to image the rupture process of the 2015 M_w 7.8 Gorkha Nepal earthquake with the back-projection method. The mainshock ruptured about 140 km eastward along the Main Himalayan Thrust (MHT) fault with an average velocity around 2.3 km/s. Back-projection results from certain arrays show a northeast branch rupturing about 45 seconds after the initiation of the mainshock. Using the same technique and arrays, we detect and locate aftershock activity within 19 days following the mainshock. Although the majority of these events are already recorded in the global earthquake catalog (the Advanced National Seismic System, ANSS catalog), we have found hundreds more. Aftershocks detected by the arrays share the same general east-west trend as existing cata-

logs. The majority of aftershocks are located at the eastern edge of the rupture region and surround the rupture zone of the largest aftershock (M_w 7.3 Kodari earthquake). The newly detected aftershocks are located within the area of coseismic rupture and to the southwest of it. The catalog events not detected by the back-projection method mainly range in magnitude between 4 and 5, similar to the back-projection aftershocks not recorded in the catalog, that range between 4 and 5.5. In comparison to an interseismic coupling model along the MHT fault (*Ader et al.*, 2012), the majority of the catalog aftershocks are found to be distributed in a region with coupling between 0.4 and 0.6, and near 1, the fully locked region, while our back-projection results show most aftershocks located in a zone with coupling ranging from 0.85-1. Despite more aftershocks being located in the coseismic region overall, the majority of them are still distributed around the edges of least coseismic slip.

2.2.2 Introduction

The spatiotemporal distribution of aftershock activity is critical for studying earthquake dynamics and stress transfer (*King et al.*, 1994), especially for large earthquakes. For the mainshocks that occur relatively far away from densely distributed seismic networks, it is difficult to identify all small to moderate magnitude aftershocks. Even in well-instrumented regions it is difficult to detect early aftershocks because they are drowned out by the coda of the mainshock - a complexity due to the simultaneous arrival of various seismic phases of multiple aftershocks and lower signal to noise ratios for small earthquakes (*Kilb et al.*, 2007). This leaves current global aftershock catalogs incomplete, even for moderate sized earthquakes, greater than magnitude 4, and resulting in a delay in detecting the earliest aftershocks.

Located at the boundary between the India and Eurasian plates, the Nepal region is one of the most active seismic zones in the world. Owing itself to the accumulation of high tectonic strain, the central Nepal region has experienced many great and large earthquakes that occurred in 1225, 1344, 1505, 1833, 1934 and 1950. The behavior of the subsequent aftershock sequences from these previous large earthquakes remains poorly studied *Adhikari et al.* (2015) due to the lack of seismic instruments in the area. The most recent large event to occur in this region is the 2015 M_w 7.8 Gorkha earthquake, which occured at 06:11:26 (UTC), April 25th 2015, with an epicenter at $28.147°N, 84.708°E$ (the U.S. Geological Survey, USGS) along the Himalayan front close to Kathmandu. The Gorkha earthquake nucleated at the lower edge of the locked portion of the MHT fault and resulted in more than 9,000 deaths, destroying 490,000 homes and leaving 3.5 million residents homeless (*Bilham*, 2015). Despite the destructive magnitude of this earthquake, it did not fully release the tectonic strain that had accumulated in this region prior to the last large event, which is dated back to at least 1505 or even 1344 (*Grandin et al.*, 2015). Furthermore, the global catalog shows no aftershocks with large slip to release the remaining strain in the shallow part of the MHT. This implies that a large damaging earthquake could happen updip of Gorkha event, in the frontal part of the megathrust sometime in the near future (*Grandin et al.*, 2015). Thus, a detailed study of the aftershocks evolution and stress transfers in Nepal region is necessary to better understand the regional fault dynamics and associated seismic hazards.

Because of the limitations in density and distribution of seismic instruments in the Nepal region, many smaller aftershocks remain undetected (and/or remain proprietary)

by current seismic networks in place. This necessitates the use of teleseismic data and other methods to detect and locate local events. Using the back-projection method, *Kiser and Ishii* (2013) detected a significant amount of aftershocks of the 2011 M_w 9 Tohoku earthquake, especially those not captured by the global seismic network and therefore not included in the global comprehensive seismic catalog. However, their approach in only using one single array, restricts the azimuthal coverage to a relatively small range. In this study, we use four global seismic arrays (US Array, European Array, Japan Array and Austria Array) to detect earthquakes following the 2015 Gorkha earthquake in and around its rupture area, and then analyze and compare the detection results with current existing global catalog.

2.2.3 Data and Method

With limited data from local seismic stations immediately after the 2015 M_w 7.8 Gorkha earthquake, we apply the back-projection method to detect and locate seismicity for 19 days after the Gorkha earthquake. To tackle the issue of insufficient azimuthal coverage, we use data from four global arrays: US Array (US), European Array (EU), Japan Array (JP) and Austria Array (AU). Only stations with relatively high coherence (≥ 0.6)for the first 20 s of the P-wave are selected to avoid the interference of low-quality signals and noise. We use the mainshock as a reference event and apply a cross-correlation method during the first 20s of the high-frequency P wave energy to determine waveform coherency. Based on this, 91, 122, 350, 87 stations with average correlation coefficients above 0.6 from the EU, AK, JP and AU network are selected. The distance ranges for the EU, AK, JP, AU array

are 40-70, 70-85, 35-52, 55-85 degrees, and the azimuth coverage are 294-325, 343.7-32.9, 54.6-73.8, 118.6-151.5 degrees, respectively (Figure 2.9).

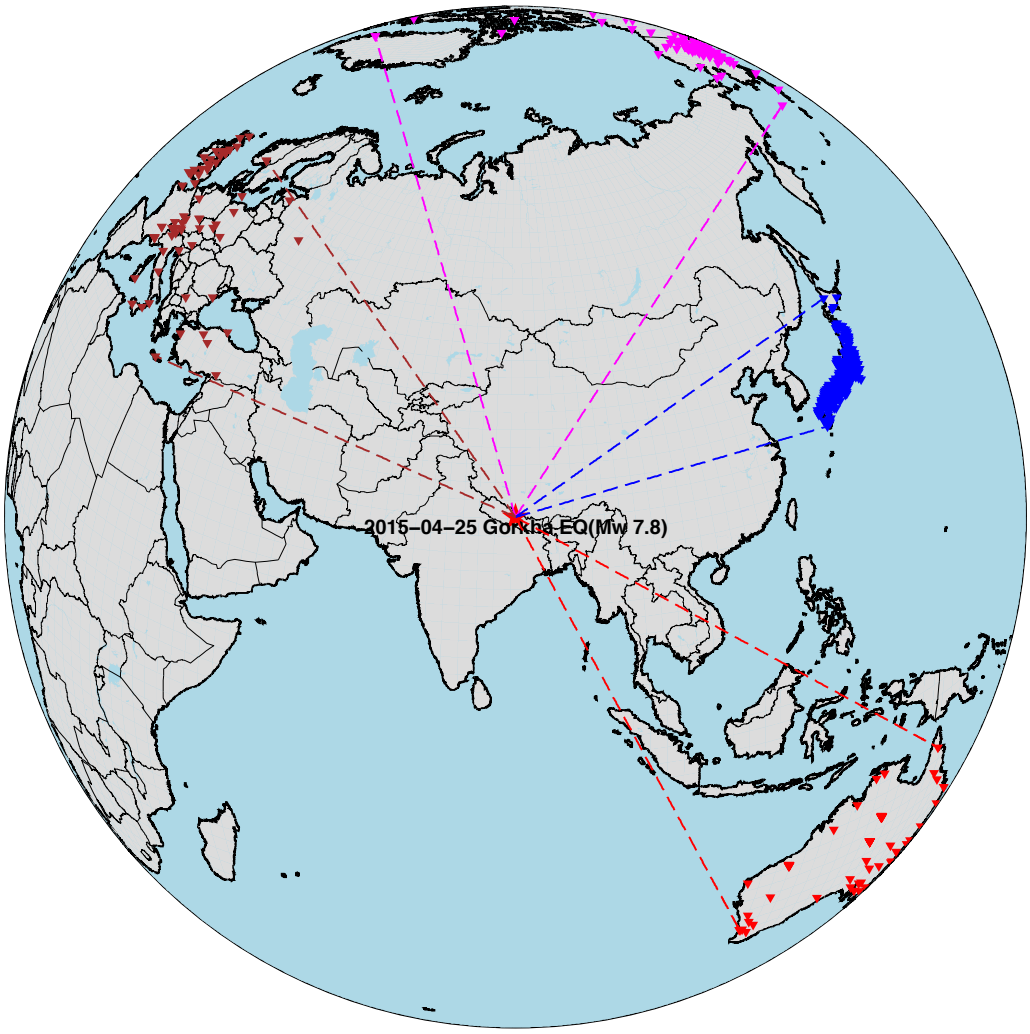

Figure 2.9: Global arrays distribution. The red star in the center shows the epicenter of the April 25th 2015 M_w 7.8 Gorkha earthquake. The red, blue, magenta and brown triangles represent the Australia (AU) Array, Japan Hi-net (JP) Array, Alaska (AK) Array, and the Europe (EU) Array stations, respectively. The corresponding dashed lines show the azimuth coverage.

To improve the azimuthal coverage and the resolution of our back-projection results, we combine these four global arrays. For each array, we select one station with the

highest average cross correlation coefficients with all other stations in the array. Then we use the selected stations from four arrays to make the array relative travel-time calibration. In comparison to the resolution of when only using a single array, the resolution of combined arrays is significantly improved (Figure 2.10).

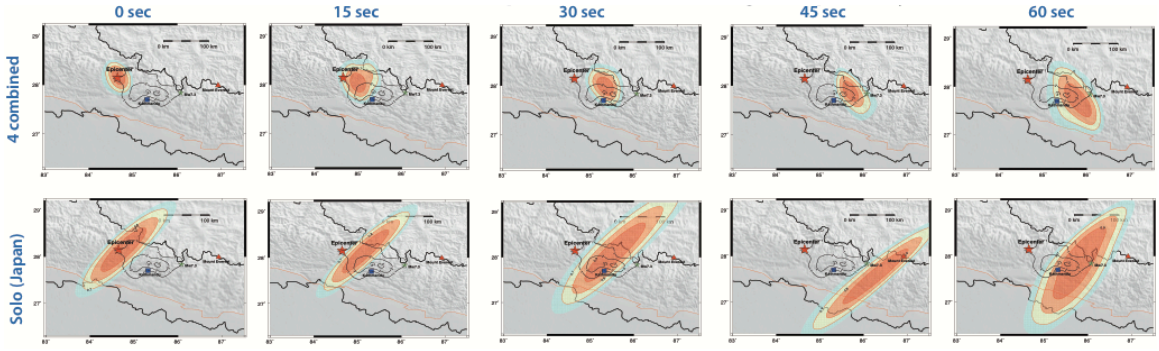

Figure 2.10: The comparison of back-projection results (of the Gokha earthquake) between using a single array (JP array, bottom), versus a combination of four global arrays (top).

The study region for the Gorkha event is defined by the latitude range $26°N$ to $29°N$, and longitude range $83°E$ to $87°E$, with $0.1°$ grid spacing in both latitude and longitude. We use a 1-D velocity model (iasp91) (*Kennett and Engdahl*, 1991) to calculate the theoretical travel time from the source grid to each seismic station belonging to the given array. We use a sliding time window approach, with 20s time-length and 10s time-steps for the continuous data 19 days after the mainshock to detect the seismic activity. For each time window, we calculate the relative energy stacked at each source grid, and then calculate the ratio of peak to average beam amplitude. During an earthquake, the rupture area would show a much higher energy than the background; the use of a short time window means the rupture not propagate far away from the epicenter and limits it to a more precise area comparing to the whole study region, which should result in a higher energy ratio

(Figure 2.11). Some events outside of the study area may exhibit relatively higher energy in the study region because of the array response function (ARF), but this also means the ARF has low resolution and is almost unable to produce high energy ratio. Another way to eliminate regional events and suppress the boundary effect is by omitting detected events within 0.5 degree to the study region boundaries. After testing different thresholds, we set the detection threshold as 5 times the median of the normalized peak energy, and 2.5 times above the median of the energy ratio, for 19 days of continuous back-projection results. Each time window that satisfies both thresholds is considered as a candidate event. The grid node associated with peak energy is recorded as the event location. For some events that last for a relatively long time and satisfy the detection criteria in several consecutive time windows, we consider them as one event if the epicenter locations are within 50km in two successive time windows. We then use the location of peak energy in the first window as the epicenter.

To evaluate the effectiveness of the back-projection method in detecting aftershocks, we compare our catalog with the ANSS catalog. In order to compare these two catalogs, we use both time and location difference to develop the match criteria to check whether they are the same event in both catalogs. If the origin time between the back-projection and catalog events are within 30 s, and their epicentral distances are less than 75 km apart, they are considered the same or matched event. Using these matched events, we then apply a calibration method developed by *Ghosh et al.* (2012) to reduce the systematic bias in the locations due to varying source depth, 3-D velocity structures and anisotropy along the travel path from the source to each station at their respective array.

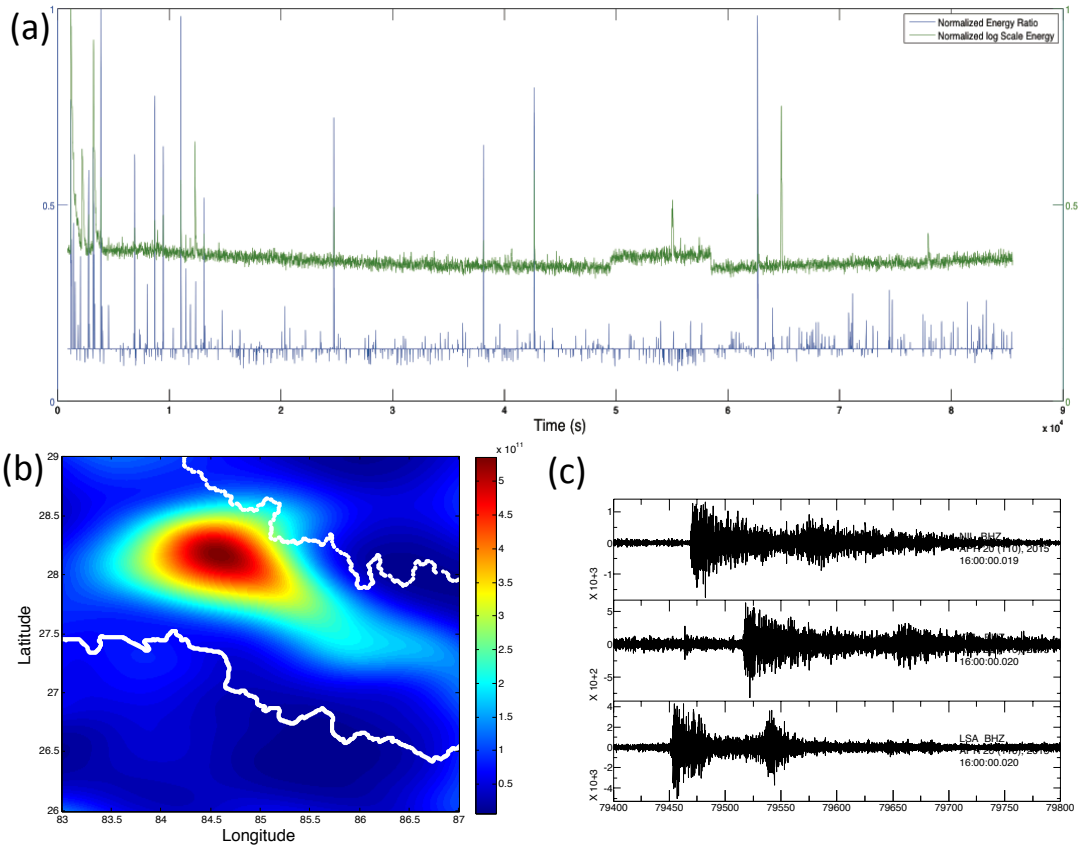

Figure 2.11: Hidden earthquake detection. (a) The normalized log scale of peak energy (green) and normalized energy ratio (blue) for the back-projection results. According to manual checks, we set the detection threshold as 5 times the median normalized peak energy and 2.5 times above the median energy ratio. (b) An example of the back-projection results for a hidden earthquake detection showing a unique energy center. (c) The seismograms of 3 nearby stations (within 15 degrees) from the detected event.

2.2.4 Results

We first apply the back-projection method to study the rupture propagation of the mainshock and the largest M_w 7.3 aftershock using the global arrays. The dense distribution of stations, high signal-to-noise ratio and cross-correlation coefficients, allows us to achieve a high frequency filter of 0.25 to 1 Hz. For the mainshock, each individual array shows similar along-strike rupture propagation to the east (Figure 2.12). However, each single array has

a limitation of azimuth coverage and would result in low resolution and possible artifacts due to azimuthal gaps, and show variations in details. The AK, JP and AU arrays show a branch rupturing to the northeast at around 45 seconds after the start of the mainshock, while the EU array alone shows only continuous propagation to the east. In comparison to a slip inversion model developed by the USGS, the back-projection results show that the higher frequency radiation (rupture front) migrated about 20-30km downdip, coincidently propagating along the 2m-slip contour.

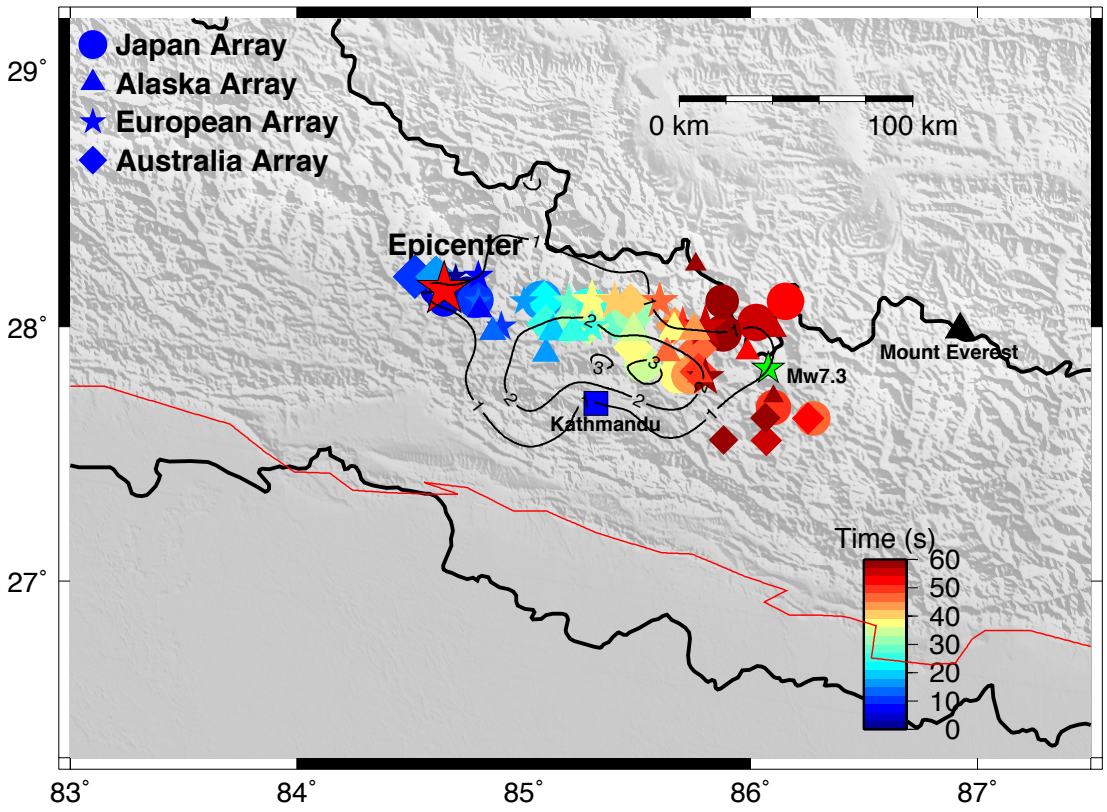

Figure 2.12: Rupture process of the M_w 7.8 Gorkha earthquake imaged by four global arrays, in frequency band 0.25 to 1 Hz. The red line marks the surface trace of the MHT fault (*Taylor and Yin*, 2009). The black contours show the slip contours from the inversion model developed by the USGS.

The back-projection results of combined arrays show that the mainshock ruptures 140 km eastward along the fault with average velocity around 2.33 km/s. the rupture also propagated updip slightly at the beginning and then reversed direction downdip (Figure 2.13). According to the interseismic coupling model along the MHT fault (*Ader et al.*, 2012), the Gorkha earthquake ruptured a highly coupled region along strike in the first 35 seconds, then it ruptured into a less-strongly coupled area where it terminates (Figure 2.13).

17 days after the Gorkha earthquake, there was a M_w 7.3 aftershock that occurred at the eastern edge of the mainshock rupture zone. The normalized time-integrated energy distribution shows that the majority of energy emitted by the mainshock is released about 75km east of the epicenter and 50km north of Kathmandu, while the energy release of the M_w 7.3 earthquake is concentrated around its own epicenter (Figure 2.14).

In addition to imaging the rupture process of the mainshock, the back-projection method is also applied to search for the aftershocks. We detect 568 aftershocks within 19 days (April 25^{th} to May 13^{th}) following the 2015 Gorkha earthquake (Figure 2.15), while in the ANSS comprehensive earthquake catalog only 226 aftershocks are recorded during the same period. Each day, the back-projection method detected more events than the global catalog, especially right after the mainshock (April 25^{th}) and the largest M_w 7.3 aftershock (May 12^{th}). The total number of aftershocks detected by the back-projection method is about 2.7 times that detected by the ANSS catalog events.

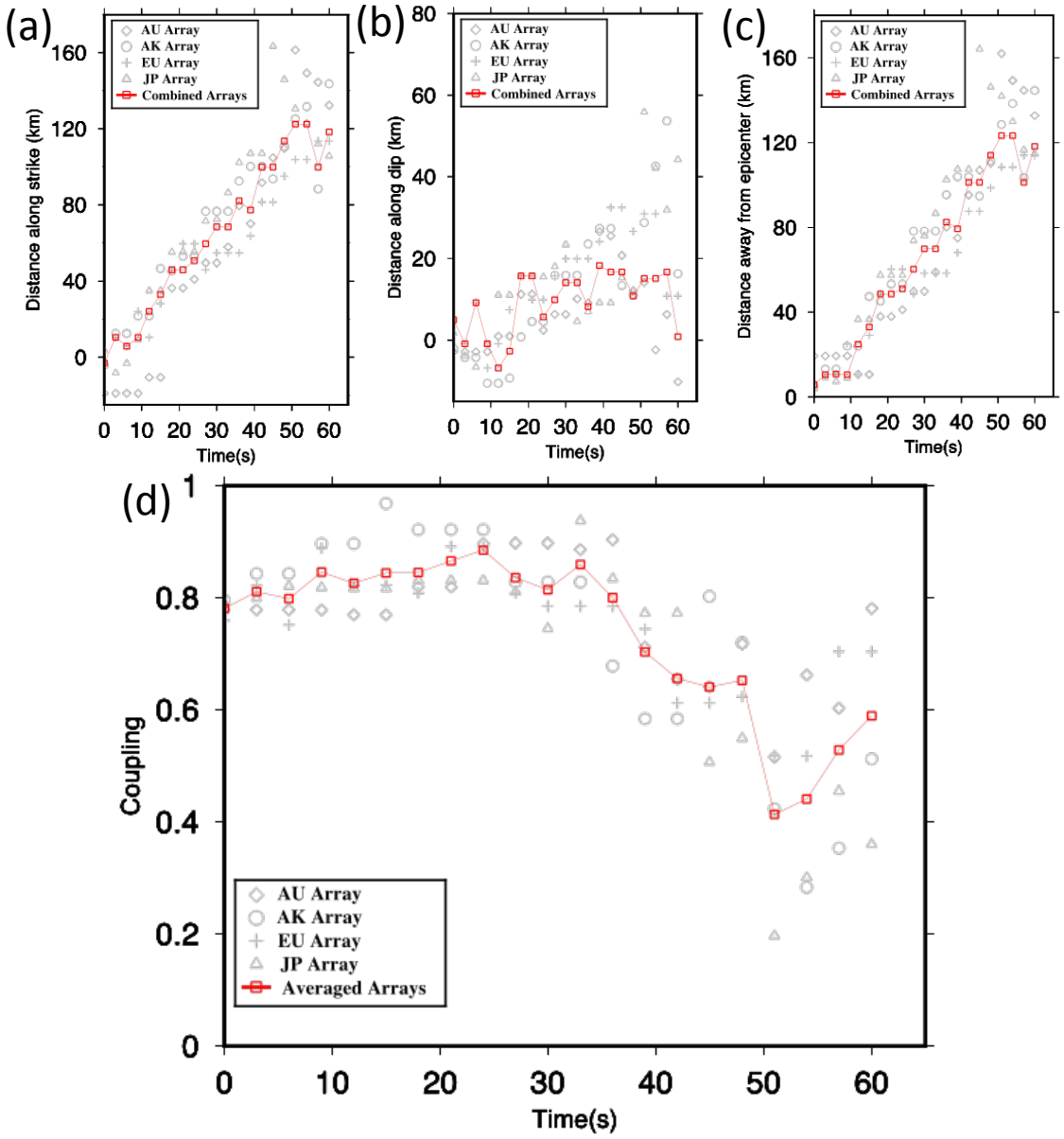

Figure 2.13: The rupture process of the Gorkha earthquake. (a) The rupture front along-strike of the MHT fault. (b) The rupture front along-dip of the MHT fault. (c) The rupture front away from the epicenter of the Gorkha earthquake. (d) The coupling change of the rupture front.

With the matching criteria described before, 176 of 226 (77.9%) ANSS global catalog events within 19 days following the mainshock are detected by the back-projection

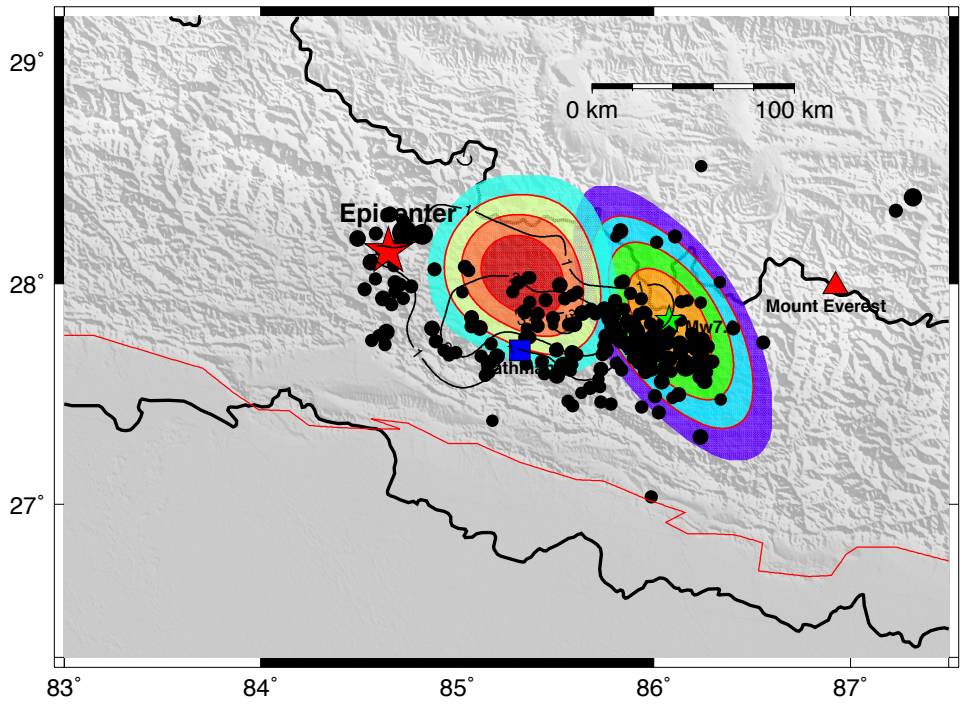

Figure 2.14: Time-integrated energy distribution for the Gorkha earthquake (red star) and the largest aftershock (green star). Each black circle represents an aftershock that occurred from April 25th to May 13th within the complementary ANSS catalog. The colored contours show the normalized time-integrated energy, starting at 60% of the peak energy and 10% increment, with the red center contours for the mainshock and orange center for the M_w 7.3 aftershock. Each time-integrated energy radiation contour is normalized by its own energy radiation.

method (Figure 2.16). Using global arrays, we detect all the ANSS catalog events with magnitude above 5.2 except the M_w 6.1 event, located near Kathmandu. This event is recorded as a local magnitude (ML) 6.0 aftershock in the National Seismological Center (NSC) as well, but with an epicenter located 101km from that in the ANSS catalog. Thus the reason that back-projection method missed the M_w 6.1 ANSS catalog event is that its location is far away from the true location, beyond our matching criteria. Most of the undetected ANSS catalog events are within a magnitude range between 4 and 5 (Figure 2.17), and distributed near Kathmandu and the epicenter of M_w 7.3 Kodari aftershock.

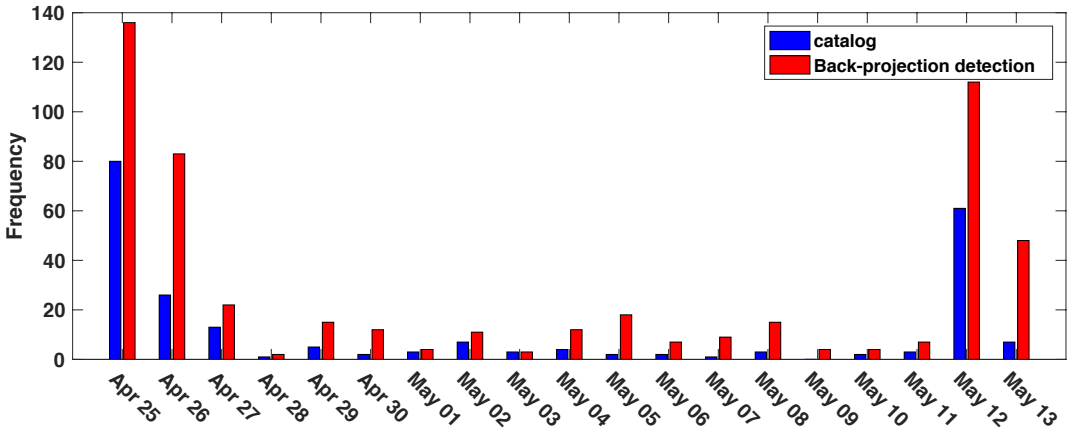

Figure 2.15: Daily seismicity rate in the catalog and back-projection detection of 19 days after the Gorkha earthquake.

Besides the catalog events, there are 392 detected events recorded in our global arrays catalog, which are 173% more aftershocks than that of the global catalog.

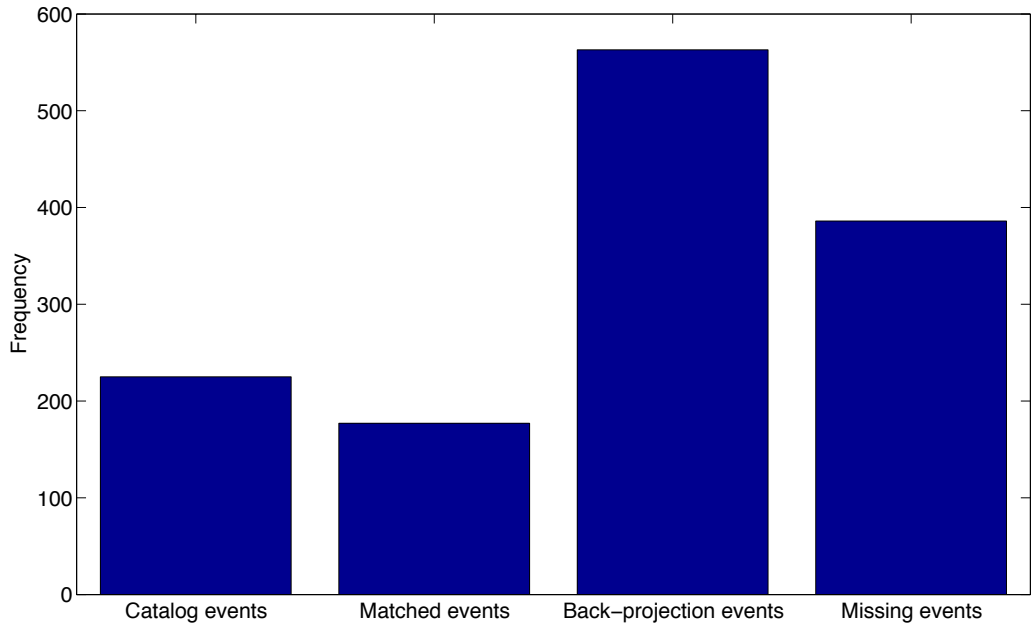

Figure 2.16: Comparison between catalog and back-projection detection results. The missing events mean the events detected by the back-projection but not recorded in the catalog.

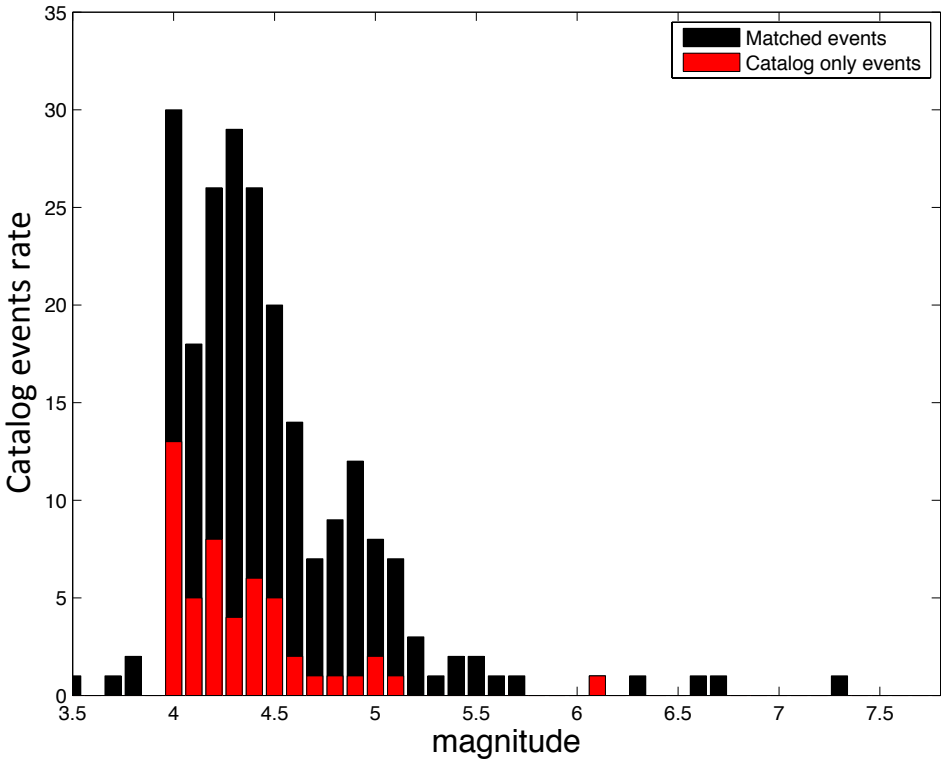

Figure 2.17: Seismicity rate versus magnitude for back-projection events and those in the ANSS catalog.

Using the matched event pairs, we are able to empirically estimate the magnitude for our hidden events by finding the relationship between the peak-beam power (summed up squared velocity seismograms) during the event time against the catalog magnitude. Figure 2.18 shows the log scale of back-projection peak energy of the ANSS catalog events with respect to the catalog magnitude. We try to best fit the data in a least-squares sense using both linear and parabolic functions. Both show similar results, especially between events with magnitudes ranging between 4 and 5.5. We prefer the parabola fit not because of its lower misfit, but also it kind of making up the energy radition of large earthquakes,

which has longer duration than our back-projection time window (20 s). It shows that the majority of hidden aftershocks range in magnitude between 4 and 5.5 (Figure 2.19).

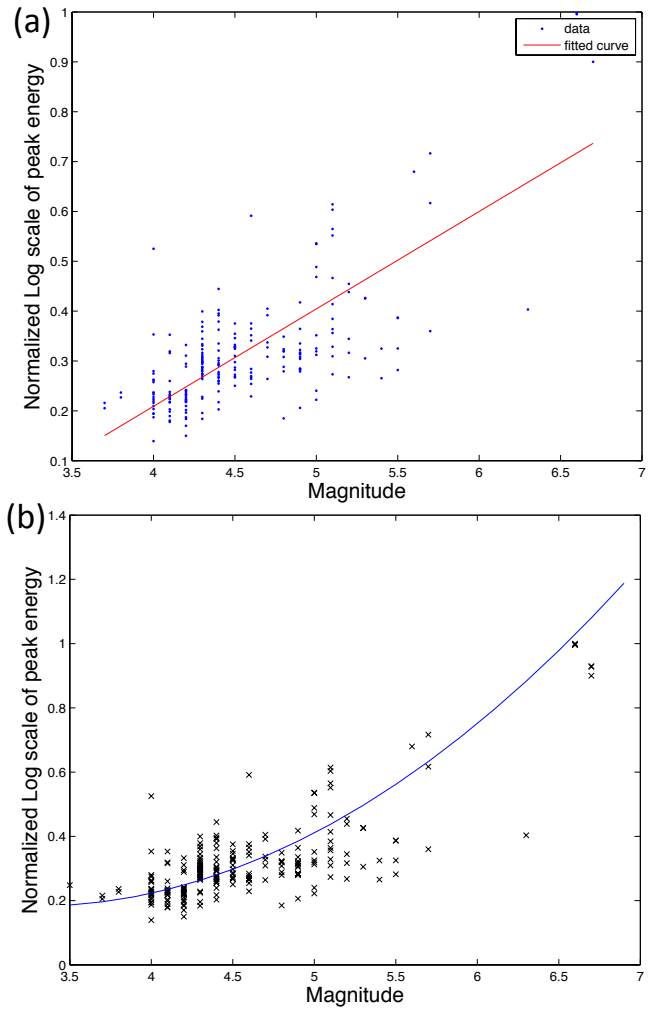

Figure 2.18: Normalized log scale of back-projection peak energy with respect to the ANSS catalog magnitude. (a) Linear best-fit line for the matched aftershocks. (b) The best-fit parabola for the matched events.

The back-projection events are distributed in a narrow band about 75km along dip and 200km along strike of the MHT (Figure 2.20). Most of the catalog aftershocks are distributed around the western and eastern edges of the mainshock rupture zone, and in the

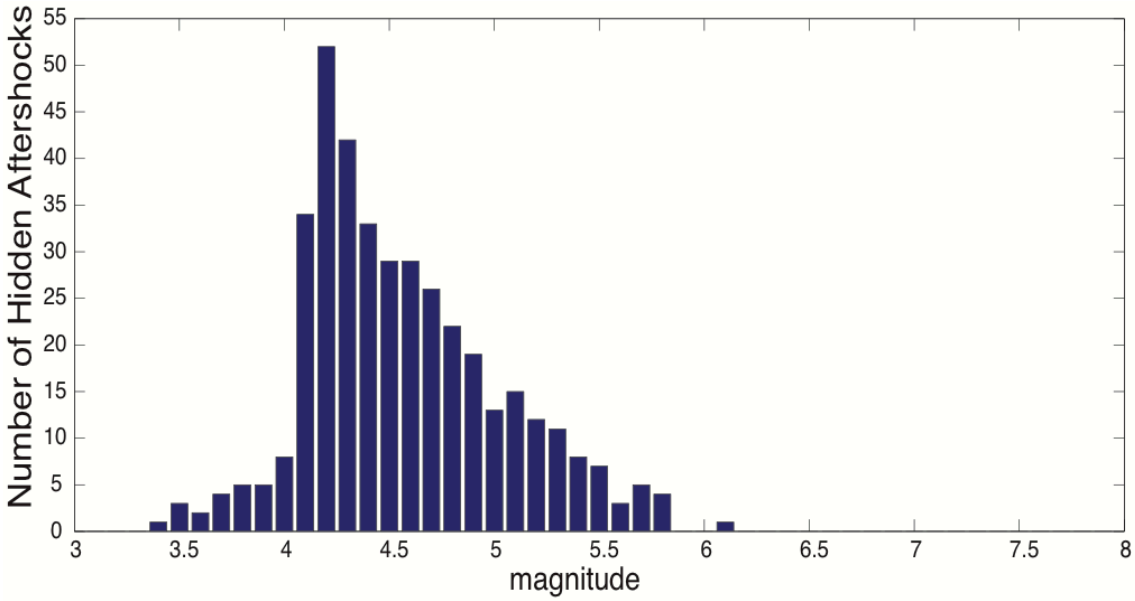

Figure 2.19: Magnitude distribution of hidden aftershocks detected by the back-projection method.

rupture zone of the M_w 7.3 aftershock (Figure 2.14). The rest are distributed throughout the mainshock rupture area. Similar to the global catalog distribution, the back-projection events also show an east-west distribution along strike, with majority of the aftershocks around the rupture zone of the M_w 7.3 aftershocks. They also shows many more aftershocks within the coseismic rupture area, and a NE-SW narrow band of aftershock distribution (Figure 2.20).

With respect to the interseismic coupling information (*Ader et al.*, 2012), the global catalog aftershocks and back-projection detections differ spatially. The catalog events mainly distributed in a region where the coupling value is above 0.4. Aftershocks right after the mainshock quickly occupy a region where coupling ranges from 0.6 to 1, and the aftershocks following the M_w 7.3 event are located in an area where coupling varies

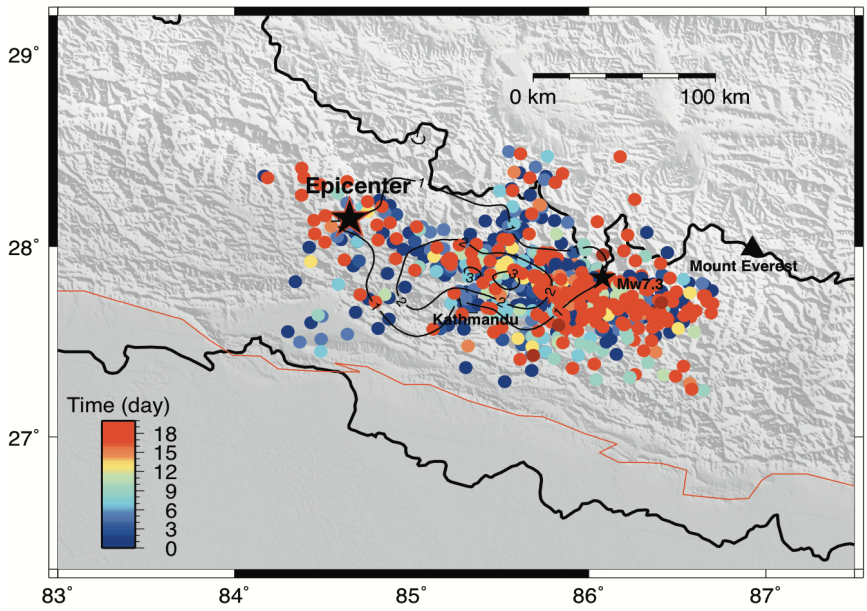

Figure 2.20: Locations of aftershocks detected by the back-projection method.

between 0.4 and 0.7 (Figure 2.21). The catalog aftershocks between these two large events are distributed in two narrow bands. One band is almost fully locked, with the coupling values near 1, and the other with coupling values in the range 0.6-0.7. While for the back-projection events, more aftershocks are located in a coupling region with values above 0.9, and the rest are almost evenly distributed in the region with coupling values 0.4-0.8 (Figure 2.21).

2.2.5 Discussion

The M_w 7.8 Gorkha earthquake provides a good opportunity to study a vigorous aftershock sequence and its potential implications on seismic hazard in the Himalayas. The aftershocks quickly distribute throughout the rupture region. After some time, more

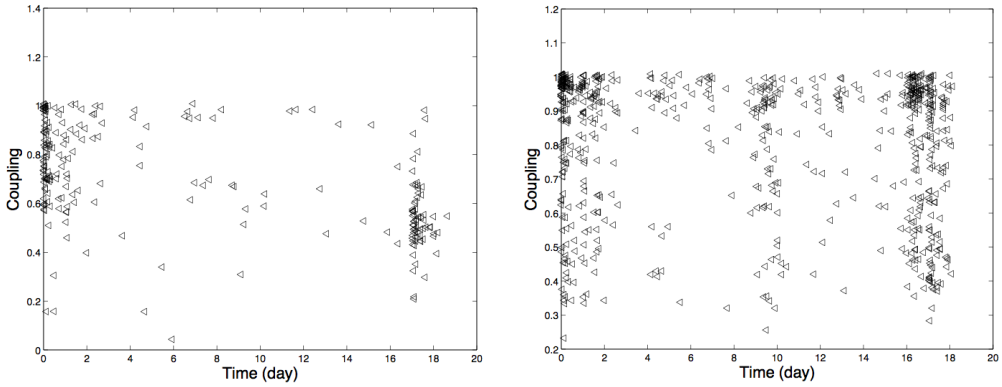

Figure 2.21: Left panel: The interseismic coupling for the catalog aftershocks plotted against time. Each triangle represents one catalog event. Right panel shows as similar plot but for back-projection detections in this study.

aftershocks occur at the eastern edge of the mainshock rupture zone, and form unevenly along strike of the MHT. This may be due to activity on a midcrustal structure (*Adhikari et al.*, 2015), second order structural features, and/or heterogeneities of co- and post-seismic slip (*Avouac et al.*, 2015; *Grandin et al.*, 2015). Many of the aftershocks cluster around the epicenter of the M_w 7.3 Kodari aftershock, which is located at the eastern rupture edge of the mainshock where there is a sudden steeppening of the MHT (*Nábělek et al.*, 2009; *Acton et al.*, 2010; *Caldwell et al.*, 2013). An abrupt geometry change of the MHT may result in high stress concentrations that spawn the high rate of aftershocks around the M_w 7.3 aftershock. About 15% of hidden aftershocks in the back-projection catalog are located to the west and south of the rupture region where coupling is high, and coseismic slip was low. According to the stick-slip frictional instability law of *Brace and Byerlee* (1966) and the seismic coupling relationship between earthquake rupture and seismicity (*Scholz*, 1999), the stress at the edge of the rupture region would increase and the frictional instability would increase within higher coupling areas. This may explain why there are aftershocks

distributed west and south of the cataloged events region. Some of these locations are a result of of the over-calibration for most of the matched events being within or in the eastern edge of the rupture zone, which means the events far from the matched events cluster are calibrated more than that they suppose to. The others are not detectable by the current global catalog due to the limitation of distance and azimuth coverage for the used global array used (*Kiser and Ishii*, 2013), in which few stations are to the south and west of the rupture zone.

The method of using multiple global seismic arrays shows the potential of quickly detecting aftershocks following a large earthquake. It detects about 2.7 times more events than the global catalog for the 19 days of aftershock activities that follow the 2015 M_w 7.8 Gorkha earthquake. In addition to 176 of 226 current catalog events with magnitudes above 3.5 detected, 392 hidden events can be supplemented to current global aftershock catalog. According to the *Gutenberg and Richter* (1956) law, there are many smaller magnitude aftershocks that are still undetectable by array methods, and despite this shortcoming, the back projection shows a much higher capability of detecting aftershocks than global catalog. Therefore, back-projection can still contribute to aftershock studies where there are no local stations, or limited numbers of seismic stations, like at mid-ocean ridges.

2.2.6 Conclusions

The Gorkha ruptured 140 km eastward along the MHT fault and show a branch rupture about 45 seconds after the initition of the maishock. Combining multiple global arrays can significantly improve the azimuthal coverage and the resolution of the back-projection method, and enable a higher detection capability for earthquake detections.

Using the back-projection array method with global arrays, we detect 568 aftershocks within 19 days following the 2015 M_w 7.8 Gorkha earthquake. Our detected aftershocks show an east-west aftershock distribution, similar to the existing global catalog. In addition, a significant number of aftershocks are detected to the southwest, and within the coseismic rupture area. The magnitudes of most hidden earthquakes range between 4 and 5.5, and all the catalog events with magnitude above 5.7 are detected, since the missed M_w 6.1 aftershock turns out to have an incorrect catalog location. The back-projection method using global arrays shows a much higher capability for aftershocks detection for a given region with limited seismic instruments than current catalogs, but a well-distributed local seismic network is still needed in order to detect smaller magnitude aftershocks.

Chapter 3

Near Continuous Tectonic Tremor and Low Frequency Earthquakes in the Alaska-Aleutian Subduction Zone revealed by Array of Mini Arrays

3.1 Abstract

The Alaska-Aleutian subduction zone is one of the most seismically and volcanically active plate boundaries on earth. Compared to other subduction zones slow earthquakes, such as tectonic tremors (TTs) and low frequency earthquakes (LFEs), are relatively

poorly understood due to the limited data availability and difficult logistics of filed efforts. Here we use two data sets- (a) two-month data from one mini array, (b) yearlong data of three mini arrays and five stand-alone stations-to study slow earthquakes in the Unalaska and Akutan region. Using two months of continuous data recorded by a mini array deployed in Akutan Island, we detect an average of 1.3 hours of tectonic tremor activity per day with the beam back-projection method. TTs are clustered in two patches southeast and southwest of Akutan Island, with a $\sim$ 25 km gap in between them. In addition, using three visually identified LFEs as templates, we detect $\sim$ 1300 additional LFEs applying a matched-filter method. Unidirectional tremor propagations are observed both along the strike and dip of the subduction fault, with velocities ranging between 13-110 km/hr.

Using the yearlong data, we detect near continuous tremor activity with three mini arrays, with an average activity duration of 2.7 hours per day. The tremor sources are located offshore to the south of the Unalaska and Akutan Islands, showing locations near or on the subduction surface with a depth range 40-65 km. There are three major clusters, with a $\sim$ 20 km relatively tremor silent segment between the western and middle patch, and a $\sim$ 12 km less active segment between the middle and eastern clusters. The eastern cluster shares the same patch location with the western cluster defined in the two-month data set. Multiple migration patterns, both unidirectional propagation and direction reversal, are observed, with propagation in both along-strike and dip directions, as well as a wide range of velocities. The various migration speeds and directions suggest non-linear rheology and physical asperities along the transition zone in the study region. We also identify tens

of LFE families and use them as templates to search for repeating LFE events with the matched-filter method. Hundreds to thousands of LFEs for each family are detected.

Both data sets show LFEs activity is spatiotemporally consistent with tremor activity. LFEs have a much smaller time interval during tremor signal than LFEs occurring during non-tremor time periods. Tremor clusters in several patches, implying lateral fault heterogeneity with unstable asperities embedded in the more stable fault zone; interactions between these patches are mediated by creep. The density distribution of the tremor sources changes from the creeping segment to the strong asperities in the transient zone of this subduction fault. Tremors and LFEs are more active in the western patch, suggesting a higher slip rate of the plate subducting to the west of the study region.

3.2 Introduction

Tectonic tremor (TT) is characterized by a non-harmonic emergent signal of sustained amplitude lasting from minutes to days, and sometimes for months or longer. It was first observed in the Nankai trough subduction zone in southwest Japan (*Obara*, 2002), and soon after tremor was distinguished in other subduction zones, including Cascadia (*Rogers and Dragert*, 2003), Mexico (*Payero et al.*, 2008), Costa Rica (*Thorwart et al.*, 2007), and Alaska (*Peterson et al.*, 2011; *Brown et al.*, 2013). Studies show that TT is not limited to subduction environments. It is also observed along the San Andreas Fault (SAF), a continental transform plate boundary fault (*Ellsworth et al.*, 2005; *Nadeau and Dolenc*, 2005; **?**), and beneath the central Range in Taiwan, an arc-continental type collision environment (*Peng and Chao*, 2008). Tectonic tremor, (TTs) or non-volcanic tremor, low

frequency earthquakes (LFEs), very low frequency earthquakes (VLFEs), and episodic slow slip events (SSEs) are observed as coupled phenomena in many subduction zones (*Brown et al.*, 2009; *Ghosh et al.*, 2012, 2015; *Hutchison and Ghosh*, 2016; *Shelly et al.*, 2006). TTs have been observed to be triggered by tiny tidal stress and dynamic stress from passing teleseismic waves (*Ghosh et al.*, 2009; *Rubinstein et al.*, 2008; *Thomas et al.*, 2013). TTs are typically known to occur during episodes of SSEs on fault segments downdip of the seismogenic zone (*Rogers and Dragert*, 2003; *Shelly et al.*, 2006). Different models are proposed to explain these phenomena collectively known as slow earthquakes (*Gershenzon et al.*, 2011; *Ide et al.*, 2007b). LFEs are thought to be generated by slip on relatively small on-fault asperities (*Ide et al.*, 2007a; *Royer and Bostock*, 2014). There is evidence that LFEs comprise at least a portion of tremor, and the LFEs occur on the plate interface, coincident with the inferred zone of slow slip (*Frank et al.*, 2013, 2015; *Shelly et al.*, 2006, 2007b). Thus, more detailed studies of tremor and LFEs in the subduction zones will help indicate the mechanism of tremor, constrain the depth of slow slip events, and delineate the transition zone and plate interface more accurately. Previous studies imply that TT, generally with the coupled phenomenon of slow slip events (SSEs), can transfer stress to the updip portions of the fault, and may clock advance or trigger earthquakes in the seismogenic zone (*Mazzotti and Adams*, 2004). Thus, detailed study of tremors and SSEs can help researchers understand potential stress changes in the subduction zones, and provide a new way for early warning of seismic hazard. Compared to other subduction zones, investigating tremor and LFEs along the Alaska-Aleutian subduction zone is more challenging due to the

harsh weather conditions, limited land and seismic station coverage, and the interference of volcanic activities.

The 3800 km Alaska-Aleutian subduction zone forms the northern plate boundary between the Pacific and North American plates (*Ruppert et al.*, 2007). It has segments with different plate motion direction and velocities, and is both very seismically and volcanically active. Within the last 80 years, four large earthquakes with $M_w \geq 8$ have occurred: 1938 M_w 8.2 Shumagin Islands, 1957 M_w 8.6 Andreanof Islands, 1964 M_w 9.2 Good Friday, and 1965 M_w 8.7 Rat Islands (*Brown et al.*, 2013) (Figure 3.1). TTs and LFEs have previously been identified in south-central Alaska and along the Alaska-Aleutian Arc (*Brown et al.*, 2013; *Gomberg and Prejean*, 2013; *Peterson et al.*, 2011). Their spatiotemporal distribution, however, is poorly known due to the limited number of tremor/LFE studies in this area.

Here, we focus our study region near the Akutan Island and Unalaska Island, where land coverage is available and there is a small airport for relatively easier logistics. We first show the detection and location results of TTs and LFEs using two months of high-quality continuous seismic data recorded by a mini array (array stations distributed within a small aperture of typically a few kilometers) deployed on Akutan Island. Then we present the results using the yearlong data recorded by three mini arrays. We detect and locate TTs and LFEs, analyze their spatiotemporal distributions, and explore relationships between them. In addition, we compare their locations with the rupture zone of the 1957 M_w 8.6 earthquake in this region. Finally, we discuss possible explanations for the observed distribution of TTs and LFEs in the study area, and the possible implications for the physical properties of the subduction fault.

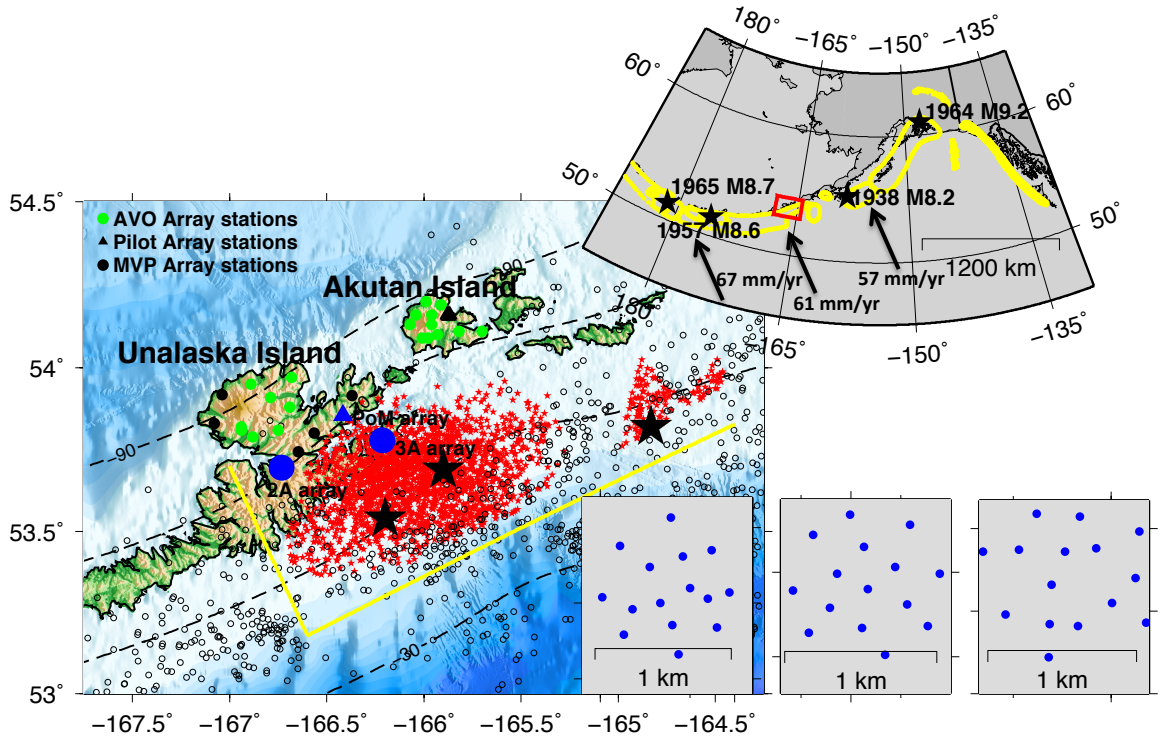

Figure 3.1: Left: Seismic array and tremor distribution. Each red star represents the location of a one-minute tremor signal determined by the beam back-projection method using the two-month continuous data recorded by the Pilot array in 2012 (*Li and Ghosh*, 2017). The black stars show three visually detected LFEs located using arrival times of body waves. The yellow lines are used to calculate the along-strike and along-dip distance of tremor source migration. The contour lines show the depth of the subduction interface according to the United States Geological Survey (USGS) slab model (*Hayes et al.*, 2012). The black open circles show the Advanced National Seismic System (ANSS) catalog earthquakes (01/01/2002 - 10/01/2016) located near the subduction surface. The right bottom panel shows the distribution of the 2A, 3A and PoM array stations, respectively. The right top figure shows the Alaska-Aleutian subduction zone, with the yellow dotted closed lines showing the rupture zones for larger earthquakes (*Brown et al.*, 2013). The red box shows our study area, which is located along the eastern edge of the 1957 M 8.6 and to the west of the 1938 M_w 8.2 megathrust earthquakes.

3.3 Data and Method

In this study, we first use a dense mini seismic array designed with 11 three-component stations deployed on Akutan Island in 2012. The array was operational for

two months from early July to September. The mini array technique has been successfully applied to detect and locate tremor activity in Cascadia and along the San Andreas Fault (*Ghosh et al.*, 2012). It is also logistically easier to deploy and service mini arrays rather than a conventional seismic network, particularly in the Alaska-Aleutian subduction zone due to rough, unpredictable weather and challenging terrain. Using this mini array, we detect prolific tremor activities, with majority of them located close to the Unalaska Island. Thus, to better study slow earthquakes and understand their physical characteristics in the study region, especially to constrain the depth of TTs and LFEs, we have deployed a hybrid array of arrays, consisting of three well-designed mini seismic arrays (2A, 3A and PoM) and five stand-alone stations, in the Unalaska Island since 2014 (Figure 3.1). 2A, 3A and PoM mini array consist of 15, 15 and 18 stations, respectively. Their operation periods are from June 2015, June 2015, and June 2014 to July 2016, respectively.

For tremor detection, we apply the beamforming method to automatically scan the continuous seismic data collected by mini arrays. The beam back-projection method consistently shows higher tremor duration than visual detection or the envelop cross-correlation method used in the Cascadia subduction zone (*Ghosh et al.*, 2009, 2012). We divide the continuous data into 30s time windows and run the beamforming for each time window to get the slowness and azimuth information of the signals, while we use a 1-minute independent (no overlap) sliding time window for the two-month data. Compared to regular local earthquakes, the tremor signal in Unalaska and Akutan region generally has a longer duration (Figure 3.2). Thus, to remove the earthquakes from the tremor detections, we treat the signal as tremor when it shows nearly consistent slowness (+/- 0.02 s/km) and

azimuth (+/- 10 degrees) in continuous 5 time windows, with one time window exception considering the possible interference from other types of signal during the 2.5 minutes.

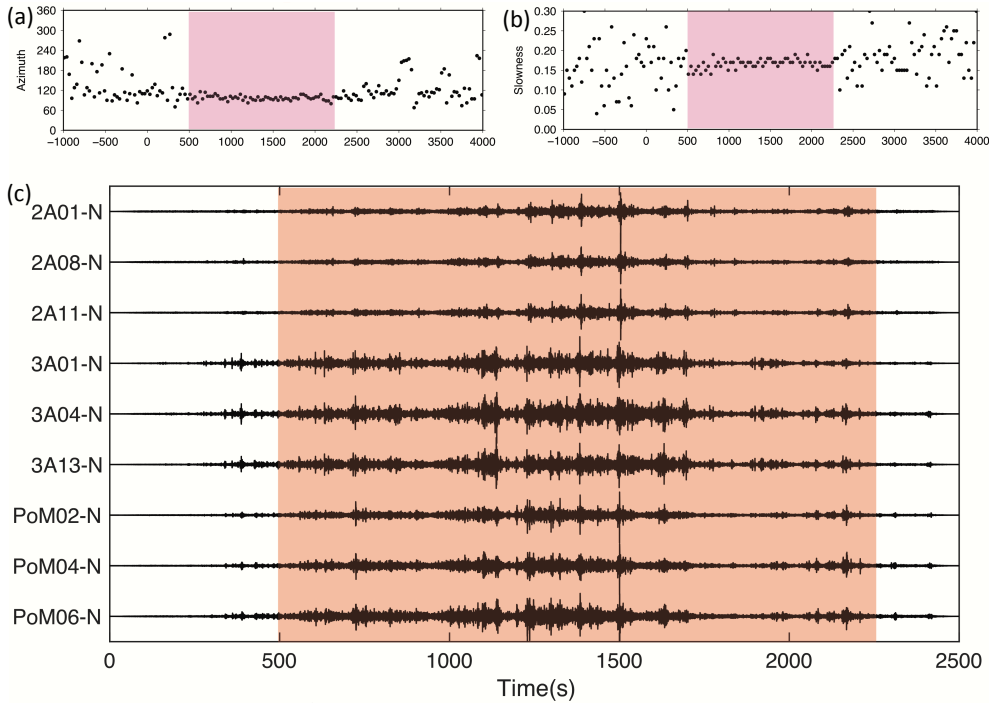

Figure 3.2: Tremor Example. (a) Azimuth distribution before, during and after the tremor signal. The shaded pink area marks the time period for the tremor signal. (b) Same as (a) but for the slowness before, during and after the tremor signal. (c) Seismograms showing the tremor signal filtered in 2-8 Hz. The array and station names are on the left outside. The orange shaded area bounds the same time as the pink shaded are in (a) and (b).

To locate tremor sources, we first divide the study region into 0.01 latitude degrees by 0.01 longitude degrees by 0.5 km depth grids, and then calculate the slowness and azimuth for all the grid points to the array center of each mini array using a 1-D velocity model (*Fogleman et al.*, 1993). For tremor signal detected by only one mini array, we trace the slowness and azimuth along the grid trace until it reaches the subduction interface, which is from the United States Geological Survey (USGS) slab model (*Hayes et al.*, 2012),

assuming the signals are from the slab interface. The tremor sources determined by multiple mini arrays using multibeam backprojection (MBBP) (Figure 1.3) suggest they are located near the subduction interface; thus, it is appropriate to make such an assumption. In addition, we use the bootstrap method to estimate the location uncertainties. For each detection, we do the beamforming 105 times, each with a combination of 13 out of 15 stations. Then we remove the outliers and use the mean value of the clustered slownesses to represent the tremor signal and estimate the slowness uncertainties. Finally, we perform ray tracing to estimate the location uncertainties. Each array is calibrated applying an empirical calibration function calculated using regular earthquakes near the subduction interface (*Ghosh et al.*, 2012). When more than one mini array detects the tremor signals, we use the slowness and azimuth values from the beamforming results to ray trace, with the uncertainties applied. Ideally the traces will intersect at one grid point (Figure 1.3), but this is not usually the case. The grid point with minimum slowness residual is considered the tremor source location. In addition, the bootstrap method and calibration are applied to obtain more reliable locations and estimate the location uncertainties.

The frequency bands 2-8 Hz and 2-6 Hz are used for the analyses of tremor and LFE respectively. The repeating LFEs are difficult to detect due to their inherently low signal-to-noise ratios (*Brown et al.*, 2008; *Shelly et al.*, 2006). This problem can be circumvented once LFE templates are identified. Scanning two months of continuous seismic data, we visually identify the three "clear" LFEs. And we use the modified automatic network-beamforming response method and distinguish hundreds of LFEs. Those LFEs can be categorized into 28 families based on their cross-correlations. We then use those three visually identified

LFEs and one LFE with the highest average cross-correlation coefficient from each family as templates to search for new LFEs with a matched-filter method. For each template, we use a sliding 6 s time window, with a 0.025 s time step to search the whole continuous seismic data. Though it is difficult to distinguish the S- and P-wave arrivals in an LFE at a single station due to low signal-to-noise ratio, they become recognizable on aligned and stacked waveforms. We use both the mini array stations and the USGS-AVO stations to locate the LFE families using phase arrivals and the hypoinverse algorithm (*Klein*, 2002).

3.4 Results

3.4.1 Results of the two-month data

Tectonic tremor (TT)

The beam back-projection method shows significant improvements in tremor detection over visual detection. During the two-month data period, the beam back-projection method detects five times the tremor activity in terms of duration compared to visual detection (visually scan the seismogram) (Figure 3.3). The beam back-projection method detects 1.3 hours of tremor per day on average. In contrast, visual inspection reveals tremor activity of only 0.27 hours per day on average.

The tremor activity lasts from minutes to hours, and TTs show a spatiotemporally heterogeneous distribution in the study region (Figure 3.3, 3.4). The tremor catalog produced using the beam back-projection method shows that the tremors are located to the south of the array in two clusters, with the majority of them distributed offshore to the

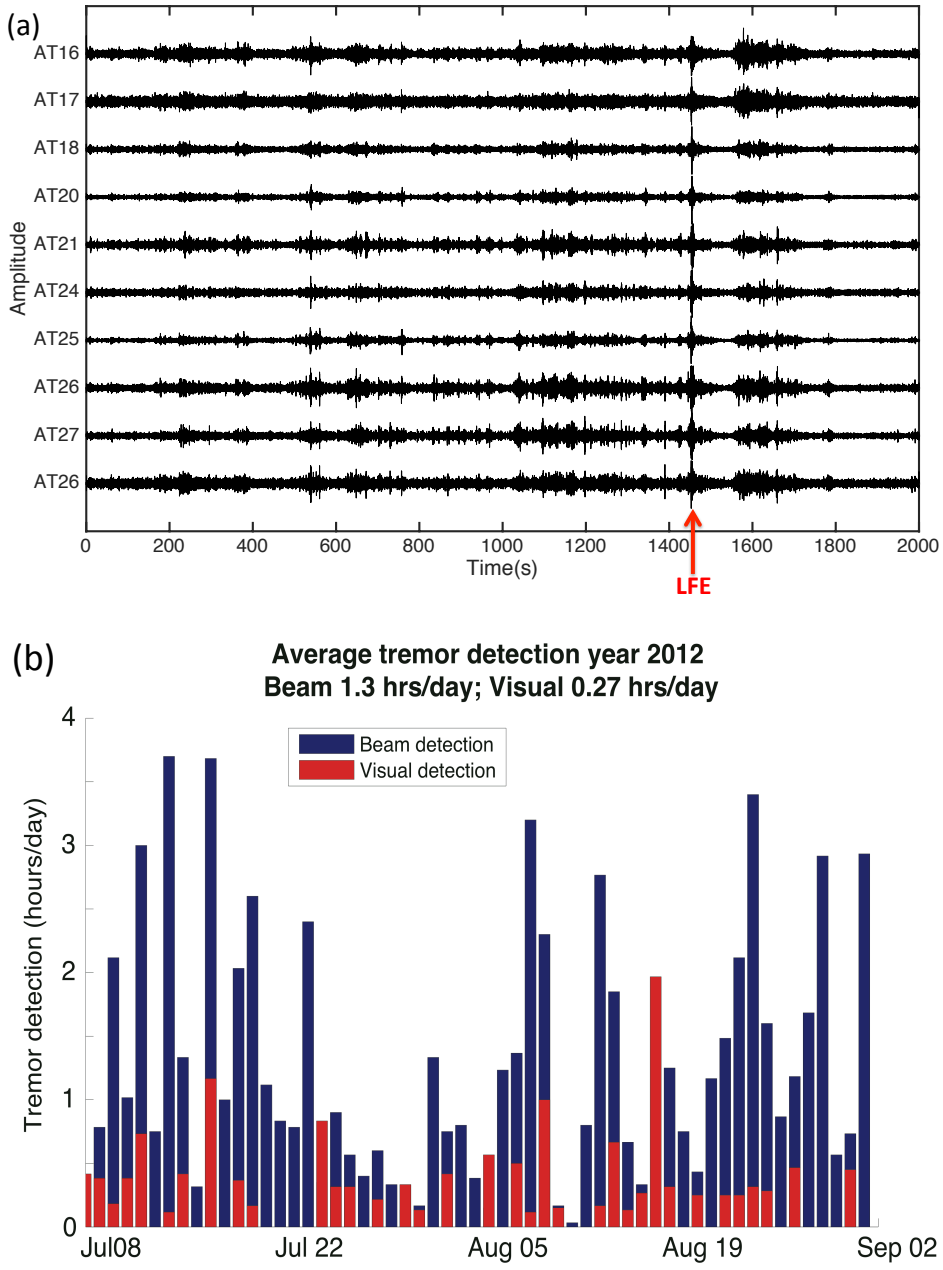

Figure 3.3: (a) Example of 2-8 Hz filtered velocity seismograms for the tremor activity on 23^{th} July 2012, recorded by the pilot array. The red arrow shows one of the visually identified LFE templates. (b) Tremor detection comparison using beam back-projection and visual scanning method. The beam back-projection method detects 5 times higher duration of tremor activity.

south of the Unalaska and Akutan Islands. The tremor activity can be divided into two clusters with a depth range from 45 to 70 km. This range is deeper than the 30-35 km depth range observed in SW Japan and the 30-40 km depth range observed in northern Cascadia and Costa Rica (*Brown et al.*, 2009). Along strike, there is an approximately 25 km gap in between the two tremor clusters. This is much larger than the location uncertainty, with average uncertainy in NS about 3.5 km and EW about 3.8 km, calculated using the bootstrap method. The western cluster aligns along-strike to the south of the Unalaska-Akutan Island and covers a much larger area in map view (Figure 3.1, 3.4). On the other hand, the eastern cluster is much smaller and located to the southeast of the Akutan Island. The western patch also shows a larger depth range and deeper downdip edge than the eastern patch. The location density map shows more detailed spatial distribution, which indicates tremors are not uniformly distributed even in the same cluster (Figure 3.4). The majority of the tremor locations are within 4-5 discrete patches within the western cluster. The most tremor-active patch is observed within the western cluster just offshore Unalaska Island.

Tremors in the western cluster are temporally more active and have a longer duration than those in the eastern cluster (Figure 3.5). Tremors in the eastern cluster are only active for a few times during this two-month period, while the western cluster shows activity almost daily for the entire two months.

In the study region, tremors generally show along-strike migration. In the eastern cluster, tremors propagate to the southwest along the strike at a speed about $13 \sim 15$ km/h (Figure 3.6), with only small amount of along-dip propagation (Figure 3.5, 3.6). In the western patch, it moves in both southwest and northeast directions, with a higher

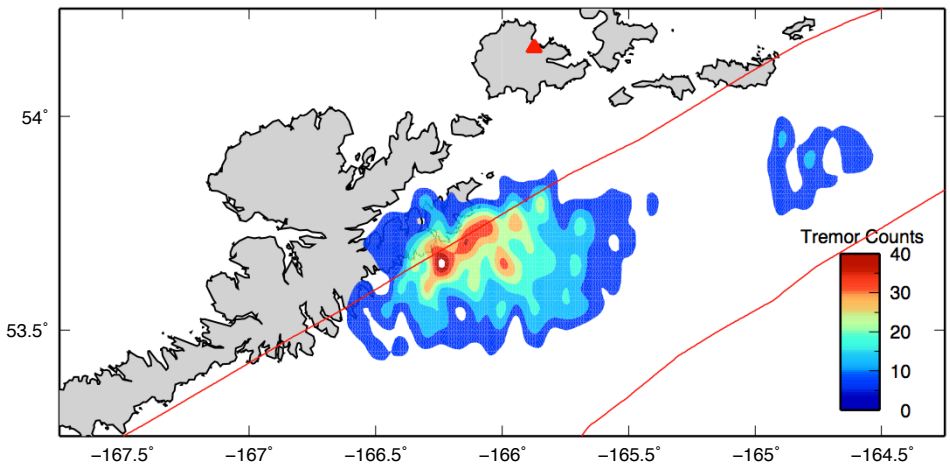

Figure 3.4: Tremor location density during the time period of this study. The red triangle shows the location of the mini array and the red lines delineate the eastern end of rupture zone of the 1957 M_w 8.6 earthquake.

velocity (30 - 110 km/hr) and shows movements along both strike and dip direction (Figure 3.6). Assuming that the TTs are occurring on the subduction interface, tremor clusters are located in a depth range between 45 and 70 km. TTs in the western patch show a larger depth variation than the eastern patch. Interestingly, the downdip edge becomes progressively shallower from west to the east (Figure 3.1). Tremor studies in western Japan suggest that tremor is located downdip of the rupture zones and outline the depth extent of extensive slip during large earthquakes (*Ide et al.*, 2007a). This relationship has also been observed near Kodiak Island, Alaska, where tremor and LFEs occurs near the down-dip extent of the 1964 M_w 9.2 Alaska earthquake (*Brown et al.*, 2013). In our study region, TTs appear to be located down-dip of the rupture zone of the 1957 M_w 8.6 earthquake.

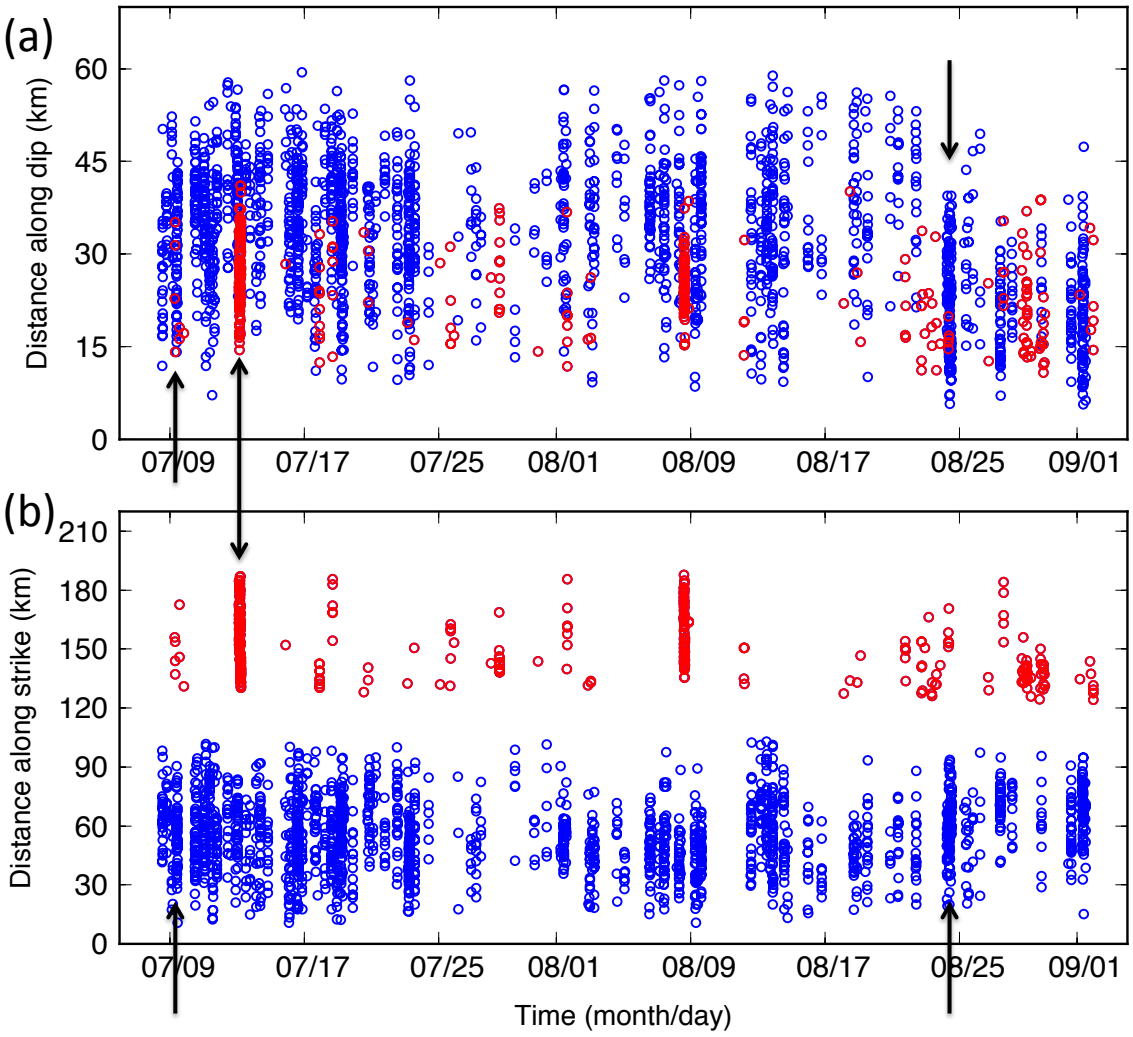

Figure 3.5: (a) Tremor migration along the strike relative to the reference yellow line along strike of the subduction fault in Figure 3.1. Each circle represents the tremor location that determined by the beam back-projection method using a one-minute independent time window. Blue and red colors indicate the tremor locations in western and eastern clusters, respectively. (b) Tremor migration along the dip relative to the yellow reference line along-dip direction in Figure 3.1.

Low frequency earthquakes (LFEs)

The low signal-to-noise ratio (SNR) of LFEs makes it very difficult to detect and analyze an individual LFE event. Swarms of repeating LFEs have been observed within tremor, with each source producing many LFEs over time known as multiplets (*Shelly*

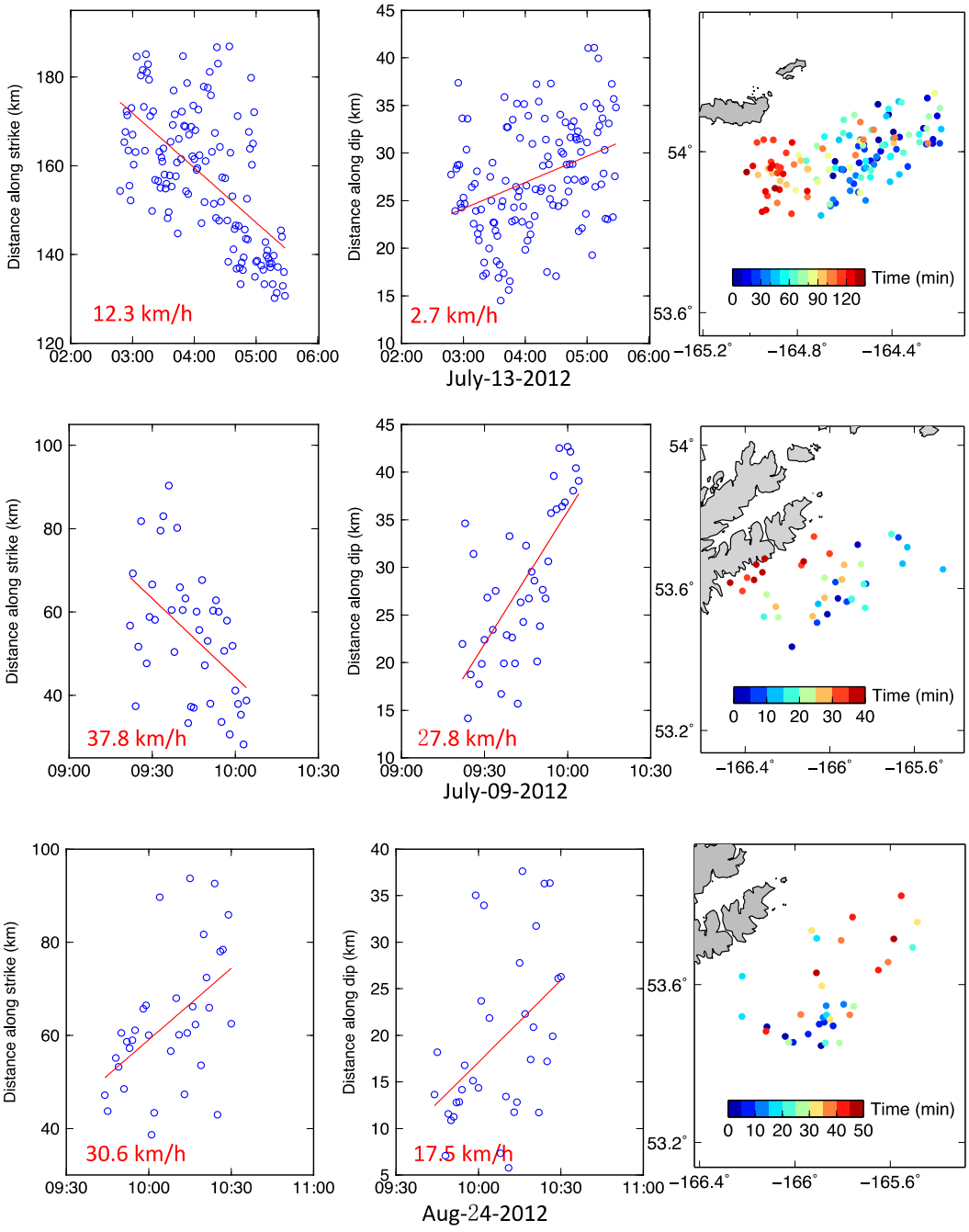

Figure 3.6: Different tremor propagation patterns observed during the two-month data period in the study region. Top panel represents the tremor propagation in the eastern cluster, and the middle and bottom panels show the tremor propagation examples in the western cluster. The red lines represent the average velocity along dip and strike delineated in Figure 3.1. The average velocities for each case are in the bottom-left of each figure.

et al., 2007b). We visually inspect seismic array data and identify three "clean" LFEs, with clear S-phases (Figure 3.7a), and use them as the templates to detect more repeating LFEs (Figure 3.7c). Using the detection threshold as 10 times of the root mean square (RMS) of the two-month results (Figure 3.7b), we detect a total of $\sim$ 1300 LFEs. Similar to the findings in southwestern Japan, Cascadia and Costa Rica (*Brown et al.*, 2009), the majority of the LFEs activities are observed during TTs activities (Figure 3.8), even though they are detected using two very different and independent techniques. However, there are some LFEs (about 15%) occurring in-between tremor activities. Interestingly, during strong tremor activities, we detect much more LFEs showing a short recurrence interval (time between two consecutive LFEs). In contrast, only scattered LFEs are detected with long recurrence interval during times of tremor quiescence. All three LFEs are located using P- and S-arrival times observed in the array stations and stations of the local network (AVO) in Unalaska and Akutan Islands. They show locations within the tremor clusters. Two LFEs are located in the western tremor cluster, and the other one is in the eastern cluster (Figure 3.1). The two western LFEs show activities over the entire two months, while in the eastern cluster, only intermittent LFE activities are detected (Figure 3.9) consistent with the tremor activities.

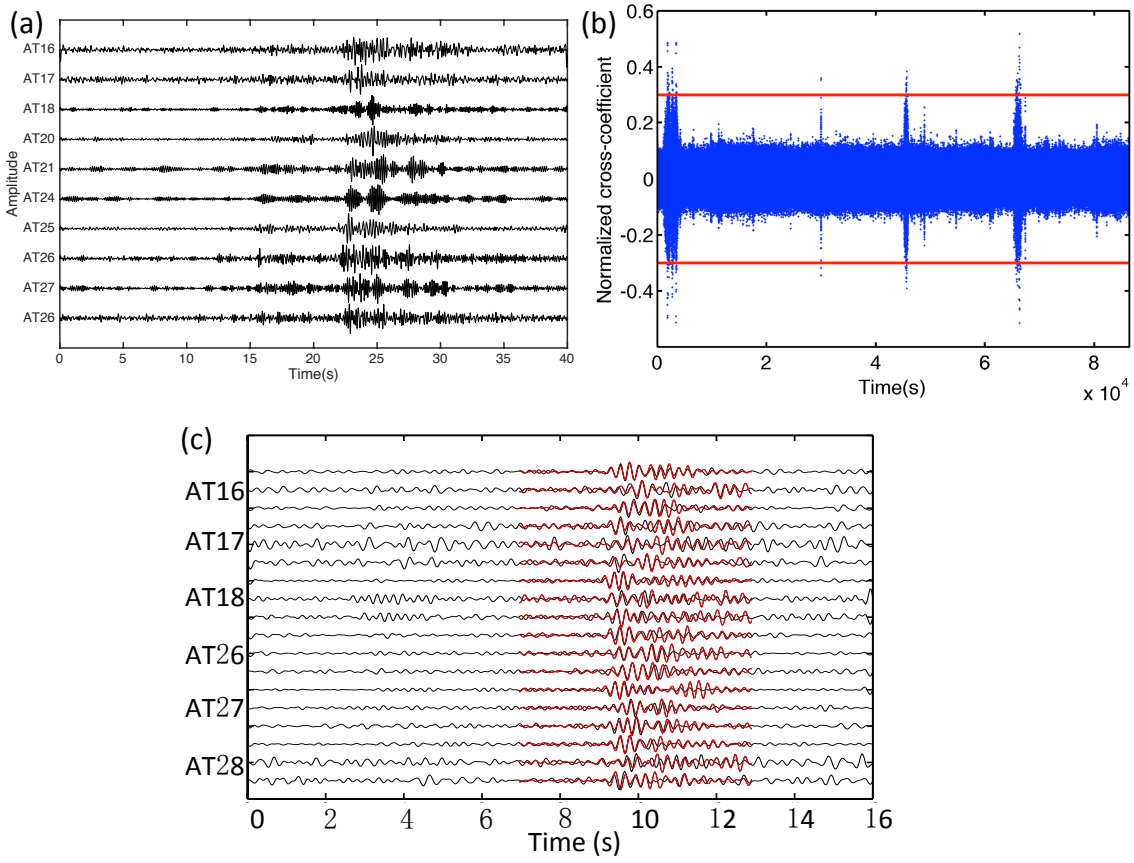

Figure 3.7: (a) Example of 2-6 Hz filtered velocity seismograms of the East channel to determine LFE activity on 23^{th} July 2012. (b) The normalized cross-correlation (CC) sum of 13^{th} July. The red lines show the threshold used to detect LFEs (10 times the RMS, 0.31 in this case). Only 6 stations with 18 components showing high quality seismograms for the whole two-month period are used. (c) Example of waveform matched filter procedure, with the station name on the left side. The seismograms are in the order of E-W, N-S and vertical components. The red seismograms are the templates from (a).

3.4.2 Results of the yearlong data

Tremor Detections

Each mini array shows different detection capabilities. The detection result for each single array is shown in Figure 3.10. The 2A array has the most detection, with average tremor activity duration of 2.64 hours per day. The 3A and PoM detected 0.76

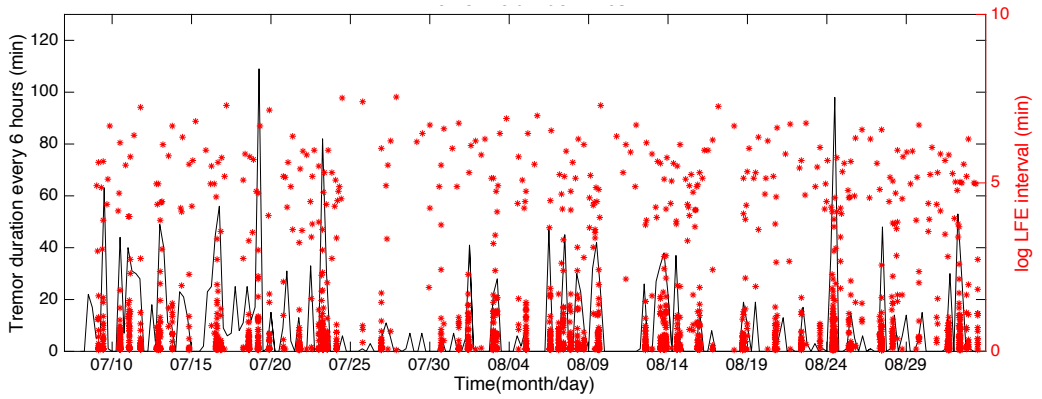

Figure 3.8: TT activity and the overall LFEs time interval (in log scale) between two consecutive LFEs. The black line shows the tremor duration every 6 hours. The red star represents the time interval between two successive LFEs.

and 0.25 hours of tremor signals per day, respectively. Since only the PoM array ran from 2014 to 2015 and there was an approximately six-month data gap (January 2015 to June 2015, the disk filled due to its high sample rate), we focus more on the detection result from July 2015 to July 2016 (Figure 3.11), where during this period all three mini arrays are in operation. It shows near-continuous tremors are detected by three mini arrays using the beamforming method. Tremor is very active in the Unalaska-Aleutian region, which can be up to 10 hours per day and with average activity duration of 2.7 hours per day when combine all three arrays detection. Generally, the deata show episodes of tremor bursts, with relatively quiescent periods in between. In the end of the yearlong period, it has generally shorter duration of tremor signals per day, which may be because fewer stations are active due to a full disk, or a malfunction.

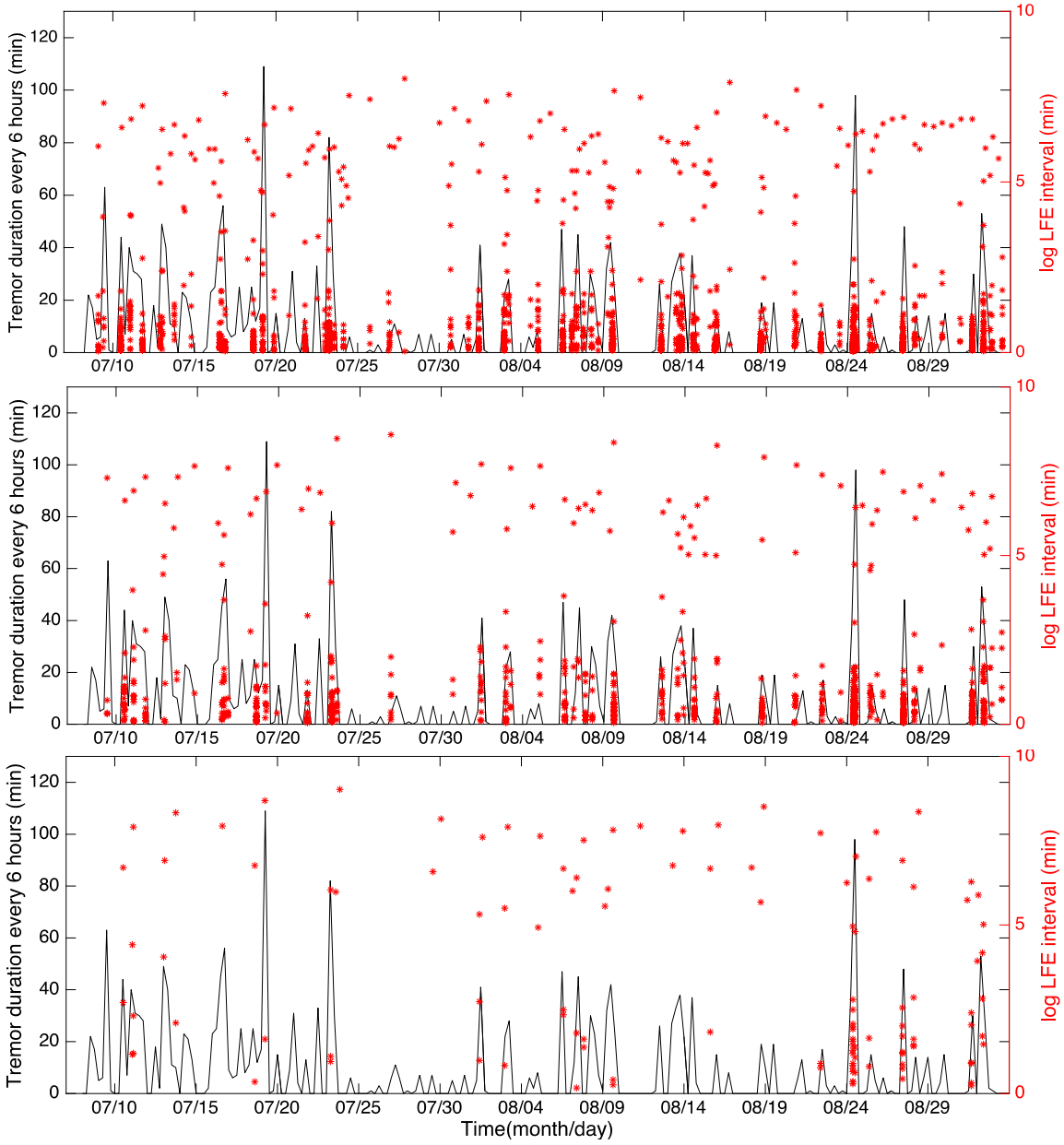

Figure 3.9: TT activity and the LFEs recurrence interval (in nature log scale) for each LFE template. The top and middle panels show the two LFE templates detection in the western tremor cluster; the bottom panel illustrates the LFE template detection in the eastern tremor cluster.

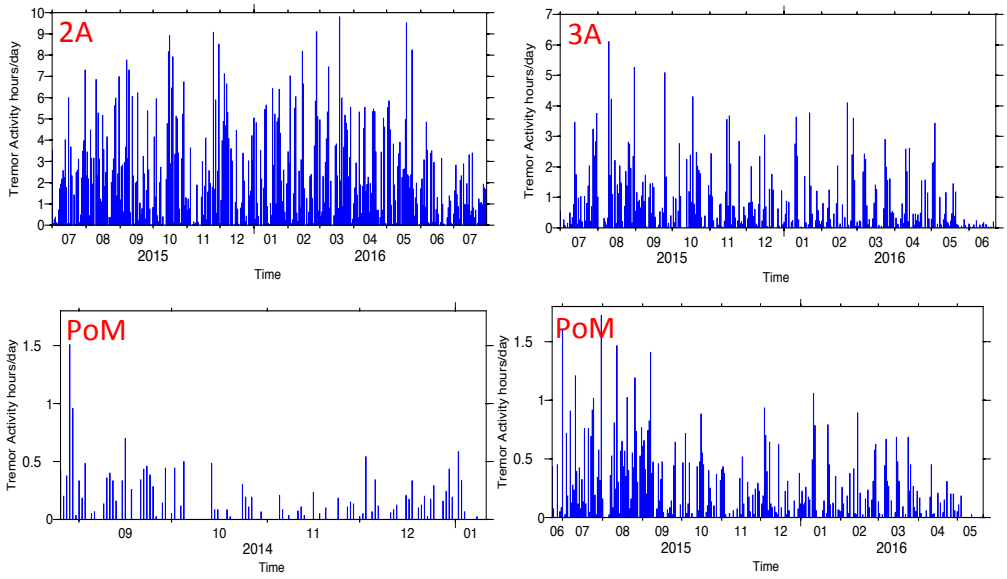

Figure 3.10: Tremor detections by the beam back-projection method by each single array 2A, 3A and PoM arrays. The bottom panels show the results of PoM array in 2014 and 2015-2016, respectively.

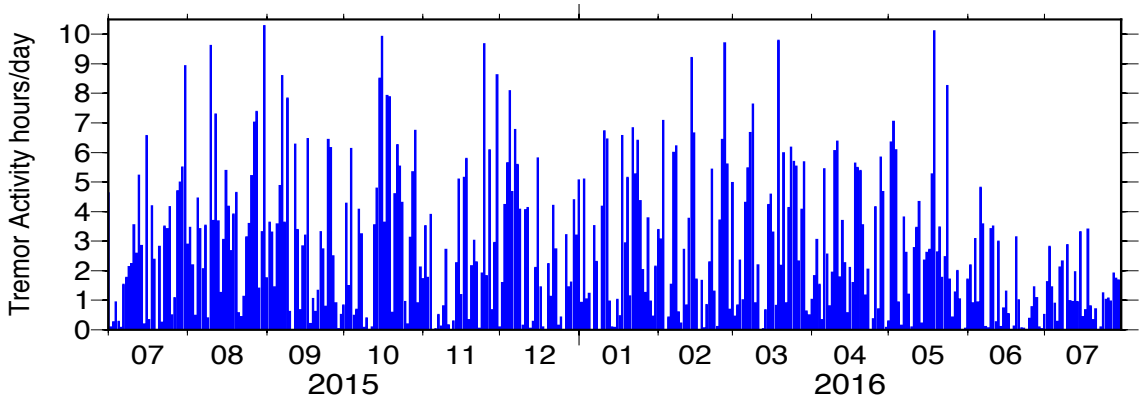

Figure 3.11: Tremor detections by the beam back-projection method using all three arrays.

Tremor locations by each array

The tremor source locations determined by the (multi) beam back-projection method are heterogeneously distributed to the south of Unalaska Island (Figure 3.12). The tremor catalog determined by 2A array shows there are two major clusters. One cluster is

to the southwest of the 2A array and the other one to the southeast. The western patch is much more active than the eastern one, with a 20 km less active segment in between. It can also be seen with a clear azimuth gap in the rose diagram in the top panel of Figure 3.12. The 3A array detects most of the tremors to the southwest of the array center. The tremor source locations can be categorized into three clusters. The western cluster is similar to the western one located by the 2A array, but with shallower depth. The same less active gap is obvious between the western and middle clusters. The middle cluster in 3A array corresponds to the eastern cluster in 2A array detections. A more further eastern tremor cluster shows up in the 3A catalog, which is more or less consistent with the eastern tremor patch in previous two-month detections (Figure 3.1). Each array shows higher detections near the array site and reveals tremor density variations in each cluster. The depths of tremor sources located by 2A and 3A arrays are in a wide range, from 45 to 65 km. In contrast, the PoM array only shows detection of one western tremor patch, with a shallower depth from 30 to 55 km. The apparent shallower depth of the tremors may be due to the uncertainty of the beam back-projection method, in which the slownesss uncertainty results in larger location uncertainty when the source is further away from the array.

Tremor locations by multiple arrays

The locations of tremor sources detected by multiple arrays use the ray tracing method, in which the subduction fault geometry is not required. It produces source locations that are similar in distribution to the locations determined by the single array. Figure 3.13 shows the locations ray traced by the 2A and 3A arrays. Tremors are clustered in

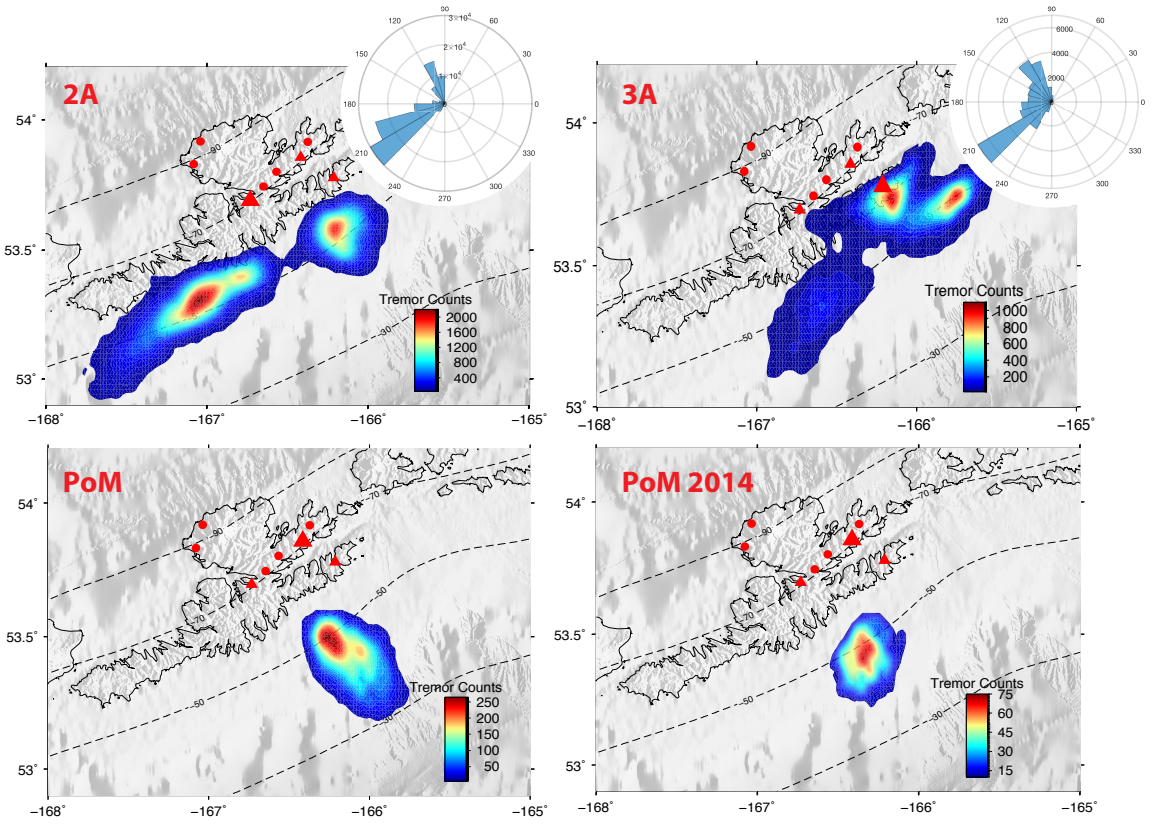

Figure 3.12: Tremor locations determined by beam back-projection method. The rosegram in the top panels show the azimuth distribution of tremor signal locations relative to the array center. The larger size triangle represents the mini array used in each subplot.

three major patches with a less active segment between each other. The cross-sections (Figure 3.13) show that the locations are near or on the plate interface from the USGS slab model. Considering the depth uncertainties both in the slab model and tremor source locations (Figure 3.14), we can say the tremor sources are on the subduction fault, which are consistent with previous studies of other subduction zones (*Ghosh et al.*, 2012; *Rogers and Dragert*, 2003; *Schwartz and Rokosky*, 2007). However, compared to the 30-35 km depth range in SW Japan, the 30-40 km depth range in northern Cascadia and Costa Rica and *sim*40 km depth in Guerrero, Mexico (*Brown et al.*, 2009; *Zigone et al.*, 2015), tremor

sources in our study region show deeper locations, from 40-65 km, with majority of them in the depth range 45-55 km, with uncertainties less than 5 km for $sim84\%$ tremors.

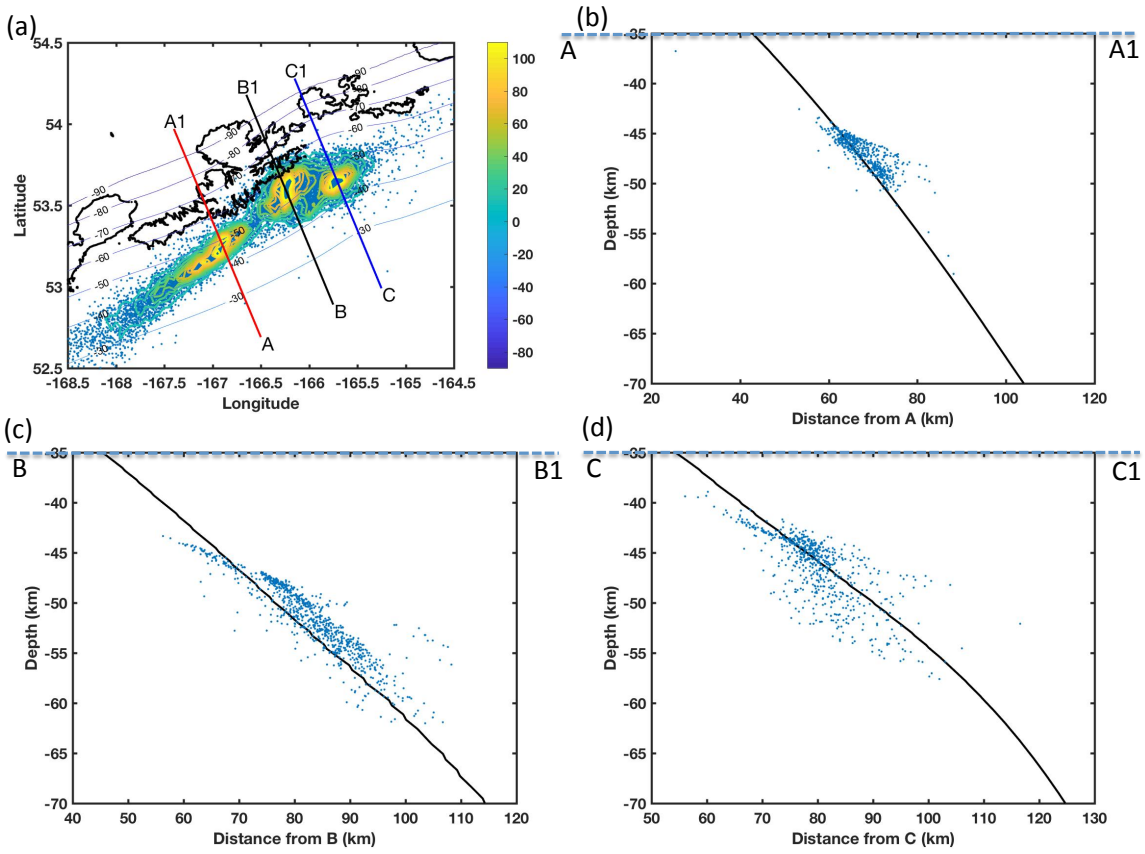

Figure 3.13: (a) Tremor source locations determined by 2A and 3A arrays, with contours mark the source density distribution. Each dot shows a 30s tremor signal locations. (b), (c) and (d) show the cross sections of tremor locations along line A-A1, B-B1and C-C1, respectively. The black solid line represents the subduction interface from the USGS Slab1.0 model.

Tremor sources migration

Tremor migration is an important feature that provides clues about the dynamics of slow earthquakes and the physical asperities on the subduction interface (*Ghosh et al.*,

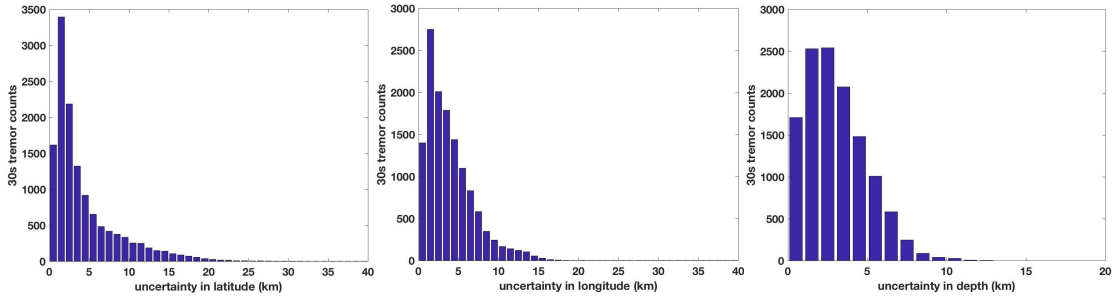

Figure 3.14: Location uncertainties in longitude, latitude and depth, for the tremor sources determined by the ray tracing of 2A and 3A arrays.

2010b,a). During the yearlong data period, we observe multiple migration patterns for the tremor sources. Figure 3.15 shows three types of short time scale tremor migrations, both along-strike and along the dip direction of the subducting fault. Tremor sources can migrate unidirectionally within the asperity and terminate, or reverse direction when they approach the asperity boundary. Tremor in our study region shows a wide range of migration velocities from 15 to 110 km/h. Generally the sources show a faster along-strike migration speed than in the along-dip direction.

Low frequency earthquakes (LFEs)

Using the yearlong data, we identify hundreds of LFEs. Based on their cross-correlation coefficients, we categorized them into 28 LFE families. For each family, we use the one with highest average cross-correlation coefficient with other events in the same family as template and apply the matched-filter detection algorithm. Hundreds to thousands of new LFEs are detected in each family, and show well temporal correlation with the tremor activities (Figure 3.16). Stacking all the events in the same family amplify the seismic signal

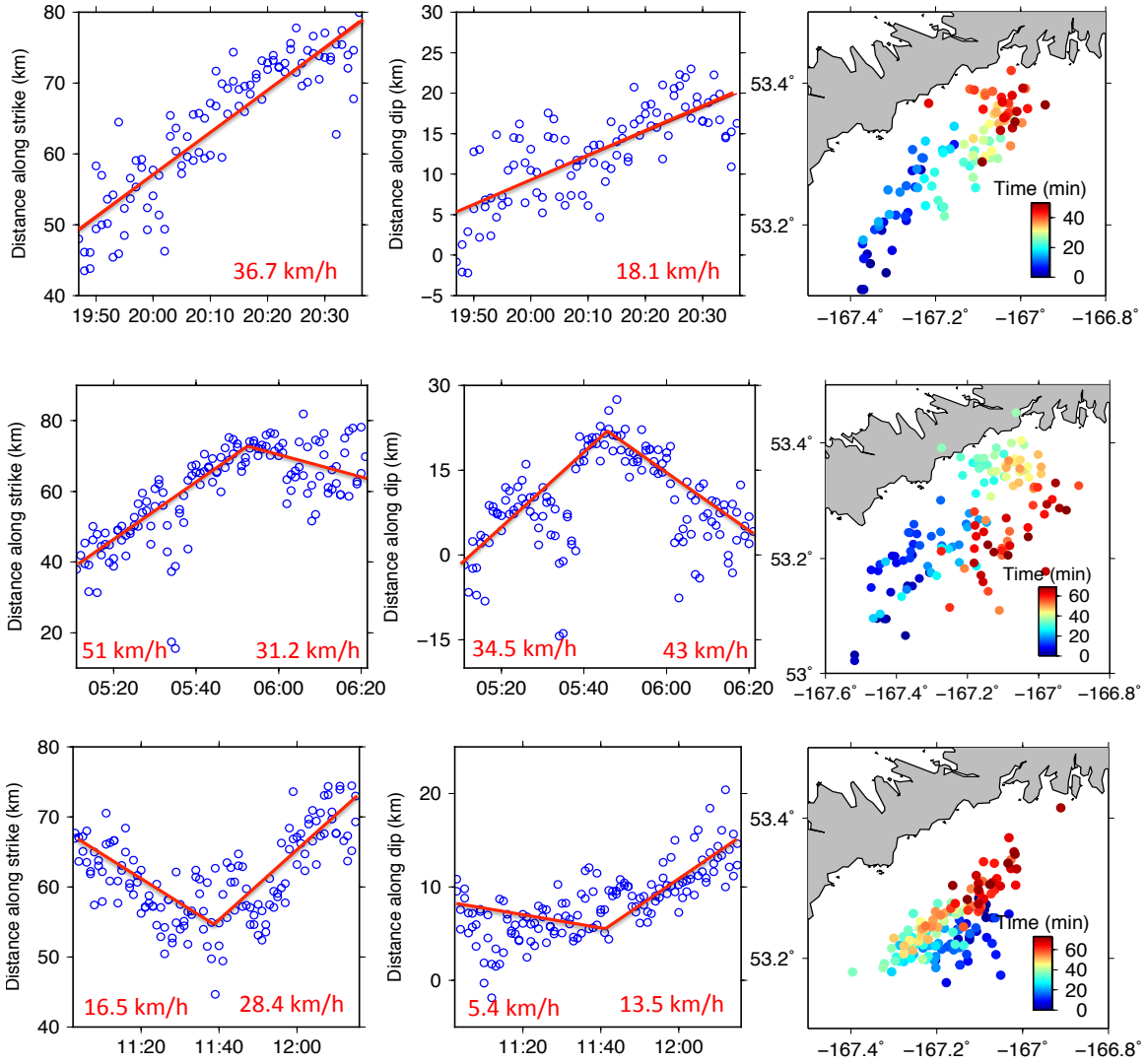

Figure 3.15: Three different migration examples observed in short time scale (tens of minutes to a few hours). The distance along-strike and dip are calculated along the yellow lines in Figure 3.1, with the best-fit red lines showing propagation direction. The velocities in the bottom of each figure show the average velocities. Tremor in the study region shows migration both along strike and dip directions, with a wide range of velocities.

and allow for the picking up P- and S-wave for LFE locations. Figure 3.17 shows all LFE families are within the tremor patches, with more LFE families locating to the west cluster.

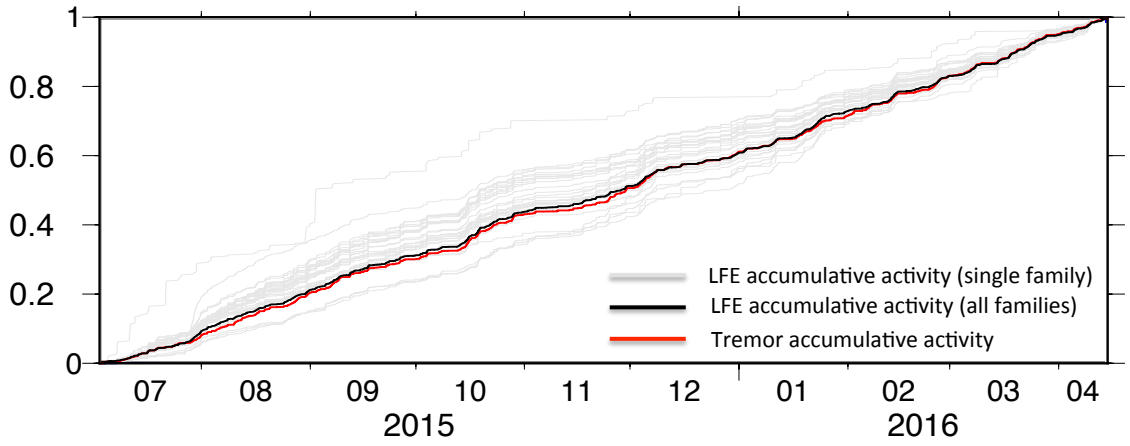

Figure 3.16: Temporal relations between tremor and LFE activities. Each gray line represents the normalized accumulative activity of LFEs in one family. The black line shows the LFE activities for all families. It correlates well with tremor activity, which is shown in red color.

3.4.3 Discussion and Conclusions

The abundant tremor and its spatio-temporal distribution in the Unalaska/Akutan region may indicate frictional properties of the plate-interface changing from stick-slip to creeping in both the dip and lateral directions (*Rubin*, 2011; *Gomberg and Prejean*, 2013). The tremor source locations determined by multiple arrays show the locations are near or on the subduction fault, suggesting the locations back-projected to the subduction geometry is reliable. Each mini array shows different detection capabilities, with higher detections near the array site. This can be due to multiple reasons, such as the distance variation between

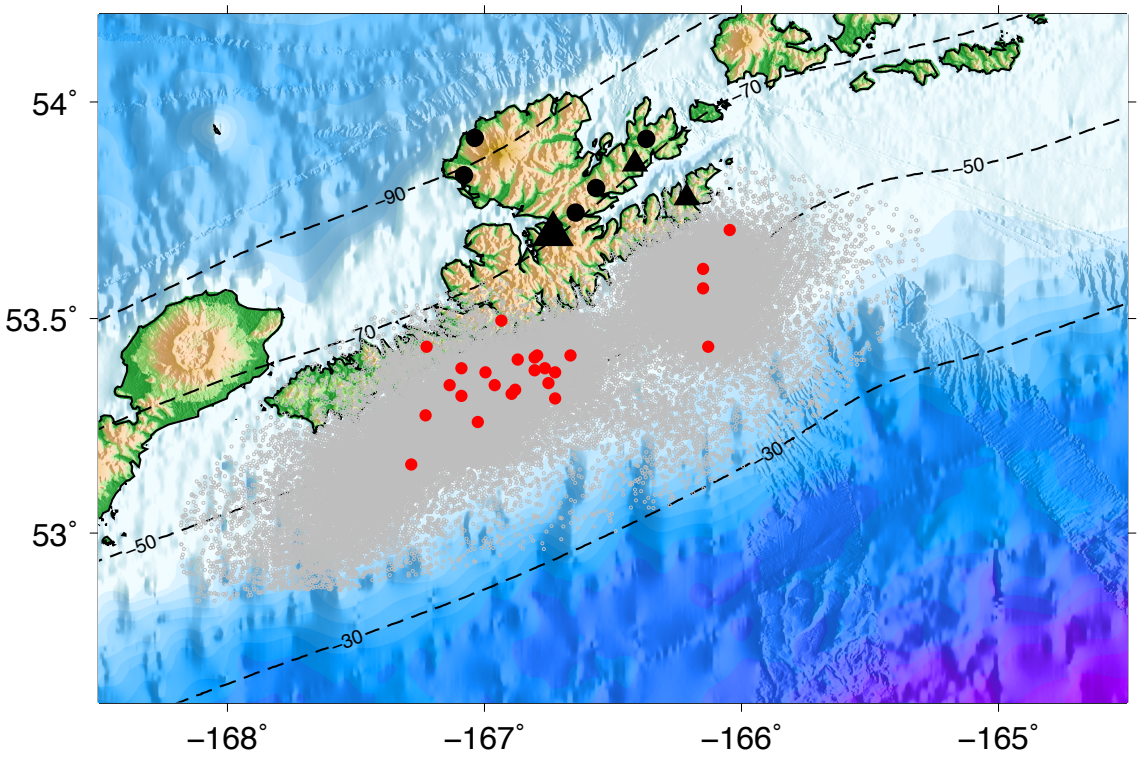

Figure 3.17: Spatial relations between tremor sources and LFEs located by 2A array. Each gray dot represents one tremor source location for a 30s time window. And the red dots show the locations of LFEs detected by the same array.

the tremor source locations and the array location, the noise level in each array site, and the structures along travel traces from sources to each array.

Tremor events are located more deeply in the Unalaska-Akutan region than in most other subduction zones. The two-month data set shows tremor sources are located in a depth range 45 to 70 km, and the better constrained depths determined by multiple arrays show a range of 45-60 km. The tremor sources are deeper than the 30-35 km depth range in SW Japan, the 30-40 km depth range in northern Cascadia and Costa Rica, and 40 km depth in Guerrero, Mexico (*Brown et al.*, 2009; *Zigone et al.*, 2015). This may indicate tremors are fluid driven activities (*Miyazawa and Mori*, 2006; *Rubinstein et al.*, 2008): since

the incoming plate in the study region is older (10-30 Ma older), faster, and colder than other places, the hydrous minerals fluid is generally released at greater depths (*van Keken et al.*, 2011; *Abers et al.*, 2013; *Brown et al.*, 2013). Tremor events are clustered to the south and offshore of the islands. Heterogeneous distribution of tremorgenic area along strike and dip may be due to the temperature variation along the arc that controls the distribution of hydrous minerals releasing fluids (*Katsumata and Kamaya*, 2003) enabling tremor activity.

The two-month data result shows a $\sim$ 25 km gap between the two tremor clusters. Two months are too small of a time period to gauge long-term tremor behavior. The yearlong data set results identify three tremor patches, with a $\sim$ 20 km gap between the western and middle one and a $\sim$ 12 km less active segment between the middle and eastern patches. The middle and eastern cluster of tremor sources located using the yearlong data share the same patch with the western patch and terminate at the tremor gap that was observed in the two-month continuous study. This suggests the gaps are temporally stable features, and indicate lateral heterogeneity in the transition zone. Tremors in the study region distribute roughly in a zone between the slightly coupled and the decoupled area of the plate based on geodetic models (*Cross and Freymueller*, 2008; *Freymueller et al.*, 2008). We posit these gaps represent an aseismic creeping zone releasing stress without much seismic radiation. Using the Advanced National Seismic System (ANSS) earthquake catalog, we compare the tremor distribution with earthquakes near the subduction surface ($\leq$ 5km) for the last 15 years (01/01/2002 to 10/01/2016) (Figure 3.1). Interestingly, earthquakes appear to be occurring along the edge of the tremor clusters, possibly delineating the boundaries of transitional asperities in the study region. In addition, the tremor activities

also show heterogeneous temporal distribution, with relatively silent periods between the tremor bursts. This may imply the occurrence of multiple small slow slip events (*Frank*, 2016), which requires detailed geodetic study to verify.

Migration is one of the most significant features of tremor. Tremors are thought to represent slip on small asperities due to slow slip in the surrounding region (*Bartlow et al.*, 2011). We observed more frequent tremor activity in the western cluster, which may imply a higher slip rate than that in the eastern segment. The geodetic studies also show the plate motion velocity becomes faster from east to west along the Alaska-Aleutian subduction zone (*Brown et al.*, 2013). The migration direction, pattern and speed of tremor sources also shed light on the dynamics of the slow earthquakes and the physical asperities on the subduction interface (*Ghosh et al.*, 2010a,b; *Obara et al.*, 2011). Tremors may be more active at relatively stronger asperities comparing to the surrounding relatively creeping zone. We speculate that the migration terminates or the direction changes at the rheology perturbation. The various migration patterns, with wide ranges of migration speed both along strike and dip direction, observed in the study region suggest non-linear rheology distribution (*Luo and Ampuero*, 2017).

The majority of the LFEs occur within the duration of tremor events, and show a much shorter recurrence interval than the LFEs occurring in the non-tremor period. The LFEs located to the west are more frequently active, which is consistent with the higher tremor activity in the study region. Additionally, all LFEs are located within the tremor patches. This supports the notion that LFEs comprise at least a portion of tremor (*Shelly et al.*, 2007b; *Brown et al.*, 2008). In addition, there are some LFE activities that do

not temporally coincide with tremor activities. This may be explained by the possible incomplete detection of tremors because of the limitation of the station distribution and low SNR. A similar phenomenon has been observed in Guerrero, Mexico, where only 18.3% of LFEs are reported to occur during tectonic tremor for a yearlong period (*Frank and Shapiro*, 2014; *Husker et al.*, 2012). LFEs are considered small seismic events that occur at the fault releasing accumulated tectonic stress (*Ide et al.*, 2007a; *Shelly et al.*, 2007a; *Ohta and Ide*, 2011; *Bostock et al.*, 2012). In addition, we calculated the relative moment of tremor sources by integrating the far-field displacement pulse and then corrected for distance from the source location to the array center. The result shows that more larger moment tremor events occur in the western cluster. Thus more frequent activities of tremors and LFEs in the western region may suggest a higher seismic slip rate than that in the eastern region.

Multiple cases have been observed that local earthquakes in the study region can either terminate the tremor activities or stimulate/amplify the tremor activities (Figure 3.18), depending on the locations of earthquakes. In another way, some local earthquakes occurred after a burst of tremor activities. Due to the limitation of station coverage, we are unable to figure out how the stress change in the tremor patches affect or or are affected by the regular earthquakes. At the minimum, our data indicate that earthquakes and tremors can interact with each other. Our study region is located at the eastern and down-dip edge of the rupture zone of the 1957 M_w 8.6 earthquake and to the west of the 1938 M_w 8.2 megathrust earthquakes, and this area has not ruptured for a long time (*Brown et al.*,

2013). The prolific tremor activities may transfer the stress to the updip seismogenic zone, leading to a clock advance of the next large earthquake.

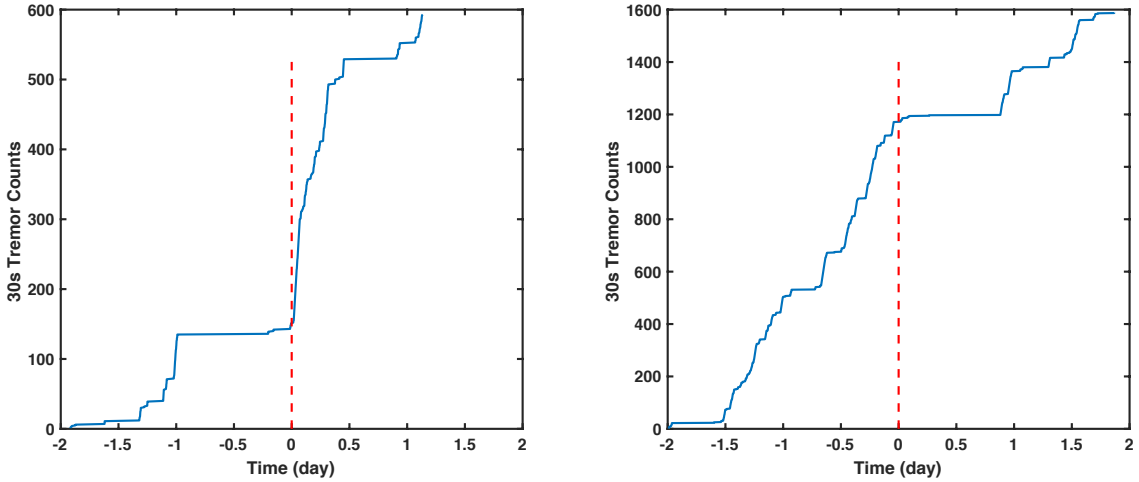

Figure 3.18: Temporal relationship between the earthquakes and tremors in the study region. The red line marks the start time of the earthquakes. Left panel shows tremor bursts after the earthquake and right panel shows tremor activities terminate after the earthquake.

In conclusion, beam back-projection shows a high capability of tremor detection and spatial resolution in the Unalaska-Akutan subduction zone. The near-continuous tremor activity is clustered in several patches, with tremor gaps or less active segments in between, indicating lateral heterogeneity in the transition zone. Regular earthquakes are located along the edges of the tremor patches, possibly delineating the boundaries of the tremorgenic transition zone. The LFEs spatiotemporally match with the tremor activities, showing a much smaller time interval between events during tremor signals. The more frequent tremors and LFEs activities in the western region suggest a higher slip rate than the eastern region. The various migration patterns show non-linear rheology and heterogeneous physical asperities distribution in the transition zone of the study region.

Chapter 4

Using the Move Max Matched-filter to Detect Small Earthquakes in the San Jacinto Fault Region Triggered by the 2014 M_w 7.2 Papanoa Earthquake

4.1 Abstract

We apply the move max matched-filter (MMMF) method to detect the heightened seismicity triggered in the San Jacinto fault zone, Southern California, by the 2014 M_w 7.2 Papanoa earthquake. This method detects 5.4 times the number of earthquakes than is

recorded in the ANSS and SCSN catalog, while the conventional matched-filter method only distinguishes 3.2 times the number compared to the catalog events using the same detection threshold. The seismicity rate increases significantly $\sim$ 3.5 hours after the passage of the surface waves of the Papanoa earthquake, and the heightened seismic rate persists for about one week. More than one mechanism may be responsible for this observation. The transient dynamic stresses may have triggered a slow slip or fault creep, and consequently led to the increased and protracted seismicity along the San Jacinto Fault (SJF). The highest increase of seismicity is located west of the SJF and the city of Anza, implying the activation of an unmapped blind fault. A best-fit plane and focal mechanism infer a normal fault to be nearly perpendicular to the SJF, steeply dipping to the northwest. We argue that a time-dependent acceleration to failure process initiated by the dynamic stress change can result in the enhanced seismicity on the newly discovered fault. The unmapped fault may also indicate more serious damage in the surrounding areas if a large earthquake nucleated near or within the Anza seismic gap.

4.2 Introduction

With the implementation of globally distributed seismic networks and improved earthquake detection/location methods, large earthquakes have been widely observed to change the seismic rate, via immediate or delayed triggering of earthquakes, of regions hundreds to thousands of kilometers away (*Hill et al.*, 1993; *Shelly et al.*, 2011; *Meng and Peng*, 2014; *Mendoza et al.*, 2016). The dynamic stress changes due to large earthquakes at teleseismic distances have been estimated to be between ~ 0.1 and $\leq$ 1MPa (*Prejean and Hill*,

2009); thus, the occurrence of triggered earthquakes indicates a region is sensitive to small stress perturbations. Studies of such triggered earthquakes provide clues to understanding the stress state on a fault prior to failure (*Johnson et al.*, 2015).

The San Jacinto Fault Zone (SJFZ) is currently the most seismically active fault segment in southern California (*Thatcher et al.*, 1975; *Kagan et al.*, 2006). It consists of several right-lateral strike-slip faults, and has produced 11 earthquakes with magnitudes larger than 6 in the last 120 years (*Bailey et al.*, 2010; *Kagan et al.*, 2006). The central region of the SJFZ, a segment known as the Anza seismic gap, is known to not have spawned a major earthquake for over 200 years (*Rockwell et al.*, 1990). Previous studies show the potential for an earthquake with magnitude 6.5 or larger to occur in this seismically quiet segment (*Thatcher et al.*, 1975; *Sanders and Kanamori*, 1984). Therefore, understanding the stress state and conditions required for rupture nucleation in the Anza gap and nearby faults is important to estimate earthquake hazard there.

On 18 April 2014, the M_w 7.2 Papanoa, Mexico earthquake occurred within the Guerrero seismic gap, as a result of thrust motion at shallow depth along the Cocos-North America plate boundary (*Mendoza and Martínez López*, 2017). The event result in unprecedented damage near the epicenter and minor damage in Mexico City. In this study, we build upon the commonly used template matched-filter method, and apply the move max matched-filter (MMMF) method to detect the seismic events in the study region, one month before and after the Papanoa earthquake. Then we use hypoinverse (*Klein*, 2002) and hypoDD (*Waldhauser*, 2001) to locate and relocate all detected events with high pre-

cision. Finally, we investigate the spatiotemporal distribution of relocated earthquakes and discuss the possible mechanisms for this observed triggered seismicity.

4.3 Data processing and methods

In this study, we use continuous seismic data from 17 stations surrounding the San Jacinto fault (Figure 4.1) to detect and locate local earthquakes in the study region that were triggered by the M_w 7.2 Papanoa earthquake. The data spans one month before to one month after the Papanoa event. During this period, there are 880 local events recorded by the Advanced National Seismic System (ANSS) and the Southern California Seismic Network (SCSN) catalog (Figure 4.1). All of the catalog events are used as templates to perform the matched-filter and MMMF methods in detecting missing local events. For each catalog event (origin) time, a 25 s time window (resampled at 20 samples per second) around the waveform is cut, and then applied to do sliding window search through the 2 to 7 Hz filtered continuous dataset to detect other similar waveforms.

We first use the traditional template matched-filter method. It calculates the cross-correlation coefficient between the template and the continuous waveforms for all the 3 components, sums the coefficients, and retains new detected events that meet or exceed some predetermined threshold value. One assumption behind this method is that the matched event shares the same (or similar) location as that of the catalog event. As a result, the template and its matched event(s) have similar waveforms and station move-out. We have experimented with several thresholds by visually checking detected events through visually inspecting the seismograms of some random selected detection. A threshold value

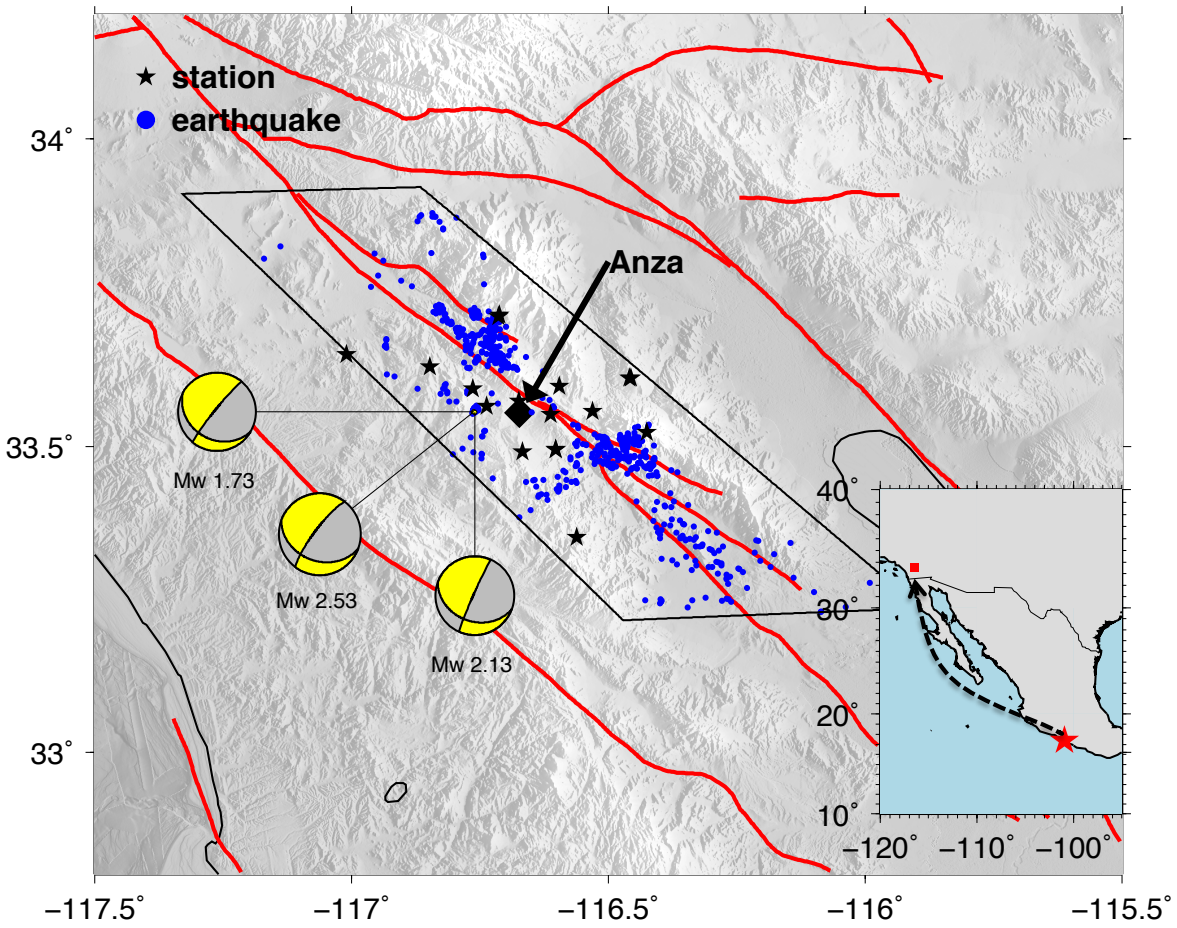

Figure 4.1: Study region in southern California. The black polygon outlines the study region. The red lines show the traces of active faults. Each blue dot represents one event in the Advanced National Seismic System (ANSS) and the Southern California Seismic Network (SCSN) catalog and the black stars represent seismic stations used in this study. The red star in the inset map shows the location of the 2014 M_w 7.2 Papanoa, Mexico earthquake, while the red square marks the study area presented here.Three beach balls show the normal fault focal mechanism in the off fault earthquake cluster discussed below. The black dashed arrow shows the great circle travel path from the source to the study region

of 6 times of the root mean square (RMS) of the two-month cross-correlation results is used in this study to detect new events.

One significant drawback we noticed using the traditional matched filter method, though, is that any given template usually does not produce the maximum cross-coefficients at the exact same move-out time in all stations for the missing events. Furthermore, at the same time window, some stations show peak coefficients while others show much smaller or even negative coefficients, with peak coefficients a few time steps (0.05-1s in our case) away, which lowers the summed coefficients under the threshold (Figure 4.2a). This is because that even some events are located close to the catalog events, but they are not exactly in the same location, which will result in different arrival time lags relative to the template event. *Zhang and Wen* (2015) developed the match and locate (M and L) method to improve their own detections by adding some potential hypocentral locations/grids around the template location. Then they calculate the move-out at each potential location, do the time shift and stack the cross correlation coefficients. This method can detect small events in the grid around the template location, but may still miss the events around the template location but not exactly in the grid locations. In addition, the travel time calculated using the current velocity model may not match the true travel time, and result in artificial move-out. Furthermore, it is not time efficient to calculate the move-out for all the grids to the stations. Considering these limitations, here we use a detection method we call move-max matched-filter (MMMF). In this method, the first step is similar to the matched-filter method, which calculates the cross-coefficient for each component. But in the second step, instead of summing the cross-coefficients directly with constant move-out for

each template, we dynamically replace the coefficient at the time step with the maximum coefficient 1s before and after it (Figure 4.2b,c). In other words, we consider the locations up to 1s travel distance away from the template location as neighboring events. Afterwards we sum the move max coefficients and remove the mean values to make it comparable with the matched-filter results (Figure 4.2d). We then use the same threshold as the matched-filter method to obtain earthquake detections. A similar method has been applied previously by (*Shelly et al.*, 2007b) to detect "weak" LFEs.

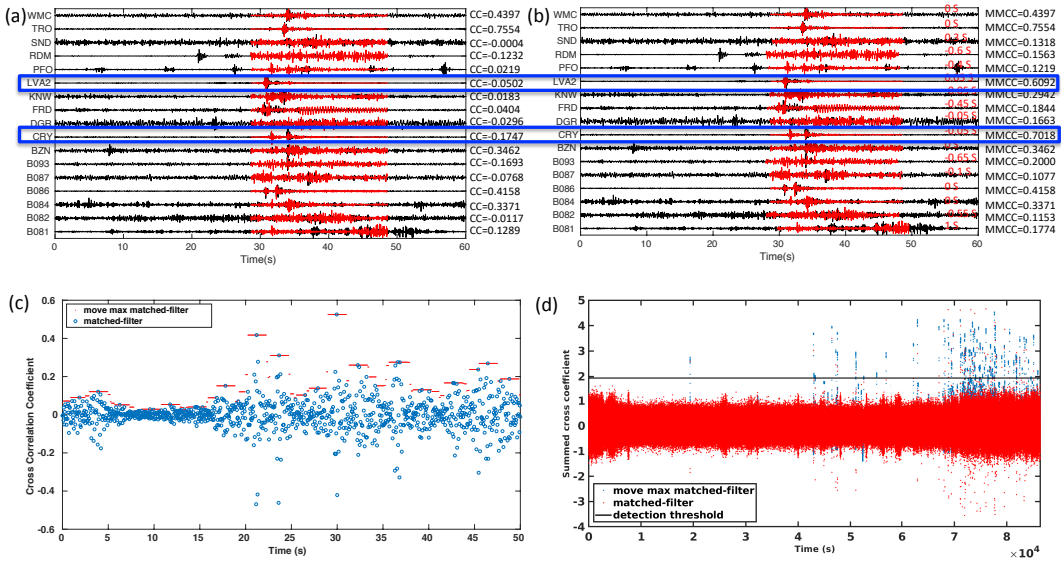

Figure 4.2: Comparison between conventional matched-filter and MMMF. (a) Example of matched-filter method. The cross correlation coefficients that result in the maximum summed coefficient are marked on the right side. (b) Example of the move max matched-filter method. The move max cross correlation coefficients that result in the maximum summed coefficient are noted in black on the right side of the figure, and the time-shift relative to the matched-filter time is shown in red font. Note that cross correlation coefficients are almost always higher for MMMF method. The blue boxes show an example of two stations with a significant increase in cross correlation coefficients. (c) 50s example of MMMF for one component. The blue and red dots represent the cross-correlation used in template matching and MMMF method, respectively. (d) Detection comparison between matched-filter and MMMF. The black horizontal line indicates the detection threshold, which is six times the RMS of two-month cross-correlation results.

After the detections, we use the cross-correlation between the template and the detections for each station to determine the arrival time of P waves using the vertical components, and the S waves with the horizontal components. Lastly we use a 1-D velocity model from *Scott et al.* (1994) to locate all detected phases by first using hypoinverse (*Klein*, 2002), then relatively relocate them using hypoDD (*Waldhauser*, 2001).

4.4 Results

Local earthquakes in San Jacinto fault region triggered by the M_w 7.2 Papanoa earthquake can be seen in Figure 4.3. This figure shows a remarkable increase in seismic activity after the Papanoa earthquake, especially about just a few hours after the passage of the teleseismic wave train. This heightened seismic activity is also clear in histogram and corresponding spectrogram (Figure 4.3). Using the 880 catalog events as templates, the matched-filter and MMMF detect 2835 and 4765 local earthquakes, which are about 3.2 and 5.4 times the numbers of catalog events, respectively (Figure 4.4). The result shows the elevated seismic rate lasts for around 7 days before returning to the background level. To better compare the detection results between each other and with the catalog events, we normalize the cumulative detections to the same level (Figure 4.4). All three lines show similar cumulative patterns, yet differ in detail. The result shows that in the catalog recordings, there is approximately a 50 percent increase of events occurring one month after the Papanoa earthquake, while matched-filter detection results show $\sim$ 87% percent increase of detected events occurring after the Papanoa earthquakes during the same period. The detection results of MMMF detect the most events and also sim50%

increase as the catalog events, amplifying the detection nearly same level both before and after the Papanoa earthquake. But it shows much higher seismicity rate increase in the first three days following the mainshock (Figure 4.4).

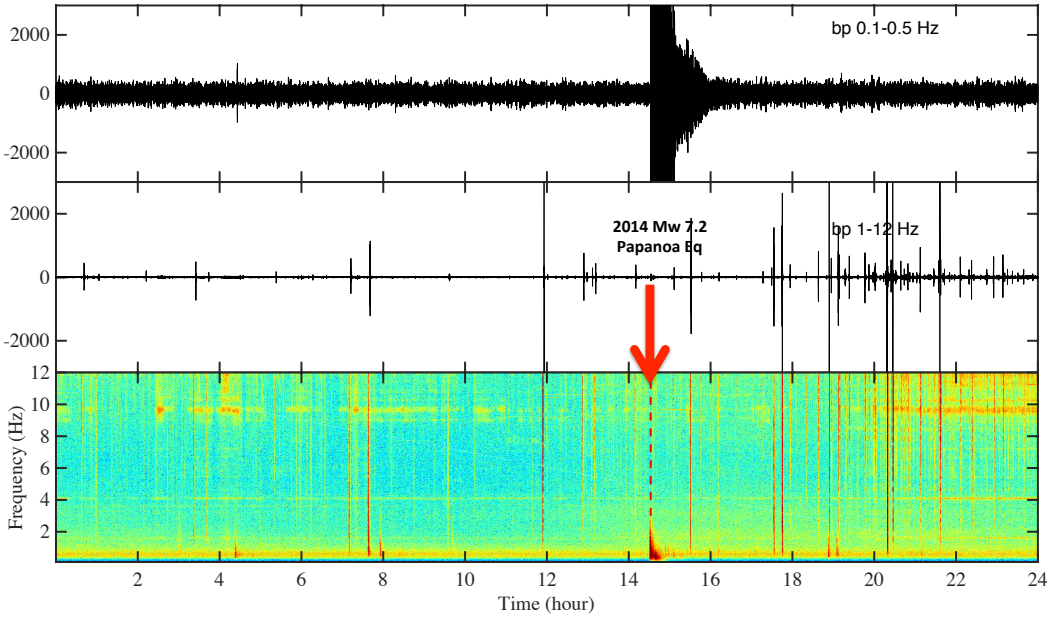

Figure 4.3: Seismograms (top: filtered in 0.1-0.5 Hz to show the teleseismic signal ,and middle: filtered in 1-12Hz to show local seismic signals), and bottom: spectrogram (0.1-12Hz) showing local earthquakes triggered by the M_w 7.2 Papanoa earthquake. The red dashed line marks the occurrence time of the teleseismic event.

After relocation, the newly detected local events show an overall similar distribution to that of the catalog events, but with some significant difference in detail. The new catalog reveals some linear features along the fault traces (Figure 4.5) and a more clear less active area between the northwest and southeast earthquake clusters. This less active seismic region is defined as the Anza gap in previous studies (*Thatcher et al.*, 1975; *Sanders and Kanamori*, 1984; *Rockwell et al.*, 1990). The Anza gap lies in close proximity to the seismically active triple junction of the Coyote Creek, Clark, and Buck Ridge segments of

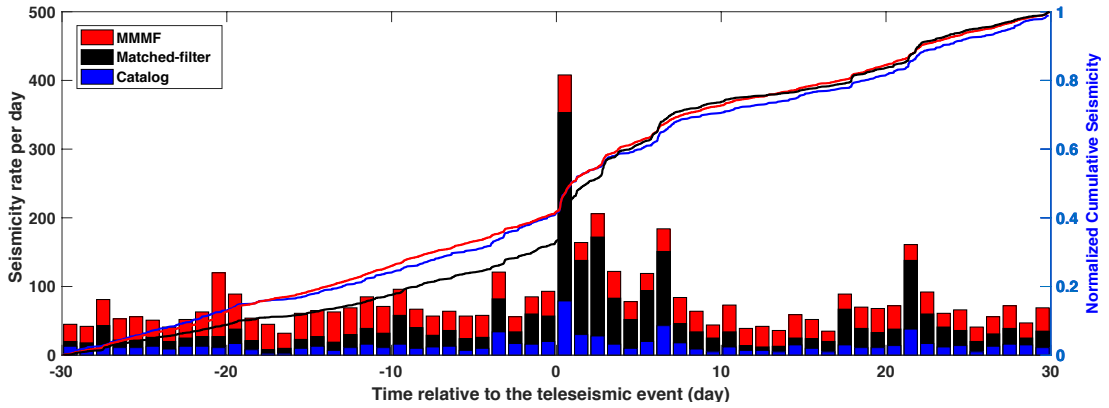

Figure 4.4: Detection results of local seismicity. The histogram shows detection results of daily seismicity. The lines show the normalized cumulative seismicity correspondingly.

the San Jacinto Fault (SJF) zone. The cross section along the SJF trace shows that the earthquake depth distribution is shallow when approaching the Anza gap from northwest, but then increase in depth when moving away from it towards the southeast (Figure 4.6).

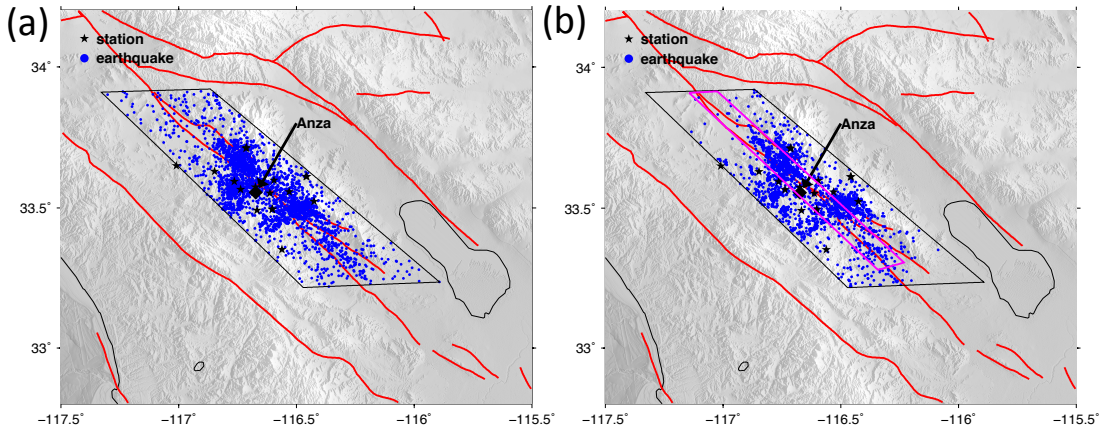

Figure 4.5: Distribution of detected events. (a) Earthquake locations determined with hypoinverse. (b) Relocated earthquake locations using hypoDD. The magenta polygon encompasses the relocated earthquakes the along fault region used to show the cross-section in Figure 4.6.

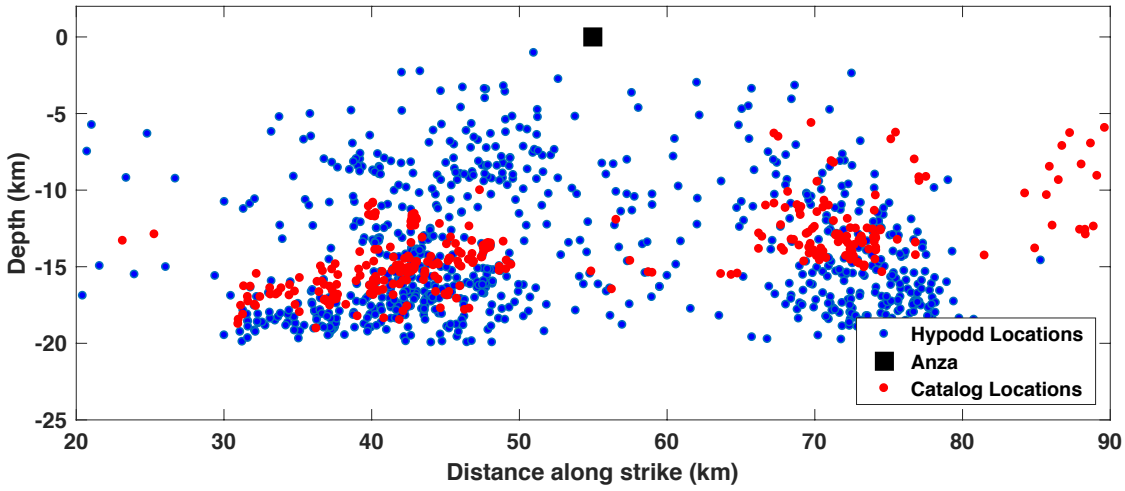

Figure 4.6: Cross section of the relocated earthquakes along the San Jacinto Fault trace from northwest to southeast. Each blue dot represents one relocated earthquake in the magenta polygon in Figure 4.6, and the red dots show the catalog events. The black square shows the horizontal location of the city of Anza.

To investigate the seismicity rate changes in detail, we divide the study region into 0.025 by 0.025 degrees grids and compare their seismic activities one month before and after the M_w 7.2 Papanoa earthquake. Figure 4.7 shows a general seismicity rate increase after the Papanoa earthquake in the study region. Interestingly, new patches light up with seismicity to the northwest and southeast of the Anza gap, but no heightened seismicity is observed within the Anza gap. The patch with the highest seismic rate increase is located west of the city of Anza and off of the SJF. However, there are no known faults that have been mapped in this particular area. Furthermore, we obtain a best-fit plane based on the earthquake distribution. It suggests a fault plane that has a strike nearly perpendicular to the SJF, and is steeply dipping to the northwest (Figure 4.8).

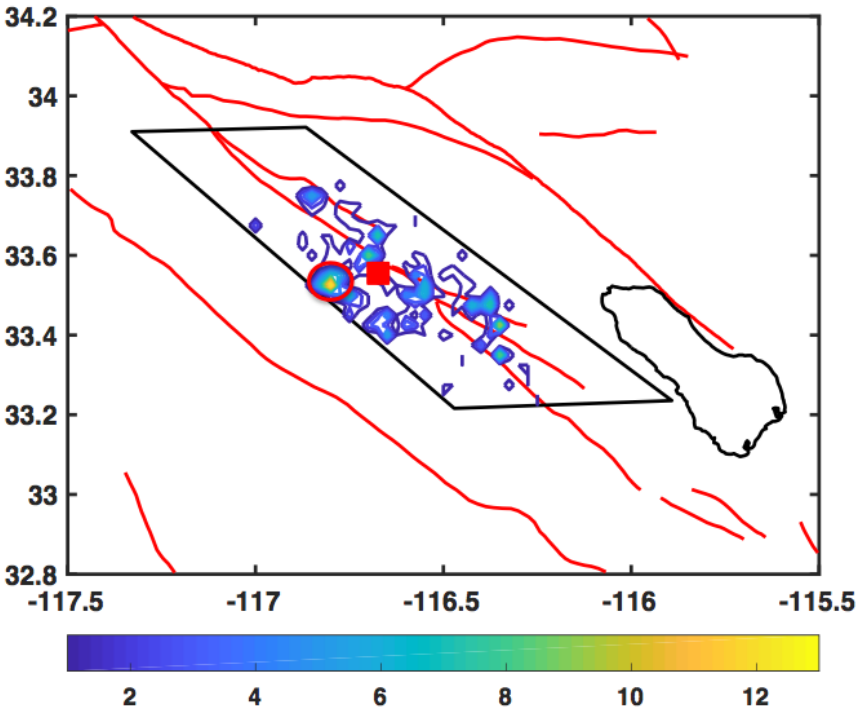

Figure 4.7: Seismicity rate ratio (after/before the M_w 7.2 Papanoa earthquake). Since the cutoff here is selected to be 1, the colored region represents the area of seismicity rate increase. The red ellipse shows the most seismically active region that was triggered by the Papanoa earthquake. The red square marks the location of city Anza

4.5 Discussion

Using 880 catalog events as templates, the matched-filter method detects 2835 events and the MMMF detects 4765 events, which is ~ 1.7 times that of the matched-filter detections. This result indicates that the MMMF method has a much higher detection capability compared to traditional template matching. For each template event, the MMMF method can detect events within a certain distance range (detectable distance) away from the template event, which depends on the allowed shift time (1s in our case), the velocity model, and hypocentral distances. The MMMF method is more time efficient than traditional template matching method, especially for a large catalog. It does not require all

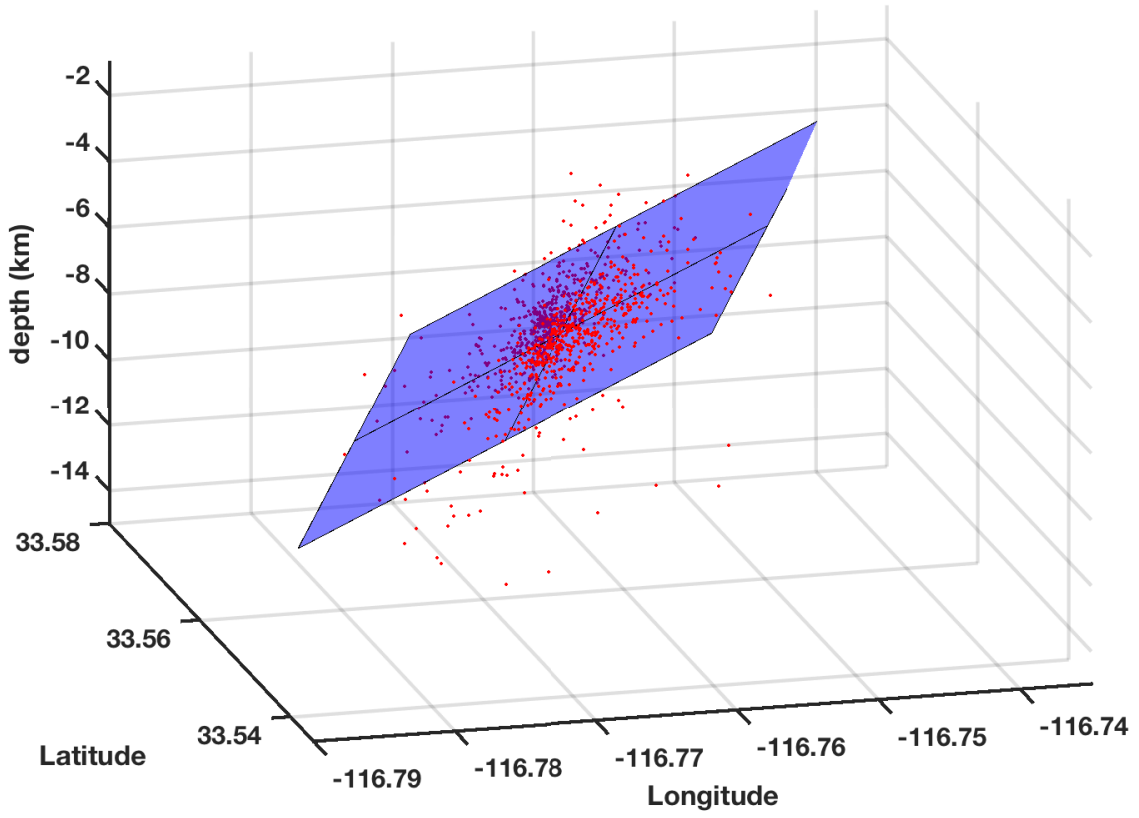

Figure 4.8: Best fitting fault plane for the triggering earthquakes cluster in the Magenta polygon in Figure 4.5. Each red dot represents one relocated earthquake.

catalog events to be used as templates to perform template matching. The study region can be divided into many grids based on earthquake distribution for further analyses. Only a few events, depending on the complexity of local structures and similarity of the waveforms, are able to capture almost all the events in the same grid region because of the allowed move max cross-correlation coefficients.

The seismic rate changes non-uniformly in the study region, with the most significant patch of seismicity about 15 km west of the SJF and near the city of Anza. Figure 4.8 shows the 3-D distribution of the relocated earthquakes in this small region. Earthquakes locate between a depth range of 4 to 9 km, and the locations become shallower from

southeast to northwest. A planar structure that best fits the locations show a strike nearly perpendicular to the SJF and dips steeply to the northwest. The focal mechanisms of three catalog earthquakes (M_w 2.53, 1.73 and 2.13) within this patch indicate a normal fault with strike about perpendicular to the SJF and steep dip (Table 4.1), which could be the result of the extension force from the right lateral San Jacinto and Elsinore fault. We investigate the seismic events in this small area recorded in the SCSN catalog from 01/01/2001 to 12/30/2017, and notice only a few scattered earthquakes in the catalog that occurred before the Papanoa earthquake, implying that this fault has been in quiescence. This may be because of the low tectonic shear stress loading on it, since it is nearly perpendicular to the overall San Andreas Fault plate motion. This unmapped fault does not seem to extend far enough to connect the SJFZ and the Elsinore Fault Zone, thus limiting the likelihood of through-going rupture from one fault zone to the other, which could increase the potential for a large earthquake in this region. However, this new fault is close to the Anza gap, where previous studies show the potential for a M_w 6.5 or larger earthquake (*Thatcher et al.*, 1975; *Sanders and Kanamori*, 1984). A large local earthquake potentially could lead to rupture on this unmapped fault and result in more serious damage in the surrounding region. Another possibility is that an earthquake on the unmapped fault could potentially propagate to become a damaging earthquake on the San Jacinto Fault.

M_w	strike	dip	rake
2.53	217	79	-123
1.73	219	85	-120
2.13	204	87	-125
best-fit plane	215	83	

Table 4.1: Orientation of three relatively large events within the small patch and the best-fit plane for the events in the same patch.

In this study, we do not observe dynamically triggered earthquakes during the passage of the seismic wave train of the 2014 Papanoa earthquake; however, $\sim$ 3.5 hours after the coda we observe a burst of local earthquakes. The elevated seismic rate lasts for about one week before it decays back down to the background level. This observation suggests that dynamic stresses due to the passage of teleseismic waves set off a time-dependent acceleration to failure process, or a secondary mechanism that resulted in delayed triggering (*Freed*, 2005). The rate and state friction law derived by *Dieterich* (1979, 1981), which has logarithmic dependence of friction on rate and state and the sudden change of the state won't change the slip rate on the fault, is one mechanism that can explain the delayed fault failure. *Gomberg et al.* (1998) indicate that the sudden stressing of a population of faults, even if the amplitude is very small, can lead to a cluster of triggered earthquakes on the fault is critically stressed. On another hand, *Atkinson* (1984) uses the subcritical crack growth model to explain the accelerating failure process. He infers that the intensity of stress at the crack tip, which is proportional to crack size, controls the rate of crack growth. When there is a sudden change of stress, the cracks become larger from the increase in stress at the crack tip, and thus accelerate the growth of cracks, and leading to a delayed fault rupture. Only a few earthquakes occurred on the newly-inferred normal fault before

the Papanoa earthquake. Thus, we conjecture the time-dependent acceleration to failure process to be the primary mechanism that leads to the seismic rate changes on this new fault.

An alternative class of mechanisms to explain the delayed triggering phenomenon is that the Papanoa earthquake may have triggered a local creep or slow slip event (SSE) in the study region and then the stress changes due to the creep or SSE triggered the local earthquakes. Based on the seismic and geodetic data, *Wdowinski* (2009) propose that deep creep causes excess seismicity along the San Jacinto fault, and *Shelly et al.* (2011) show that fault creep and triggered tremor initiated by remote earthquakes can last for several days after the passage of teleseismic waves, resulting in a prolonged increase of local seismicity. Other studies have shown that slow slip events (SSEs) can trigger both small and large earthquakes, with the triggering process sustaining as the SSE evolves in space and time (*Kato et al.*, 2012; *Delahaye et al.*, 2009; *Peng and Gomberg*, 2010; *Vidale et al.*, 2011). *Radiguet et al.* (2016) infers that a SSE in Guerrero, Mexico triggered the 2014 M_w 7.2 Papanoa earthquake. While we do not find direct evidence of fault creep or SSE during this period of elevated seismicity, this may be because of the slip is too small to be detectable. Recent studies have identified tectonic tremors in the study region (*Wang et al.*, 2013; *Hutchison and Ghosh*, 2017). Even though there are observations that SSE and tremors are occurring independently (*Delahaye et al.*, 2009; *Li and Ghosh*, 2017), generally, they are associated with each other and are known as episodic tremor and slow slip events (ETS) (*Ito et al.*, 2007; *Ghosh et al.*, 2015). Tremor and slow slip are most likely results of the same physical processes along the fault plane (e.g. *Ghosh et al.*, 2012). Thus a triggered

SSE or fault creep in the study region and may be responsible for the delayed and sustained increase of seismicity on the SJF.

Another possible mechanisms for the delayed triggering could be the increase of pore pressure due to the oscillatory stresses that are initiated by seismic waves. When the dilatation component of compressional waves interacts with the fluids in the crust, it can rupture fluid seals within the fault and produce subsequent fluid flow leading to the increase of pore pressure (*Hill et al.*, 1993). Previous studies have observed sustained water level changes in Oregon and at Long Valley Caldera, California that are associated with remote earthquakes up to several thousand miles away (*Brodsky et al.*, 2003; *Roeloffs et al.*, 2003).

It has yet to be determined whether the aforementioned primary and secondary mechanisms could fully explain the delayed triggering and sustained increase of seismicity in the study region. It is possible that there is more than one physical mechanism at play after the passage of the teleseismic waves of the Papanoa earthquake.

4.6 Conclusions

In this study, we use the move max matched-filter method to find delayed dynamic triggering of small earthquakes, and we detect abundant seismicity in the San Jacinto fault region between one month before and after the 2014 M_w Papanoa earthquake. The MMMF method detects about 5.4 times the amount of local seismicity found in the ANSS and SCSN catalogs, and 1.7 times the amount of seismicity identified by the traditional matched-filter method, thus greatly improving the completeness of the current earthquake catalog. Although there is no observation of dynamically triggered events during the passage of

the teleseismic waves, we find a significant increase in the seismicity rate that begins a few hours after the coda and persists for about one week before decaying back down to the background seismicity level. More than one mechanism could be responsible for these observations. They include but are not limited to: (1) The dynamic stress initiating a time-dependent acceleration to failure, (2) secondary mechanisms such as fault creep or a slow slip event, or (3) a transient increase in pore pressure. Relocations of detected seismicity show several linear clusters of seismicity occurring along the SJF systems and reveal depth changes to shallow from northwest to the Anza gap, and then become deeper when the locations move away to the southeast. Lastly, a cluster of delayed triggering seismicity off SJF implies the existence of an unmapped fault that is trending nearly perpendicular to the SJF. This blind fault is located west of the Anza gap and the city Anza, and if coseismically triggered it might cause more serious damage to the surrounding region when a large earthquake breaks the SJF.

Chapter 5

Conclusions

The back-projection method images three rupture patches of the 2015 M_w 8.3 Illapel earthquake, and the rupture was bounded along-strike by two fracture zones to the north and south. It has also been applied to the 2015 M_w 7.8 Gorkha earthquake, which shows $\sim$ 140 km eastward rupture along the Main Himalayan Thrust fault for about 60s and a northeast branch rupture at $\sim$ 45s. In addition to its application to quickly imaging the rupture process of large earthquakes, the back-projection method also shows it has capability for aftershock detection, especially when combining multiple arrays to improve the azimuth coverage and resolution. Thus it provides another way to study earthquakes where there is no or limited local/regional seismic stations, like the seismicity in the middle of the ocean. However, there are still questions about this method that remain unaddressed. Such as how does the rupture jump from one patch to another patch, as we see in the back-projection results of the Illapel earthquake; why can different arrays reveal different rupture features for the same event, which is shown in the Gorkha earthquake, with three arrays

revealing the northeast branch rupture while one array just show unidirectional rupture to the east; and what is the physical meaning behind the back-projection results or how can we link the back-projection result with the physical properties on the fault?

In a continued project, cooperated with Baoning and David, we compare the back-projection results with some kinematic models. The preliminary results indicate that the back-projection results tend to track heterogeneous ruptures, where the fault geometry, slip rate, and/or rupture velocity change. Higher frequency back-projection results are able to track smaller heterogeneity variations, which agree with the frequency dependent rupture observations [Kiser and Ishii, 2011; Kopper et al., 2011; Lay et al., 2012. Short-period radiation comes from the downdip part of the subduction fault, where we believe smaller asperities are distributed [Lay et al., 2012]. Rupture directivity can change the frequency of source energy due to the Doppler effect, and the back-projection tends to image the rupture in a direction that is preferred by the array for a certain frequency band, this could explain why different arrays sometimes capture different features of the same event rupture. In future, more models will be designed and synthetic tests will be done to help us better understand the link between the fault ruptures and the back-projection results.

Regarding the study of slow earthquakes, there are two popular hypotheses to explain the generation of tremor. One is that tremor is generated by the movement of fluids at depth, either by hydraulic fracturing [K. Obara, 2002; T. Seno T. Yamasaki, 2003] or by coupling between the rock and fluid flow [Katsumata and Kamaya, 2003]. Alternatively, tremor is generated directly by slow shear slip on the plate interface [K. Obara Hirose, 2006]. Tremors in the Unalaska and Akutan region show a depth range

between 45 to 60 km, which is deeper than the 30-35 km depth range in SW Japan, the 30-40 km depth range in northern Cascadia and Costa Rica, and 40 km depth in Guerrero, Mexico [Brown et al, 2009, Zigone et al, 2012]. This may indicate tremors are fluid driven activities [Miyazawa Mori, 2006; Rubinstein et al., 2007], since the incoming plate in the study region is older, faster, and colder than other places, the hydrous mineral fluids are generally released at greater depth [Van Keken, et al., 2011; Abers, 2013; Brown et al., 2013]. The heterogeneous distribution of slow earthquakes indicates both the along-dip and lateral frictional variabilities of the plate interface. Tremors in our study region cluster in multiple patches, with fewer active tremor segments in between. The yearlong tremor behavior suggests these gaps are temporally stable features and may represent aseismic creeping segments in the transition zone. The local earthquake catalog shows that the fast earthquakes locate at the updip edges of the tremor patches, which indicate tremors could be used to delineate the boundary of transitional asperities and the downdip extent of ruptures of large earthquakes [Ide et al., 2007]. In addition, the slow earthquake studies in the dissertation do show that there is interaction with fast earthquakes. Multiple cases have been observed where local or regional earthquakes show strong temporal correlation with tremor activities, either initiation or termination with tremor bursts, depending on their locations. But we are unable to figure out how the stress transfers between the seismogenic zone and the transition zone, mostly due to the limited azimuth coverage of seismic stations. In future, we plan to investigate more about their relationship in a region where fast and slow earthquakes are active, with good azimuth and station coverage.

Tremors are thought to be comprised of LFE signals [Shelly et al., 2007a, 2007b; Brown et al., 2009]. Here we observe strong spatio-temporal correlation between tremor signals and LFE activities. LFEs are located in the tremor patches and show bursts during the tremor signals. However, there are also some LFEs that do not temporally coincide with tremor activities. This may be due to the incomplete detection of tremors because of the limited station coverage, or that LFEs can occur independently in discrete small asperities that are not enough to produce tremor signals. LFEs are small seismic events generated by slip on relatively small on-fault asperities [Ide et al., 2007; Royer and Bostock, 2014] and can be applied as creepmeters to study deep slips of a fault [Thomas et al., 2017]. The study region is located at the eastern and down-dip edge of the rupture zone of the 1957 M_w 8.6 earthquake and to the west of the 1938 M_w 8.2 megathrust earthquakes, and it has not been ruptured for a long time. The prolific tremor activities and LFEs may transfer the stress updip to the seismogenic zone and clock advance the occurrence of next large earthquake.

Delayed triggering of small earthquakes in SJF by a teleseismic large earthquake in Mexico is found. More than one mechanism may be responsible for the delayed triggering earthquakes in the SJF region by the 2014 M_w 7.2 Papanoa earthquake. A local creep or small SSE triggered by the teleseismic event changes the stress and trigger the earthquakes on the SJF. Previous studies have identified tectonic tremors, slow slip and deep creep in the SJF region [Inbal et al., 2017; Lindsay et al., 2014; Jiang and Fialko, 2016; Hutchison Ghosh, 2017]. The dynamic stress due to the passage of teleseismic waves may initiate a time-dependent acceleration to failure process and trigger the earthquakes on the unmapped

fault, off the SJF. This new fault is close to the Anza gap, where previous studies show the potential for a M_w 6.5 or larger earthquake [Thatcher et al., 1975; Sanders and Kanamori, 1984], which can activate the rupture on this unmapped fault and result in more serious damage in the surrounding region. On the other hand, slip on the unmapped fault may potentially help nucleate damaging earthquake in San Jacinto Fault.

The studies presented here provide some understanding of the fault slips in the seismogenic and transition zones, the interactions between them and among different faults. There is still much research that needs to be done to explore the detailed fault slip behaviors and their relation with fault properties, and stress transfer on or among faults. A combination of seismology studies as described here, with geodetic data, dynamic rupture modeling and lab experiments, as a whole can improve our understanding of the broad spectrum of fault slip behaviors, and contribute to our understanding of earthquake physics, related hazards and their assessment.

Bibliography

Abers, G. A., J. Nakajima, P. E. van Keken, S. Kita, and B. R. Hacker (2013), Thermal–petrological controls on the location of earthquakes within subducting plates, *Earth and Planetary Science Letters*, *369*, 178–187.

Acton, C., K. Priestley, V. Gaur, and S. Rai (2010), Group velocity tomography of the indo-eurasian collision zone, *Journal of Geophysical Research: Solid Earth*, *115*(B12).

Ader, T., J.-P. Avouac, J. Liu-Zeng, H. Lyon-Caen, L. Bollinger, J. Galetzka, J. Genrich, M. Thomas, K. Chanard, S. N. Sapkota, et al. (2012), Convergence rate across the nepal himalaya and interseismic coupling on the main himalayan thrust: Implications for seismic hazard, *Journal of Geophysical Research: Solid Earth*, *117*(B4).

Adhikari, L., U. Gautam, B. Koirala, M. Bhattarai, T. Kandel, R. Gupta, C. Timsina, N. Maharjan, K. Maharjan, T. Dahal, et al. (2015), The aftershock sequence of the 2015 april 25 gorkha–nepal earthquake, *Geophysical Supplements to the Monthly Notices of the Royal Astronomical Society*, *203*(3), 2119–2124.

Atkinson, B. K. (1984), Subcritical crack growth in geological materials, *Journal of Geophysical Research: Solid Earth*, *89*(B6), 4077–4114.

Avouac, J.-P., L. Meng, S. Wei, T. Wang, and J.-P. Ampuero (2015), Lower edge of locked main himalayan thrust unzipped by the 2015 gorkha earthquake, *Nature Geoscience*, *8*(9), 708.

Bailey, I. W., Y. Ben-Zion, T. W. Becker, and M. Holschneider (2010), Quantifying focal mechanism heterogeneity for fault zones in central and southern california, *Geophysical Journal International*, *183*(1), 433–450.

Baker, T., R. Granat, and R. W. Clayton (2005), Real-time earthquake location using kirchhoff reconstruction, *Bulletin of the Seismological Society of America*, *95*(2), 699–707.

Barazangi, M., and B. L. Isacks (1976), Spatial distribution of earthquakes and subduction of the nazca plate beneath south america, *Geology*, *4*(11), 686–692.

Barrientos, S. E. (1995), Dual seismogenic behavior: the 1985 central chile earthquake, *Geophysical Research Letters*, *22*(24), 3541–3544.

Bartlow, N. M., S. Miyazaki, A. M. Bradley, and P. Segall (2011), Space-time correlation of slip and tremor during the 2009 cascadia slow slip event, *Geophysical Research Letters*, *38*(18).

Beck, S., S. Barrientos, E. Kausel, and M. Reyes (1998), Source characteristics of historic earthquakes along the central chile subduction askew et alzone, *Journal of South American Earth Sciences*, *11*(2), 115–129.

Bilham, R. (2015), Seismology: raising kathmandu, *Nature Geoscience*, *8*(8), 582.

Bostock, M., A. Royer, E. Hearn, and S. Peacock (2012), Low frequency earthquakes below southern vancouver island, *Geochemistry, Geophysics, Geosystems*, *13*(11).

Brace, W., and J. Byerlee (1966), Stick-slip as a mechanism for earthquakes, *Science*, *153*(3739), 990–992.

Brodsky, E. E., E. Roeloffs, D. Woodcock, I. Gall, and M. Manga (2003), A mechanism for sustained groundwater pressure changes induced by distant earthquakes, *Journal of Geophysical Research: Solid Earth*, *108*(B8).

Brown, J. R., G. C. Beroza, and D. R. Shelly (2008), An autocorrelation method to detect low frequency earthquakes within tremor, *Geophysical Research Letters*, *35*(16).

Brown, J. R., G. C. Beroza, S. Ide, K. Ohta, D. R. Shelly, S. Y. Schwartz, W. Rabbel, M. Thorwart, and H. Kao (2009), Deep low-frequency earthquakes in tremor localize to the plate interface in multiple subduction zones, *Geophysical Research Letters*, *36*(19).

Brown, J. R., S. G. Prejean, G. C. Beroza, J. S. Gomberg, and P. J. Haeussler (2013), Deep low-frequency earthquakes in tectonic tremor along the alaska-aleutian subduction zone, *Journal of Geophysical Research: solid earth*, *118*(3), 1079–1090.

Caldwell, W. B., S. L. Klemperer, J. F. Lawrence, S. S. Rai, et al. (2013), Characterizing the main himalayan thrust in the garhwal himalaya, india with receiver function ccp stacking, *Earth and Planetary Science Letters*, *367*, 15–27.

Cocco, M., S. Hainzl, F. Catalli, B. Enescu, A. Lombardi, and J. Woessner (2010), Sensitivity study of forecasted aftershock seismicity based on coulomb stress calculation and rate-and state-dependent frictional response, *Journal of Geophysical Research: Solid Earth*, *115*(B5).

Contreras-Reyes, E., and D. Carrizo (2011), Control of high oceanic features and subduction channel on earthquake ruptures along the chile–peru subduction zone, *Physics of the Earth and Planetary Interiors*, *186*(1-2), 49–58.

Contreras-Reyes, E., I. Grevemeyer, E. R. Flueh, and C. Reichert (2008), Upper lithospheric structure of the subduction zone offshore of southern arauco peninsula, chile, at 38 s, *Journal of Geophysical Research: Solid Earth*, *113*(B7).

Cross, R. S., and J. T. Freymueller (2008), Evidence for and implications of a bering plate based on geodetic measurements from the aleutians and western alaska, *Journal of Geophysical Research: Solid Earth*, *113*(B7).

Das, S., and K. Aki (1977), Fault plane with barriers: a versatile earthquake model, *Journal of geophysical research*, *82*(36), 5658–5670.

Delahaye, E., J. Townend, M. Reyners, and G. Rogers (2009), Microseismicity but no tremor accompanying slow slip in the hikurangi subduction zone, new zealand, *Earth and Planetary Science Letters*, *277*(1-2), 21–28.

Delouis, B., J.-M. Nocquet, and M. Vallée (2010), Slip distribution of the february 27, 2010 mw= 8.8 maule earthquake, central chile, from static and high-rate gps, insar, and broadband teleseismic data, *Geophysical Research Letters*, *37*(17).

DeMets, C., R. G. Gordon, D. F. Argus, and S. Stein (1994), Effect of recent revisions to the geomagnetic reversal time scale on estimates of current plate motions, *Geophysical research letters*, *21*(20), 2191–2194.

Dieterich, J. (1994), A constitutive law for rate of earthquake production and its application to earthquake clustering, *Journal of Geophysical Research: Solid Earth*, *99*(B2), 2601–2618.

Dieterich, J. H. (1979), Modeling of rock friction: 1. experimental results and constitutive equations, *Journal of Geophysical Research: Solid Earth*, *84*(B5), 2161–2168.

Dieterich, J. H. (1981), Constitutive properties of faults with simulated gouge, *Mechanical behavior of crustal rocks: the Handin volume*, *24*, 103–120.

Dragert, H., K. Wang, and T. S. James (2001), A silent slip event on the deeper cascadia subduction interface, *Science*, *292*(5521), 1525–1528.

Ellsworth, W. L., J. Luetgert, and D. Oppenheimer (2005), Borehole array observations of non-volcanic tremor at safod, in *AGU Fall Meeting Abstracts*.

Fan, W., and P. M. Shearer (2015), Detailed rupture imaging of the 25 april 2015 nepal earthquake using teleseismic p waves, *Geophysical Research Letters*, *42*(14), 5744–5752.

Fogleman, K. A., J. C. Lahr, C. D. Stephens, and R. A. Page (1993), Earthquake locations determined by the southern alaska seismograph network for october 1971 through may 1989, *Tech. rep.*, US Geological Survey.

Frank, W., and N. Shapiro (2014), Automatic detection of low-frequency earthquakes (lfes) based on a beamformed network response, *Geophysical Journal International*, *197*(2), 1215–1223.

Frank, W. B. (2016), Slow slip hidden in the noise: The intermittence of tectonic release, *Geophysical Research Letters*, *43*(19), 10–125.

Frank, W. B., N. M. Shapiro, V. Kostoglodov, A. L. Husker, M. Campillo, J. S. Payero, and G. A. Prieto (2013), Low-frequency earthquakes in the mexican sweet spot, *Geophysical Research Letters*, *40*(11), 2661–2666.

Frank, W. B., N. M. Shapiro, A. L. Husker, V. Kostoglodov, H. S. Bhat, and M. Campillo (2015), Along-fault pore-pressure evolution during a slow-slip event in guerrero, mexico, *Earth and Planetary Science Letters*, *413*, 135–143.

Freed, A. M. (2005), Earthquake triggering by static, dynamic, and postseismic stress transfer, *Annu. Rev. Earth Planet. Sci.*, *33*, 335–367.

Freymueller, J. T., H. Woodard, S. C. Cohen, R. Cross, J. Elliott, C. F. Larsen, S. Hreinsdottir, C. Zweck, P. Haeussler, R. Wesson, et al. (2008), Active deformation processes in alaska, based on 15 years of gps measurements, *Active tectonics and seismic potential of Alaska*, *179*, 1–42.

Fromm, R., G. Zandt, and S. Beck (2004), Crustal thickness beneath the andes and sierras pampeanas at 30 s inferred from pn apparent phase velocities, *Geophysical Research Letters*, *31*(6).

Gershenzon, N. I., G. Bambakidis, E. Hauser, A. Ghosh, and K. C. Creager (2011), Episodic tremors and slip in cascadia in the framework of the frenkel-kontorova model, *Geophysical Research Letters*, *38*(1).

Ghosh, A., J. E. Vidale, J. R. Sweet, K. C. Creager, and A. G. Wech (2009), Tremor patches in cascadia revealed by seismic array analysis, *Geophysical Research Letters*, *36*(17).

Ghosh, A., J. E. Vidale, J. R. Sweet, K. C. Creager, A. G. Wech, and H. Houston (2010a), Tremor bands sweep cascadia, *Geophysical Research Letters*, *37*(8).

Ghosh, A., J. E. Vidale, J. R. Sweet, K. C. Creager, A. G. Wech, H. Houston, and E. E. Brodsky (2010b), Rapid, continuous streaking of tremor in cascadia, *Geochemistry, Geophysics, Geosystems*, *11*(12).

Ghosh, A., J. E. Vidale, and K. C. Creager (2012), Tremor asperities in the transition zone control evolution of slow earthquakes, *Journal of Geophysical Research: Solid Earth*, *117*(B10).

Ghosh, A., E. Huesca-Pérez, E. Brodsky, and Y. Ito (2015), Very low frequency earthquakes in cascadia migrate with tremor, *Geophysical Research Letters*, *42*(9), 3228–3232.

Gomberg, J., and S. Prejean (2013), Triggered tremor sweet spots in alaska, *Journal of Geophysical Research: Solid Earth*, *118*(12), 6203–6218.

Gomberg, J., N. Beeler, M. Blanpied, and P. Bodin (1998), Earthquake triggering by transient and static deformations, *Journal of Geophysical Research: Solid Earth*, *103*(B10), 24,411–24,426.

Grandin, R., M. Vallée, C. Satriano, R. Lacassin, Y. Klinger, M. Simoes, and L. Bollinger (2015), Rupture process of the mw= 7.9 2015 gorkha earthquake (nepal): Insights into himalayan megathrust segmentation, *Geophysical Research Letters*, *42*(20), 8373–8382.

Gutenberg, B., and C. F. Richter (1956), Earthquake magnitude, intensity, energy, and acceleration: (second paper), *Bulletin of the seismological society of America*, *46*(2), 105–145.

Hartzell, S. H., and T. H. Heaton (1983), Inversion of strong ground motion and teleseismic waveform data for the fault rupture history of the 1979 imperial valley, california, earthquake, *Bulletin of the Seismological Society of America*, *73*(6A), 1553–1583.

Hayes, G. P., D. J. Wald, and R. L. Johnson (2012), Slab1. 0: A three-dimensional model of global subduction zone geometries, *Journal of Geophysical Research: Solid Earth*, *117*(B1).

Heaton, T. H. (1990), Evidence for and implications of self-healing pulses of slip in earthquake rupture, *Physics of the Earth and Planetary Interiors*, *64*(1), 1–20.

Heaton, T. H., and D. V. Helmberger (1979), Generalized ray models of the san fernando earthquake, *Bulletin of the Seismological Society of America*, *69*(5), 1311–1341.

Heidarzadeh, M., S. Murotani, K. Satake, T. Ishibe, and A. R. Gusman (2016), Source model of the 16 september 2015 illapel, chile, mw 8.4 earthquake based on teleseismic and tsunami data, *Geophysical Research Letters*, *43*(2), 643–650.

Hill, D. P., P. Reasenberg, A. Michael, W. Arabaz, G. Beroza, D. Brumbaugh, J. Brune, R. Castro, S. Davis, W. Ellsworth, et al. (1993), Seismicity remotely triggered by the magnitude 7.3 landers, california, earthquake, *Science*, *260*(5114), 1617–1623.

Hirose, H., K. Hirahara, F. Kimata, N. Fujii, and S. Miyazaki (1999), A slow thrust slip event following the two 1996 hyuganada earthquakes beneath the bungo channel, southwest japan, *Geophysical Research Letters*, *26*(21), 3237–3240.

Hsu, Y.-J., M. Simons, J.-P. Avouac, J. Galetzka, K. Sieh, M. Chlieh, D. Natawidjaja, L. Prawirodirdjo, and Y. Bock (2006), Frictional afterslip following the 2005 nias-simeulue earthquake, sumatra, *Science*, *312*(5782), 1921–1926.

Huene, R. v., J. Corvalán, E. Flueh, K. Hinz, J. Korstgard, C. Ranero, and W. Weinrebe (1997), Tectonic control of the subducting juan fernández ridge on the andean margin near valparaiso, chile, *Tectonics*, *16*(3), 474–488.

Husker, A. L., V. Kostoglodov, V. M. Cruz-Atienza, D. Legrand, N. M. Shapiro, J. S. Payero, M. Campillo, and E. Huesca-Pérez (2012), Temporal variations of non-volcanic tremor (nvt) locations in the mexican subduction zone: Finding the nvt sweet spot, *Geochemistry, Geophysics, Geosystems*, *13*(3).

Hutchison, A. A., and A. Ghosh (2016), Very low frequency earthquakes spatiotemporally asynchronous with strong tremor during the 2014 episodic tremor and slip event in cascadia, *Geophysical Research Letters*, *43*(13), 6876–6882.

Hutchison, A. A., and A. Ghosh (2017), Ambient tectonic tremor in the san jacinto fault, near the anza gap, detected by multiple mini seismic arraysambient tectonic tremor in the san jacinto fault, near the anza gap, detected by multiple mini seismic arrays, *Bulletin of the Seismological Society of America*, *107*(5), 1985–1993.

Ide, S., D. R. Shelly, and G. C. Beroza (2007a), Mechanism of deep low frequency earthquakes: Further evidence that deep non-volcanic tremor is generated by shear slip on the plate interface, *Geophysical Research Letters*, *34*(3).

Ide, S., G. C. Beroza, D. R. Shelly, and T. Uchide (2007b), A scaling law for slow earthquakes, *Nature*, *447*(7140), 76.

Ishii, M., P. M. Shearer, H. Houston, and J. E. Vidale (2005), Extent, duration and speed of the 2004 sumatra–andaman earthquake imaged by the hi-net array, *Nature*, *435*(7044), 933.

Ito, Y., K. Obara, K. Shiomi, S. Sekine, and H. Hirose (2007), Slow earthquakes coincident with episodic tremors and slow slip events, *Science*, *315*(5811), 503–506.

Johnson, C. W., R. Bürgmann, and F. F. Pollitz (2015), Rare dynamic triggering of remote m 5.5 earthquakes from global catalog analysis, *Journal of Geophysical Research: Solid Earth*, *120*(3), 1748–1761.

Kagan, Y. Y. (2004), Short-term properties of earthquake catalogs and models of earthquake source, *Bulletin of the Seismological Society of America*, *94*(4), 1207–1228.

Kagan, Y. Y., and H. Houston (2005), Relation between mainshock rupture process and omoris law for aftershock moment release rate, *Geophysical Journal International*, *163*(3), 1039–1048.

Kagan, Y. Y., D. D. Jackson, and Y. Rong (2006), A new catalog of southern california earthquakes, 1800–2005, *Seismological Research Letters*, *77*(1), 30–38.

Kao, H., and S. Shan (2004), Delineation of rupture propagation of large earthquakes using source-scanning algorithm: A control study, in *AGU Fall Meeting Abstracts*.

Kao, H., and S.-J. Shan (2007), Rapid identification of earthquake rupture plane using source-scanning algorithm, *Geophysical Journal International*, *168*(3), 1011–1020.

Kato, A., K. Obara, T. Igarashi, H. Tsuruoka, S. Nakagawa, and N. Hirata (2012), Propagation of slow slip leading up to the 2011 mw 9.0 tohoku-oki earthquake, *Science*, *335*(6069), 705–708.

Katsumata, A., and N. Kamaya (2003), Low-frequency continuous tremor around the moho discontinuity away from volcanoes in the southwest japan, *Geophysical Research Letters*, *30*(1), 20–1.

Kelleher, J. A. (1972), Rupture zones of large south american earthquakes and some predictions, *Journal of Geophysical Research*, *77*(11), 2087–2103.

Kennett, B., and E. Engdahl (1991), Traveltimes for global earthquake location and phase identification, *Geophysical Journal International*, *105*(2), 429–465.

Kilb, D., V. G. Martynov, and F. L. Vernon (2007), Aftershock detection thresholds as a function of time: Results from the anza seismic network following the 31 october 2001 ml 5.1 anza, california, earthquake, *Bulletin of the Seismological Society of America*, *97*(3), 780–792.

King, G. C., R. S. Stein, and J. Lin (1994), Static stress changes and the triggering of earthquakes, *Bulletin of the Seismological Society of America*, *84*(3), 935–953.

Kiser, E., and M. Ishii (2011), The 2010 mw 8.8 chile earthquake: Triggering on multiple segments and frequency-dependent rupture behavior, *Geophysical Research Letters*, *38*(7).

Kiser, E., and M. Ishii (2012), Combining seismic arrays to image the high-frequency characteristics of large earthquakes, *Geophysical Journal International*, *188*(3), 1117–1128.

Kiser, E., and M. Ishii (2013), Hidden aftershocks of the 2011 mw 9.0 tohoku, japan earthquake imaged with the backprojection method, *Journal of Geophysical Research: Solid Earth*, *118*(10), 5564–5576.

Kiser, E., and M. Ishii (2017), Back-projection imaging of earthquakes, *Annual Review of Earth and Planetary Sciences*, *45*, 271–299.

Klein, F. W. (2002), User's guide to hypoinverse-2000, a fortran program to solve for earthquake locations and magnitudes, *Tech. rep.*, US Geological Survey.

Koper, K. D., A. R. Hutko, T. Lay, C. J. Ammon, and H. Kanamori (2011), Frequency-dependent rupture process of the 2011 m w 9.0 tohoku earthquake: Comparison of short-period p wave backprojection images and broadband seismic rupture models, *Earth, planets and space*, *63*(7), 16.

Kostoglodov, V., A. Husker, N. M. Shapiro, J. S. Payero, M. Campillo, N. Cotte, and R. Clayton (2010), The 2006 slow slip event and nonvolcanic tremor in the mexican subduction zone, *Geophysical Research Letters*, *37*(24).

Krüger, F., and M. Ohrnberger (2005), Spatio-temporal source characteristics of the 26 december 2004 sumatra earthquake as imaged by teleseismic broadband arrays, *Geophysical research letters*, *32*(24).

Lay, T., C. Ammon, H. Kanamori, K. Koper, O. Sufri, and A. Hutko (2010), Teleseismic inversion for rupture process of the 27 february 2010 chile (mw 8.8) earthquake, *Geophysical Research Letters*, *37*(13).

Lengliné, O., B. Enescu, Z. Peng, and K. Shiomi (2012), Decay and expansion of the early aftershock activity following the 2011, mw9. 0 tohoku earthquake, *Geophysical research letters*, *39*(18).

Li, B., and A. Ghosh (2017), Near-continuous tremor and low-frequency earthquake activities in the alaska-aleutian subduction zone revealed by a mini seismic array, *Geophysical Research Letters*, *44*(11), 5427–5435.

Lolli, B., and P. Gasperini (2006), Comparing different models of aftershock rate decay: The role of catalog incompleteness in the first times after main shock, *Tectonophysics*, *423*(1-4), 43–59.

Lowrie, A. (1981), Geological and geophysical variations along the western margin of chile near latitude 33 to 36 s and their relation to nazca plate subduction, *Geol. Soc. Amer. Mem.*, *154*, 741–754.

Luo, Y., and J.-P. Ampuero (2017), Tremor migration patterns and the collective behavior of deep asperities mediated by creep.

MacAyeal, D. R., E. A. Okal, R. C. Aster, J. N. Bassis, K. M. Brunt, L. M. Cathles, R. Drucker, H. A. Fricker, Y.-J. Kim, S. Martin, et al. (2006), Transoceanic wave propagation links iceberg calving margins of antarctica with storms in tropics and northern hemisphere, *Geophysical Research Letters*, *33*(17).

Madariaga, R. (1977), High-frequency radiation from crack (stress drop) models of earthquake faulting, *Geophysical Journal International*, *51*(3), 625–651.

Marot, M., T. Monfret, M. Pardo, G. Ranalli, and G. Nolet (2013), A double seismic zone in the subducting juan fernandez ridge of the nazca plate (32 s), central chile, *Journal of Geophysical Research: Solid Earth*, *118*(7), 3462–3475.

Mazzotti, S., and J. Adams (2004), Variability of near-term probability for the next great earthquake on the cascadia subduction zone, *Bulletin of the Seismological Society of America*, *94*(5), 1954–1959.

McCann, W., S. Nishenko, L. Sykes, and J. Krause (1979), Seismic gaps and plate tectonics: seismic potential for major boundaries, in *Earthquake Prediction and Seismicity Patterns*, pp. 1082–1147, Springer.

Melgar, D., W. Fan, S. Riquelme, J. Geng, C. Liang, M. Fuentes, G. Vargas, R. M. Allen, P. M. Shearer, and E. J. Fielding (2016), Slip segmentation and slow rupture to the trench during the 2015, mw8. 3 illapel, chile earthquake, *Geophysical Research Letters*, *43*(3), 961–966.

Mendoza, C., and M. d. R. Martínez López (2017), The mw 7.3 papanoa, mexico earthquake of april 18, 2014: Implications for recurrent m¿ 7 thrust earthquakes in western guerrero, *Geofísica internacional*, *56*(1), 13–26.

Mendoza, M. M., A. Ghosh, and S. S. Rai (2016), Dynamic triggering of small local earthquakes in the central himalaya, *Geophysical Research Letters*, *43*(18), 9581–9587.

Meng, L., A. Inbal, and J.-P. Ampuero (2011), A window into the complexity of the dynamic rupture of the 2011 mw 9 tohoku-oki earthquake, *Geophysical Research Letters*, *38*(7).

Meng, L., J.-P. Ampuero, A. Sladen, and H. Rendon (2012), High-resolution backprojection at regional distance: Application to the haiti m7. 0 earthquake and comparisons with finite source studies, *Journal of Geophysical Research: Solid Earth*, *117*(B4).

Meng, X., and Z. Peng (2014), Seismicity rate changes in the salton sea geothermal field and the san jacinto fault zone after the 2010 m w 7.2 el mayor-cucapah earthquake, *Geophysical Journal International*, *197*(3), 1750–1762.

Métois, M., A. Socquet, and C. Vigny (2012), Interseismic coupling, segmentation and mechanical behavior of the central chile subduction zone, *Journal of Geophysical Research: Solid Earth*, *117*(B3).

Miyatake, T. (1992), Reconstruction of dynamic rupture process of an earthquake with constraints of kinematic parameters, *Geophysical research letters*, *19*(4), 349–352.

Miyazawa, M., and J. Mori (2006), Evidence suggesting fluid flow beneath japan due to periodic seismic triggering from the 2004 sumatra-andaman earthquake, *Geophysical Research Letters*, *33*(5).

Nábělek, J., G. Hetényi, J. Vergne, S. Sapkota, B. Kafle, M. Jiang, H. Su, J. Chen, B.-S. Huang, et al. (2009), Underplating in the himalaya-tibet collision zone revealed by the hi-climb experiment, *Science*, *325*(5946), 1371–1374.

Nadeau, R. M., and D. Dolenc (2005), Nonvolcanic tremors deep beneath the san andreas fault, *Science*, *307*(5708), 389–389.

Obara, K. (2002), Nonvolcanic deep tremor associated with subduction in southwest japan, *Science*, *296*(5573), 1679–1681.

Obara, K., T. Matsuzawa, S. Tanaka, T. Kimura, and T. Maeda (2011), Migration properties of non-volcanic tremor in shikoku, southwest japan, *Geophysical Research Letters*, *38*(9).

Ohta, K., and S. Ide (2011), Precise hypocenter distribution of deep low-frequency earthquakes and its relationship to the local geometry of the subducting plate in the nankai subduction zone, japan, *Journal of Geophysical Research: Solid Earth*, *116*(B1).

Olson, A. H., and R. J. Apsel (1982), Finite faults and inverse theory with applications to the 1979 imperial valley earthquake, *Bulletin of the Seismological Society of America*, *72*(6A), 1969–2001.

Ozawa, S., M. Murakami, and T. Tada (2001), Time-dependent inversion study of the slow thrust event in the nankai trough subduction zone, southwestern japan, *Journal of Geophysical Research: Solid Earth*, *106*(B1), 787–802.

Payero, J. S., V. Kostoglodov, N. Shapiro, T. Mikumo, A. Iglesias, X. Pérez-Campos, and R. W. Clayton (2008), Nonvolcanic tremor observed in the mexican subduction zone, *Geophysical Research Letters*, *35*(7).

Peng, Z., and K. Chao (2008), Non-volcanic tremor beneath the central range in taiwan triggered by the 2001 m w 7.8 kunlun earthquake, *Geophysical Journal International*, *175*(2), 825–829.

Peng, Z., and J. Gomberg (2010), An integrated perspective of the continuum between earthquakes and slow-slip phenomena, *Nature geoscience*, *3*(9), 599.

Peterson, C., S. R. McNutt, and D. Christensen (2011), Nonvolcanic tremor in the aleutian arc, *Bulletin of the Seismological Society of America*, *101*(6), 3081–3087.

PILGER JR, R. H. (1981), Plate reconstructions, aseismic ridges, and low-angle subduction beneath the andes, *Geological Society of America Bulletin*, *92*(7), 448–456.

Prejean, S., and D. Hill (2009), Dynamic triggering of earthquakes, *Encyclopedia of Complexity and Systems Science, RA Meyers (Ed.), Springer*, pp. 2600–2621.

Radiguet, M., H. Perfettini, N. Cotte, A. Gualandi, B. Valette, V. Kostoglodov, T. Lhomme, A. Walpersdorf, E. C. Cano, and M. Campillo (2016), Triggering of the 2014 m w 7.3 papanoa earthquake by a slow slip event in guerrero, mexico, *Nature Geoscience*, *9*(11), 829.

Rivet, D., M. Campillo, N. M. Shapiro, V. Cruz-Atienza, M. Radiguet, N. Cotte, and V. Kostoglodov (2011), Seismic evidence of nonlinear crustal deformation during a large slow slip event in mexico, *Geophysical Research Letters*, *38*(8).

Rockwell, T., C. Loughman, and P. Merifield (1990), Late quaternary rate of slip along the san jacinto fault zone near anza, southern california, *Journal of Geophysical Research: Solid Earth*, *95*(B6), 8593–8605.

Roeloffs, E., M. Sneed, D. L. Galloway, M. L. Sorey, C. D. Farrar, J. F. Howle, and J. Hughes (2003), Water-level changes induced by local and distant earthquakes at long valley caldera, california, *Journal of Volcanology and Geothermal Research*, *127*(3-4), 269–303.

Rogers, G., and H. Dragert (2003), Episodic tremor and slip on the cascadia subduction zone: The chatter of silent slip, *Science*, *300*(5627), 1942–1943.

Royer, A., and M. Bostock (2014), A comparative study of low frequency earthquake templates in northern cascadia, *Earth and Planetary Science Letters*, *402*, 247–256.

Rubin, A. M. (2011), Designer friction laws for bimodal slow slip propagation speeds, *Geochemistry, Geophysics, Geosystems*, *12*(4).

Rubinstein, J. L., M. La Rocca, J. E. Vidale, K. C. Creager, and A. G. Wech (2008), Tidal modulation of nonvolcanic tremor, *Science*, *319*(5860), 186–189.

Rubinstein, J. L., D. R. Shelly, and W. L. Ellsworth (2009), Non-volcanic tremor: A window into the roots of fault zones, in *New Frontiers in Integrated Solid Earth Sciences*, pp. 287–314, Springer.

Ruppert, N. A., J. M. Lees, N. P. Kozyreva, and J. Eichelberger (2007), Seismicity, earthquakes and structure along the alaska-aleutian and kamchatka-kurile subduction zones: A review, *GEOPHYSICAL MONOGRAPH-AMERICAN GEOPHYSICAL UNION*, *172*, 129.

Sanders, C. O., and H. Kanamori (1984), A seismotectonic analysis of the anza seismic gap, san jacinto fault zone, southern california, *Journal of Geophysical Research: Solid Earth*, *89*(B7), 5873–5890.

Scholz, C. (1999), Earthquakes prediction: feasible and useful, *Nature Debates*, *4*.

Schwartz, S. Y., and J. M. Rokosky (2007), Slow slip events and seismic tremor at circum-pacific subduction zones, *Reviews of Geophysics*, *45*(3).

Scott, J. S., T. G. Masters, and F. L. Vernon (1994), 3-d velocity structure of the san jacinto fault zone near anza, californiai. p waves, *Geophysical Journal International*, *119*(2), 611–626.

Shelly, D. R., G. C. Beroza, S. Ide, and S. Nakamula (2006), Low-frequency earthquakes in shikoku, japan, and their relationship to episodic tremor and slip, *Nature*, *442*(7099), 188.

Shelly, D. R., G. C. Beroza, and S. Ide (2007a), Non-volcanic tremor and low-frequency earthquake swarms, *Nature*, *446*(7133), 305.

Shelly, D. R., G. C. Beroza, and S. Ide (2007b), Complex evolution of transient slip derived from precise tremor locations in western shikoku, japan, *Geochemistry, Geophysics, Geosystems*, *8*(10).

Shelly, D. R., Z. Peng, D. P. Hill, and C. Aiken (2011), Triggered creep as a possible mechanism for delayed dynamic triggering of tremor and earthquakes, *Nature Geoscience*, *4*(6), 384.

Sladen, A., H. Tavera, M. Simons, J. Avouac, A. Konca, H. Perfettini, L. Audin, E. Fielding, F. Ortega, and R. Cavagnoud (2010), Source model of the 2007 mw 8.0 pisco, peru earthquake: Implications for seismogenic behavior of subduction megathrusts, *Journal of Geophysical Research: Solid Earth*, *115*(B2).

Takeo, M. (1987), An inversion method to analyze the rupture processes of earthquakes using near-field seismograms, *Bulletin of the Seismological Society of America*, *77*(2), 490–513.

Tapponnier, P., and P. Molnar (1976), Slip-line field theory and large-scale continental tectonics, *Nature*, *264*(5584), 319.

Taylor, M., and A. Yin (2009), Active structures of the himalayan-tibetan orogen and their relationships to earthquake distribution, contemporary strain field, and cenozoic volcanism, *Geosphere*, *5*(3), 199–214.

Tebbens, S., S. Cande, L. Kovacs, J. Parra, J. LaBrecque, and H. Vergara (1997), The chile ridge: A tectonic framework, *Journal of Geophysical Research: Solid Earth*, *102*(B6), 12,035–12,059.

Thatcher, W., J. A. Hileman, and T. C. Hanks (1975), Seismic slip distribution along the san jacinto fault zone, southern california, and its implications, *Geological Society of America Bulletin*, *86*(8), 1140–1146.

Thomas, T. W., J. E. Vidale, H. Houston, K. C. Creager, J. R. Sweet, and A. Ghosh (2013), Evidence for tidal triggering of high-amplitude rapid tremor reversals and tremor streaks in northern cascadia, *Geophysical Research Letters*, *40*(16), 4254–4259.

Thorwart, M., Y. Dzierma, W. Rabbel, E. R. Flueh, W. Taylor, G. Alvarado, and M. Mora (2007), Receiver function and non-volcanic tremor studies in costa rica.

Trifunac, M. (1974), A three-dimensional dislocation model for the san fernando, california, earthquake of february 9, 1971, *Bulletin of the Seismological Society of America*, *64*(1), 149–172.

van Keken, P. E., B. R. Hacker, E. M. Syracuse, and G. A. Abers (2011), Subduction factory: 4. depth-dependent flux of h2o from subducting slabs worldwide, *Journal of Geophysical Research: Solid Earth*, *116*(B1).

Vidale, J. E., A. J. Hotovec, A. Ghosh, K. C. Creager, and J. Gomberg (2011), Tiny intraplate earthquakes triggered by nearby episodic tremor and slip in cascadia, *Geochemistry, Geophysics, Geosystems*, *12*(6).

Wald, D. J., D. V. Helmberger, and T. H. Heaton (1991), Rupture model of the 1989 loma prieta earthquake from the inversion of strong-motion and broadband teleseismic data, *Bulletin of the Seismological Society of America*, *81*(5), 1540–1572.

Waldhauser, F. (2001), hypodd–a program to compute double-difference hypocenter locations.

Walker, K. T., M. Ishii, and P. M. Shearer (2005), Rupture details of the 28 march 2005 sumatra mw 8.6 earthquake imaged with teleseismic p waves, *Geophysical Research Letters*, *32*(24).

Wang, T.-H., E. S. Cochran, D. Agnew, and D. D. Oglesby (2013), Infrequent triggering of tremor along the san jacinto fault near anza, california, *Bulletin of the Seismological Society of America*, *103*(4), 2482–2497.

Wdowinski, S. (2009), Deep creep as a cause for the excess seismicity along the san jacinto fault, *Nature Geoscience*, *2*(12), 882.

Xu, Y., K. D. Koper, O. Sufri, L. Zhu, and A. R. Hutko (2009), Rupture imaging of the mw 7.9 12 may 2008 wenchuan earthquake from back projection of teleseismic p waves, *Geochemistry, Geophysics, Geosystems*, *10*(4).

Yamamoto, E., S. Matsumura, and T. Ohkubo (2005), A slow slip event in the tokai area detected by tilt and seismic observation and its possible recurrence, *Earth, planets and space*, *57*(10), 917–923.

Ye, L., T. Lay, H. Kanamori, and K. D. Koper (2017), Rapidly estimated seismic source parameters for the 16 september 2015 illapel, chile m w 8.3 earthquake, in *The Chile-2015 (Illapel) Earthquake and Tsunami*, pp. 11–22, Springer.

Yin, J., H. Yang, H. Yao, and H. Weng (2016), Coseismic radiation and stress drop during the 2015 mw 8.3 illapel, chile megathrust earthquake, *Geophysical Research Letters*, *43*(4), 1520–1528.

Yoshida, S., I. Sumita, and M. Kumazawa (1996), Growth model of the inner core coupled with the outer core dynamics and the resulting elastic anisotropy, *Journal of Geophysical Research: Solid Earth*, *101*(B12), 28,085–28,103.

Zhang, M., and L. Wen (2015), An effective method for small event detection: match and locate (m&l), *Geophysical Journal International*, *200*(3), 1523–1537.

Zigone, D., Y. Ben-Zion, and M. Campillo (2015), Modelling non-volcanic tremor, slow slip events and large earthquakes in the guerrero subduction zone (mexico) with space-variable frictional weakening and creep, *Geophysical Journal International*, *202*(1), 653–669.